ARTERIAL BIOMECHANICS AND THE INFLUENCES OF PULSATILITY ON GROWTH AND REMODELING

A Dissertation

by

JOHN FRANCIS EBERTH

Submitted to the Office of Graduate Studies of
Texas A&M University
in partial fulfillment of the requirements for the degree of

DOCTOR OF PHILOSOPHY

December 2008

Major Subject: Biomedical Engineering

ARTERIAL BIOMECHANICS AND THE INFLUENCES OF PULSATILITY ON GROWTH AND REMODELING

A Dissertation

by

JOHN FRANCIS EBERTH

Submitted to the Office of Graduate Studies of
Texas A&M University
in partial fulfillment of the requirements for the degree of

DOCTOR OF PHILOSOPHY

Approved by:

Chair of Committee,	Jay D. Humphrey
Committee Members,	Roland R. Kaunas
	James Moore
	Emily Wilson
Head of Department,	Gerard L. Coté

December 2008

Major Subject: Biomedical Engineering

ABSTRACT

Arterial Biomechanics and the Influences of

Pulsatility on Growth and Remodeling. (December 2008)

John Francis Eberth, B.S., Clarkson University;

M.S., Clemson University

Chair of Advisory Committee: Dr. Jay D. Humphrey

Arterial wall morphology depends strongly on the hemodynamic environment experienced *in vivo*. The mammalian heart pumps blood through rhythmic contractions forcing blood vessels to undergo cyclic, mechanical stimulation in the form of pulsatile blood pressure and flow. While it has been shown that stepwise, chronic increases in blood pressure and flow modify arterial wall thickness and diameter respectively, few studies on arterial remodeling have examined the influences that pulsatility (i.e., the range of cyclic stimuli) may have on biaxial wall morphology. We experimentally studied the biaxial behavior of carotid arteries from 8 control (CCA), 15 transgenic, and 21 mechanically altered mice using a custom designed mechanical testing device and correlated those results with hemodynamic measurements using pulsed Doppler.

In this dissertation, we establish that increased pulsatile stimulation in the right carotid artery after banding (RCCA-B) has a strong affect on wall morphological parameters that peak at 2 weeks and include thickness (CCA=24.8±0.878, RCCA-B=99.0±8.43 μm), inner diameter (CCA=530±7.36, RCCA-B=680±32.0 μm), and *in vivo* axial stretch (CCA=1.7±0.029, RCCA-B=1.19±0.067). These modifications entail stress and the change in stress across the cardiac cycle from an arterial wall macro-structural point of view (i.e., cellular and extracellular matrix)

citing increases in collagen mass fraction (CCA=0.223±0.056, RCCA-B=0.314±0.011), collagen to elastin ratio (CCA=0.708±0.152, RCCA-B=1.487±0.26), and cross-sectional cellular nuclei counts (CCA=298±58.9, RCCA-B=578±28.3 cells) at 0, 7, 10, 14, and 42 post-banding surgery. Furthermore, we study the biomechanical properties of carotid arteries from a transgenic mouse of Marfan Syndrome. This arterial disease experiences increased pulse transmission and our findings indicate that alterations occur primarily in the axial direction. The above results are all applied to a predictive biaxial model of Cauchy stress vs. strain.

To the high caliber and patient mentors I've been graced with throughout my professional and academic career: Dr. Roger Schmidt, Dr. Egidio Marotta, Dr. John Wagner, and Dr. Jay Humphrey.

"Advice is like snow; the softer it falls, the longer it dwells upon, and the deeper it sinks into the mind"

-Samuel Taylor Coleridge

ACKNOWLEDGEMENTS

This dissertation would not have been possible without the support of the Texas A&M faculty who have been approachable and patient throughout my research**.** Deepest gratitude to Dr. Jay Humphrey, Committee Chair, for his unflinching encouragement and advice, and committee members, Dr. Emily Wilson, Dr. James Moore, and Dr. Roland R. Kaunas, who have been abundantly helpful, offering invaluable assistance, support and guidance. I convey my gratitude to Dr. Vincent Gresham, my veterinary surgeon, for his extraordinary experience and dedication throughout the research.

Many colleagues at Texas A&M also had a positive influenced on my research and provided unique perspectives into biomechanics, including Ryan Pedrigi, Luca Cardamone, Clark Meyer, and Natasa Popovic. Special thanks to my undergraduates Kristin Miller and Jaclyn Boone for their hard work and genuine interest in the advancement of arterial biomechanics. I would like to thank everybody who supported this project, including Jan Patterson, Wendy Dye, Dr. Anilkumar Reddy and Dr. Rudy Gleason.

Most importantly, I would like to thank my family and loving wife Jan and her family for their continued encouragement and understanding. Without their help, I would not have had this unique opportunity.

TABLE OF CONTENTS

Page

ABSTRACT iii

DEDICATION v

ACKNOWLEDGEMENTS vi

TABLE OF CONTENTS vii

LIST OF FIGURES ix

LIST OF TABLES xv

CHAPTER

I INTRODUCTION: PULSATILE REMODELING 1

II IMPORTANCE OF PULSATILITY IN HYPERTENSIVE CAROTID ARTERY GROWTH AND REMODELING 5

- Overview 5
- Introduction 6
- Materials and Methods 7
- Results 13
- Discussion 22

III TIME COURSE OF CAROTID ARTERY GROWTH AND REMODELING IN RESPONSE TO ALTERED PULSATILITY 26

- Overview 26
- Introduction 27
- Materials and Methods 29
- Results 30
- Discussion 40

IV ALTERED BIAXIAL MECHANICAL PROPERTIES OF CAROTID ARTERIES IN AN AORTIC ARCH BANDING MOUSE MODEL OF HYPERTENSION 47

- Overview 47
- Introduction 48
- Materials and Methods 49
- Results 51

Page

CHAPTER

Discussion 60

V MECHANICS OF CAROTID ARTERIES IN A MOUSE MODEL OF MARFAN SYNDROME 64

Overview 64
Introduction 64
Materials and Methods 66
Results 71
Discussion 80

VI SUMMARY AND RECOMMENDATIONS 89

REFERENCES 92

VITA 101

LIST OF FIGURES

Page

Figure 1.1. Growth and remodeling schematic of a common carotid artery in response to acute and chronic stimulation and the arterial wall by layer 2

Figure 1.2. Mouse carotid arteries from the aortic arch banding model used in Chapters II-IV 4

Figure 2.1. Chronic hemodynamic measurements for the baseline common carotid artery (CCA), right carotid after banding (RCCA-B), and left carotid artery after banding (LCCA-B) for (a) pulse and mean pressure and (b) pulse (max-min) and mean volumetric blood flow 14

Figure 2.2. Video images of carotid arteries within the mechanical testing device: (a) baseline (CCA), (b) right vessel subjected to high pulsatile conditions after banding (RCCA-B), and (c) left vessel subjected to low pulsatile conditions after banding (LCCA-B) 15

Figure 2.3. Excised vessels pressure-diameter behaviors for RCCA-B and LCCA-B after banding and baseline CCA for: (a) outer diameter with basal smooth muscle tone and (b) inner diameter with basal smooth muscle tone 16

Figure 2.4. Cauchy (true) stress vs. stretch for right RCCA-B (—) and left LCCA-B (- - -) carotid arteries after banding and baseline carotid arteries CCA (----), each at basal tone: (a) circumferential and (b) axial directions with the location of the *in vivo* axial stretch indicated by |*,|**,|*** for CCA, RCCA-B, and LCCA-B respectively. 17

Figure 2.5. Axial force-stretch responses for CCA (----), RCCA-B (—) and LCCA-B (- - -) at fixed transmural pressures of 60, 100, or 140 mmHg with the location of the *in vivo* axial stretch (crossover point) indicated by |*,|**,|*** for the CCA, RCCA-B, and LCCA-B respectively. 18

Figure 2.6. Relationships between pulsatile, mean, or maximum pressure/flow: (a) wall thickness, (b) inner diameter, and (c) *in vivo* axial stretch 19

Figure 2.7. Histological staining for the RCCA-B and LCCA-B using (a&e) H&E to visualize cell nuclei, (b&f) VVG to visualize elastin, (c&g) PSR brightfield and (d&h) darkfields to visualize fibrillar collagen 20

Figure 2.8. Histological quantification of (a) elastin mass fraction, collagen mass fraction, and collagen to elastin ratio, as well as (b) color of collagen birefringence in the RCCA-B and LCCA-B 21

Page

Figure 2.9. Relationships amongst wall constituents, including cell count x1000 , collagen to elastin ratio, collagen mass fraction, and adventitial/total cell count and macroscopic arterial wall properties: (a) wall thickness, (b) inner diameter, and (c) *in vivo* axial stretch..... 22

Figure 3.1. Non-invasive measurements of a) mean pressure with (- - -) representing the average of both vessels at all time points, b) pulse pressure for the RCCA-B (◆) and LCCA-B (○) at each time point: 0, 7, 10, 14, or 42 days post-banding surgery. Note, time=0 is before surgery and is considered the baseline test (CCA). Error bars represent standard error of the mean (n=4:7) 31

Figure 3.2. Hemodynamic measurements of a) mean flow with (- - -) representing the average of both vessels at all time points, b) pulse flow ($Q_{max} - Q_{min}$) for the RCCA-B (◆) and LCCA-B (○) at each time point: 0, 7, 10, 14, or 42 days post-banding surgery. Note, time=0 is before surgery and is considered the baseline test (CCA). Error bars represent standard error of the mean (n=4:7). 32

Figure 3.3. Cyclic biaxial mechanical test results for a) pressure-outer diameter at λ_z^{iv} and b) axial force-stretch at 100 mmHg for at each time point: 0 (CCA ----), 7, 10, 14, and 42 days post-banding surgery for both RCCA-B (——) and LCCA-B (- - -). Note that differences between 7 and 10 days were not significant ($p>0.05$) for either vessel in the outer pressure-diameter or force-stretch data. RCCA-B force-stretch plots at 14-42 days were statistically similar and the LCCA-B force-stretch did not reach statistical significance for any time point compared to the CCA ($p>0.05$). Arrows show the shift in diameter or force as time increases indicating a maximal outer diameter for both vessels at 14 days and force at 42 days..... 33

Figure 3.4. Carotid artery circumferential morphological variables at MAP: a) wall thickness, b) inner diameter, and c) smooth muscle dependent outer passive to active diameter ratio at 100 mmHg for the RCCA-B and LCCA-B at each time point: 0, 7, 10, 14, and 42 days post-banding surgery 35

Figure 3.5. Carotid artery axial morphological variables: a) *in vivo* axial stretch, and b) *in vivo* axial force for the RCCA-B, and LCCA-B at each time point: 0, 7, 10, 14, and 42 days post-banding surgery 36

Figure 3.6. Mechanical test results for a) pressure vs. circumferential stretch and b) circumferential stress vs. stretch at each time point: 0 (CCA), 7, 10, 14, and 42 days post-banding surgery for both RCCA-B and LCCA-B 36

Page

Figure 3.7. Time course of stress in the circumferential direction for a) systole, b) mean pressure, and c) the change in stress across the cardiac cycle for RCCA-B and LCCA-B at each time point: 0, 7, 10, 14, or 42 days post-banding surgery 38

Figure 3.8. Representative histological staining for right (RCCA-B) and left (LCCA-B) carotid arteries at 0, 7, 10, 14, and 42 days after aortic banding surgery using: (a-i) Verhoeff-Van Gieson (VVG) to show elastin in black and (j-r) picrosirius red (PSR) multicolored collagen shown through birefringence 39

Figure 3.9. Time course results of histological analysis for a) collagen mass fraction, b) collagen to elastin ratio, and c) cell count for the RCCA-B and LCCA-B at each time point: 0, 7, 10, 14, and 42 days post-banding surgery 41

Figure 4.1. Averaged values of total strain energy per unit area (kPa) vs. stretch in the circumferential and axial direction for the right carotid artery before banding (0 days) and after banding (RCCA-B) at 7, 10, 14, or 42 days post-surgery 52

Figure 4.2. Averaged values of total strain energy per unit area (kPa) vs. stretch in the circumferential and axial direction for the left carotid artery before banding (0 days) and after banding (LCCA-B) at 7, 10, 14, or 42 days post-surgery 53

Figure 4.3. Averaged values of the isotropic part of the strain energy W_{iso} (kPa) versus stretch in the circumferential (λ_θ) and axial (λ_z) directions for the hypertensive right carotid artery (RCCA-B) before (0 days) and after (at 7, 10, 14, or 42 days post-surgery) banding. Low values of W under actual test conditions (λ_θ and λ_z measured) are shown as solid grayscale colors with increasing values getting lighter. Strain energy extrapolated at stretches similar to those found at baseline (CCA: $\lambda_\theta = 1-1.75$ and $\lambda_z = 1-1.75$) are displayed as a grid. 56

Figure 4.4. Strain energy (W) at physiologic operating points corresponding to mean arterial pressure and systole (λ_θ^{MAP} : λ_θ^{SYS} , λ_z^{iv}) for each time point considering a) the isotropic contribution W_{iso} , b) the anisotropic contribution W_{anis} , and c) the total energy W for the RCCA-B (◆) and LCCA-B (○) at MAP and the RCCA-B (◇) and LCCA-B (◆) at systole as time progresses after aortic banding surgery. Bars represent ± standard deviations for λ_θ^{MAP} only to simplify the graph. (∗) indicates values of

Page

statistical significance at λ_θ^{MAP} and (†) shows statistical significance at λ_θ^{SYS} between RCCA-B and LCCA-B. 58

Figure 4.5. Circumferential stretch $\lambda_\theta(s)$ with different reference configurations for the RCCA-B (◆) and LCCA-B (○) as time (s) progresses after aortic banding surgery. Figure 4.5a) shows circumferential stretch $\lambda_\theta^{MAP}(s)$ at MAP with the unloaded current configuration as a reference. Figure 4.5b) shows circumferential stretch at MAP with the original $\lambda_\theta^{MAP}(s=0)$ unloaded state as the reference. Figure 4.5c) shows the unloaded current configuration referred to the original $\lambda_{\theta,u}(s=0)$ unloaded state. Bars represent ± standard deviation. 59

Figure 4.6. a) The factor by which the arterial wall thickness (h_f) of both RCCA-B (◆) and LCCA-B (○) is greater than values that would restore it to circumferential stresses found at the baseline carotid artery. b) Wall thickness and c) circumferential stress from Chapter III are repeated here for reference purposes. Bars represent ± standard deviation of the mean. 60

Figure 5.1. Unloaded and loaded basal configurations and loaded passive configurations 70

Figure 5.2. Averaged axial force-stretch data with basal smooth muscle tone at fixed pressures of 60, 100, and 140 for carotid arteries of wild-type (WT), heterozygous (HET), and knockout (KO) mice 72

Figure 5.3. Averaged axial force-pressure experimental data at fixed axial stretches including basal and passive conditions 73

Figure 5.4. Averaged pressure-diameter experimental results at fixed axial stretches including basal and passive conditions, with those at the *in vivo* axial stretch interpolated from the other stretch-data for the carotid arteries of wild-type (WT), heterozygous (HET), and knockout (KO) mice 74

Figure 5.5. Averaged circumferential stress-stretch experimental results at fixed axial stretches including basal and passive conditions, plus interpolated results for the *in vivo* axial stretch for the carotid arteries of wild-type (WT), heterozygous (HET), and knockout (KO) mice 75

Figure 5.6. Averaged axial stress-stretch results for basal smooth muscle tone at fixed pressures of 60, 100 and 140 mmHg for the carotid arteries of

Page

wild-type (WT), heterozygous (HET), and knockout (KO) mice 76

Figure 5.7. Representative diameter dose-response for the addition of (a) phenylephrine at 10^{-5} M, (b) carbamycholine chloride at 10^{-5} M, (d) sodium nitroprusside at 10^{-4} M, and (e) Hank's Balanced Salt Solution (HBSS) containing sodium nitroprusside (10^{-5} M) and EGTA ($2x10^{-3}$ M), with maximally contracted and fully passive states at (b) and (f) 77

Figure 5.8. Average circumferential stretch values for the addition of (a) phenylephrine at 10^{-5} M, (b) carbamycholine chloride at 10^{-5} M, (d) sodium nitroprusside at 10^{-4} M, and (e) Hank's Balanced Salt Solution (HBSS) containing sodium nitroprusside (10^{-5} M) and EGTA ($2x10^{-3}$ M), with maximally contracted and fully passive states at (b) and (f) for wild-type (WT), heterozygous (HET) and knockout (KO) vessels..... 78

Figure 5.9. Constitutive fits for experimental data at three axial stretches for a) wild-type (WT) mouse #1 in Table 5.3 with $c = 2.081$ kPa, $c_1^1 = 7.558$ kPa, $c_2^1 = 0.091$, $c_1^2 = 10.846$ kPa, $c_2^2 = 0.012$ $c_1^3 = 0.662$ kPa, $c_2^3 = 0.909$, $\alpha_o = 27.58$ deg., b) heterozygous (HET) mouse #1 with $c = 20.656$ kPa, $c_1^1 = 0.185$ kPa, $c_1^2 = 0.532$, $c_1^2 = 0.051$ kPa, $c_2^2 = 0.429$, $c_1^3 = 0.576$ kPa, $c_2^3 = 0.477$ and $\alpha_o = 32.00$ deg., and c) knockout (KO) mouse #2 with $c = 0.234$ kPa, $c_1^1 = 7.086$ kPa, $c_2^1 = 0.178$, $c_1^2 = 4.978$ kPa, $c_2^2 = 0.082$, $c_1^3 = 0.265$ kPa, $c_2^3 = 0.937$ and $\alpha_o = 30.86$ deg 79

Figure 5.10. Estimated and experimental a) diameter vs. pressure for passive wild-type (WT) mouse #3 in Table 5.3 with $c = 24.292$ kPa, $c_1^1 = 0.469$ kPa, $c_2^1 = 0.493$, $c_1^2 = 1.873$ kPa, $c_2^2 = 0.278$ $c_1^3 = 0.021$ kPa, $c_2^3 = 1.425$, $\alpha_o = 39.98$ deg., or b) force vs. pressure for passive knockout (KO) mouse #2 with $c = 0.234$ kPa, $c_1^1 = 7.086$ kPa, $c_2^1 = 0.178$, $c_1^2 = 4.978$ kPa, $c_2^2 = 0.082$, $c_1^3 = 0.265$ kPa, $c_2^3 = 0.937$ and $\alpha = 30.86$ deg 81

Figure 5.11. Nonlinear optical microscopic image of a representative vessel with fibrillar collagen illuminated using 2nd harmonic generation. a) wild-type, (WT) b) heterozygous (HET), and c) knockout (KO) vessels..... 82

Figure 5.12. Passive *in vivo* axial stretch for carotid arteries of a) for wild-type (WT; 1.72), heterozygous (HET; 1.73), and knockout (KO; 1.64) mice

Page

and similarly for force b) wild-type (WT; 3.63 mN), heterozygous (HET; 3.34 mN), and knockout (KO; 2.85 mN) mouse types..... 84

LIST OF TABLES

Page

Table 4.1. Sample of best-fit parameters for a 4-fiber family model determined using the simplex method for each time point in the RCCA-B and LCCA-B at 0 (CCA), 7, 10, 14, and 42 days post-banding surgery. 55

Table 5.1. Summary of tests on mgR WT, HET, and KO mice with (*n*) given separately for basal, passive data..... 69

Table 5.2. Mechanical parameters across the cardiac cycle for carotid arteries of mgR WT, HET and KO mice. 85

Table 5.3. Best-fit parameters for a 4-fiber family model determined using the simplex method for passive carotid arteries of wild-type (WT), heterozygous (HET), and knockout (KO) mouse types for each mouse tested (n=22). 88

CHAPTER I

INTRODUCTION: PULSATILE REMODELING

The population requiring treatment for hypertension in the United States alone is 50 million with a worldwide estimate of 1 billion [1]. Hypertension is characterized by a systolic pressure exceeding 140 mmHg, a diastolic pressure exceeding 90 mmHg, or both [1]. Systolic pressure (optimally 115 mmHg) has a strong positive correlation with cardiovascular mortality, stroke and heart failure and increases throughout the lifespan of humans [1,2]. On the other hand, diastolic pressure (optimally 75 mmHg) decreases after 50 years of age leading to greater pulsatile pressure ($P_{sys} - P_{dias}$) and thus altered, dynamic vascular stimulation. Blood vessels adapt to changes in acute and chronic stimuli through short (vasomotor) or long term (growth and remodeling) responses (see Figure 1.1) [3]. These mechanical, hemodynamic stimuli changes can be the result of normal growth (e.g., pre and post-natal development) [4], vascular disease (e.g., hypertension, atherosclerosis) [4,5], surgical intervention (e.g., angioplasty, artery grafts), or natural changes in blood pressure or flow (e.g., exercise or pregnancy) [2]. Chronic changes in mechanical stimulation often involve augmented pulsatile transmural pressure (pulse pressure) and pulsatile flow.

Cyclic pressure stimuli are reduced by elastin dominated arteries (e.g., aorta and carotids) [4,5] that experience significant variations in wall shear and circumferential stress throughout the cardiac cycle. Common carotid arteries (left and right) branch off the aorta to supply the head and neck with blood. The outer layer (adventitia) consists of fibroblasts and

---

This dissertation follows the style of *The Journal of Hypertension.*

helically arranged (primarily longitudinal) type I collagen [3]. The middle layer (media) consists of helically arranged (primarily circumferential) smooth muscle cells (SMC), elastin, and types I, III and V collagen. The inner layer consists of endothelial cells and a basement membrane of laminin and type IV collagen (see Figure 1.1). Of the aforementioned constituents, collagen and elastin are the chief load-bearing proteins, while smooth muscle provides vasomotor or synthetic function [3]. This composite arterial wall allows for high distensibility at low pressures (due primarily to elastin) and low distensibility at high pressures (due primarily to collagen) [5].

Unlike stiff collagen, which turns over in the vasculature every 15-90 days[3], elastin is biochemically stable and primarily deposited during development [6-9]. It exists under tension [4,10], but reduces in mass fraction with aging [9,11-14], thus decreasing overall arterial elasticity and increasing pulse pressure [2,15]. Vascular disease may further hinder the ability of elastic arteries to dampen pulse pressure. This can be due to, hardening of the vascular wall, age/disease related loss of elastin effectiveness [16-19] or distal reflection of waves causing constructive interference [16,17].

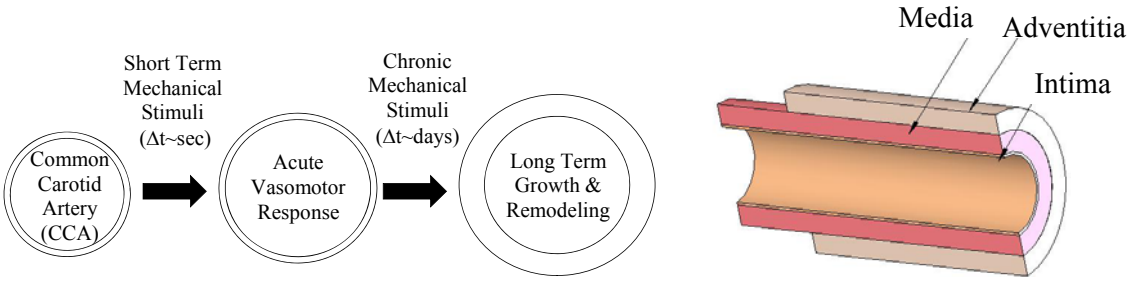

Figure 1.1. Growth and remodeling schematic of a common carotid artery in response to acute and chronic stimulation and the arterial wall by layer.

Research on resistance blood vessels (small, muscular arteries), has shown that pulse pressure can have a greater affect on cross sectional area [16-19] than peak, mean, or systolic

pressures and modulates vasoconstriction [19]. The magnitude of the pressure wave experienced by an artery depends on a variety of factors including cardiac contractility [2], location in the body [2,20], reflected waves from distal arterial beds [21] and up/downstream compliances. Pulsatile stimulation is a function of all higher level vertebras [5] yet despite the importance of pulsatility to real world application, few studies address this concept on elastic arteries *in vivo* and correlate wall morphology with pulsatile stimuli. Of particular interest are the works of Koffi *et al.* [22], Boutouyrie *et al.* [23], and Guyton and Hartley [24]. Guyton and Hartley [24] found that altered luminal circumference ratios strongly correlate with changes in peak flow and a metric of pulsatility called the pulsatility index ($PI = \left(v_{\max} - v_{\min}\right) / v_{mean}$), but not mean flow in clipped carotid arteries of rats. Boutouyrie *et al.* [23], suggested that pulse pressure had a greater affect than mean pressure on intimal-media thickening in carotids of human test subjects. In thoracic aortas of spontaneously hypertensive rats treated with the calcium blocker verapamil, Koffi *et al.* [22] also found a positive correlation between pulse pressure and thickness. They suggested that wall structure, including altered collagen to elastin ratios, can change without any changes in mean pressure and that mechanotransductive elements of the arterial wall may be receptive to dynamic stimulation.

A surgical procedure known as transverse aortic banding allows us to study the effects of changes in the magnitude of pulsatile pressure and flow in pairs of mouse carotids (see Figure 1.2) [25,26]. Using this procedure and a custom designed mechanical testing device (see Figure 1.2) [25], we have performed the first pulsatile mechanical study on growth and remodeling of paired mouse carotid arteries by comparing the highly pulsatile right vessel (RCCA-B) to the left vessel (LCCA-B). Chapter II [26] is an in-depth analysis of arterial remodeling over a long period of time in the presence of altered pulsatile stimuli. Chapter III [27] examines the pattern of hemodynamic stimulus and arterial wall response following aortic banding surgery by making

observations at 0, 7, 10, 14, or 42 days in both RCCA-B and LCCA-B. Chapter IV [28] models the findings of Chapter III using a 4-fiber family constitutive relation [29]. Finally, Chapter V [30] presents the experimental results of a mouse model of Marfan Syndrome; a disease characterized by stiffer arteries and higher pulsatile conditions [31]. The elastin portion of arteries in Marfan Syndrome are also thought to experience cyclic fatigue [32,33], a factor strongly influenced by the magnitude and frequency of pulsatility. Through experimental and mathematical analysis of arterial hemodynamics and carotid artery remodeling this dissertation aims to elucidate the relationship between pulsatile stimuli and macroscopic arterial response.

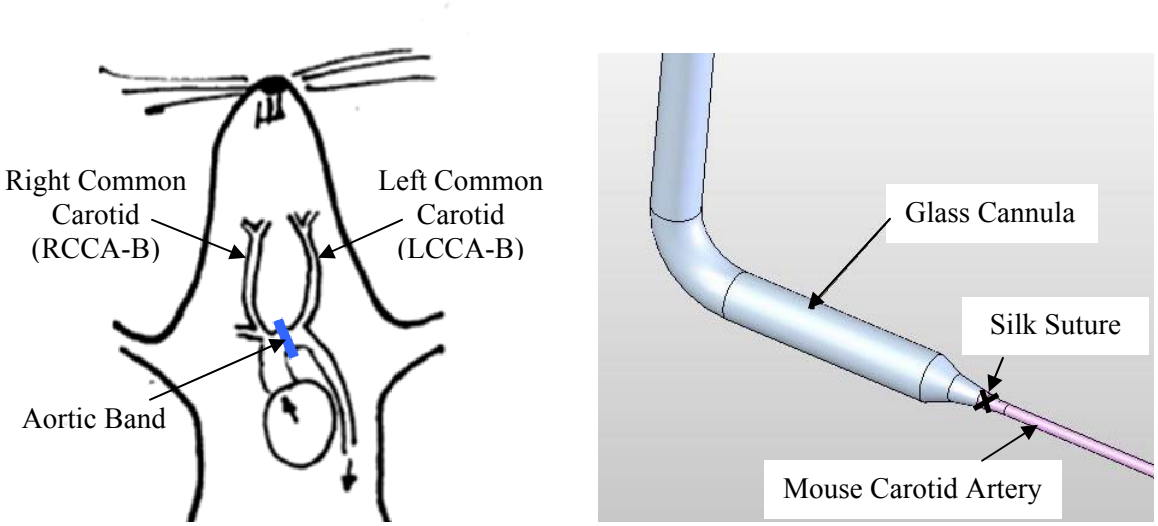

Figure 1.2. Mouse carotid arteries from the aortic arch banding model used in Chapters II-IV. All tested carotid arteries (Chapters II-V) are mounted to glass cannula and biaxially tested *in vitro* using the device described by Gleason *et al.* [25].

CHAPTER II

IMPORTANCE OF PULSATILITY IN HYPERTENSIVE CAROTID ARTERY GROWTH AND REMODELING

Overview

Arteries experience significant variations in blood flow and pressure throughout the cardiac cycle and such changes can be magnified during exercise, in disease, or with aging. In addition to mean or peak blood flow and pressure, diverse observations increasingly suggest the importance of pulsatile conditions in vascular adaptations. We used a surgical procedure known as transverse aortic arch banding to quantify effects of pulsatile pressure and flow in paired mouse carotid arteries after remodeling. We compared wall morphology, structure, and biaxial mechanical properties in the highly pulsatile right common carotid artery (RCCA-B), proximal to the band, and in the nearly normal left carotid artery (LCCA-B), distal to the band, 5 to 8 weeks after banding. Raising the magnitude of pulsatile mechanical stimuli in the RCCA-B increased wall thickness compared to the contralateral LCCA-B (RCCA-B=88.1±3.86, LCCA-B=41.6±0.815 μm), and correlated stronger with pulse (r*=0.632, p=0.006) than mean (r*=0.020, p=0.473) or systolic (r*=0.466, p=0.039) pressures. Similarly, inner diameter at mean pressure increased in the highly pulsatile vessel (RCCA-B=591±13.5, LCCA-B=410±2.7 μm) correlating only slightly stronger with pulse flow (r*=0.915, p<<0.001) than mean flow (r*=0.834, p<0.001). The amplified wall thickness and luminal diameter in the RCCA-B resulted from significant increases in cell number per cross-sectional area (RCCA-B=578±28; LCCA-B=264±40 cells) and collagen mass fraction (RCCA-B=0.314±0.0.010, LCCA-B=0.257±0.024), which appear to have contributed to the significant decrease in the *in vivo* axial stretch in the

RCCA-B (1.27±0.004) compared to the LCCA-B (1.67±0.029). Pulsatile pressure and flow are therefore important stimuli in the observed three-dimensional arterial adaptations.

Introduction

The mammalian heart pumps blood through rhythmic contractions of varying frequency and magnitude depending on demand. Large (conduit) arteries dampen out pulsations and efficiently deliver continuous blood flow to distal tissue while experiencing cyclic loading with each cardiac beat [12, 26]. The composite arterial wall provides high distensibility at low pressure (primarily due to elastin) and low distensibility at high pressure (primarily due to collagen) [5]. When blood pressure increases above normal (e.g., hypertension), the arterial wall thickens to normalize circumferential stress. Similarly, when flow increases above normal (e.g., arterial-venous fistula), the lumen enlarges to normalize wall shear stress. These adaptations result from complementary short-term (vasomotor) and long-term (growth and remodeling) responses to perturbations from normal [34]. We hypothesized that the pulsatility of the stimuli may play the dominant role in many aspects of the associated arterial adaptation.

Different diseases hinder the ability of elastic arteries to dampen pulse pressure, as, for example, via stiffening of the wall in atherosclerosis and age-related loss of elastin [35] or its mechanical effectiveness [12, 27]. Indeed, cyclic fatigue now appears to contribute to the degradation of elastin in disease and aging, thus creating a vicious cycle of stiffening and pulse wave propagation [33,36,37]. Patients with elevated pulse pressure are more prone to cardiovascular disease than those with only elevated mean blood pressure; pulse pressure should thus be considered an independent predictor of cardiovascular disease [38]. Cyclically stretching isolated smooth muscle cells similarly affects the synthesis of collagen [39] as well as cellular alignment, phenotype, and proliferation [40-43]. Endothelial cells also respond to changes in the magnitude of cyclic stimulation by aligning and elongating in the direction of flow [44-47] and

by releasing various paracrine factors [47-49] and anti-thrombogenic substances [46,50]. Because conduit artery stiffening causes increased pulse transmission, pulse pressure has been studied in resistance vessels (small, muscular arteries), [16-19] where hypertrophy correlates better with pulse pressure than with peak, mean, or systolic pressures [19]. Further, Boutouyrie *et al.* [23] showed that pulse, not mean, pressure correlates better with enlargement and thickening of carotid arteries. Similarly, Guyton and Hartley [24] found that altered luminal circumference ratios correlate with changes in peak flow and a metric of pulsatility called the pulsatility index ($PI = \left(v_{\max} - v_{\min}\right)/v_{mean}$) but not mean flow.

In this chapter, we explore roles that pulsatile mechanical stimuli play in arterial growth and remodeling. Specifically, we employed a mouse model wherein a fixed diameter band is placed around the aortic arch between the branches to the two carotid arteries for a period of 5 to 8 weeks that allows anticipated full remodeling; this procedure has been used previously to study left ventricular hypertrophy in mice [51-54]. The right common carotid artery after banding (RCCA-B) experiences a marked increase in pulsatile stimuli (pressure and flow) whereas the left common carotid artery after banding (LCCA-B) experiences a slight decrease in pulsatile stimuli, each compared to baseline common carotid arteries (CCA), while mean values remain nearly the same for all arteries [52,55]. We quantified associated changes in vessel wall morphology, histology, and biaxial mechanical properties and correlated changes therein with metrics of altered pressure and flow, estimated based on *in vivo* ultrasound.

Materials and Methods

Animals and Surgery. Male wild-type mice, having a hybrid between the common mouse types of C57BL/6J and 129Sv. These mice first underwent banding surgery at 9 to 10 weeks of age (n=7 controls, n=7 banded). All surgical procedures, housing, and experimental protocols were approved by the Texas A&M University Institutional Animal Care and Use

Committee (IACUC). Mice were sedated via an IP injection of a Xylazine/Ketamine cocktail (10 mg/100 mg in 10 ml of sterile water) at 0.1 ml/10 g body mass. Once under anesthesia, hair was removed using Nair and 3 rinses with 70% isopropyl alcohol. Buprenorphine (0.03 gm) was given IP prior to start of banding surgery. A midline incision (from mandible to mid thorax) exposed the trachea and intubation involved passing a 20 or 23 gauge catheter into the trachea, with visual verification while holding the tongue. A ventilator (Harvard Apparatus, MiniVent Respirator) was attached to the catheter and isoflurane (1.5 to 2%) started. A paramedian incision was introduced 1 mm from the sternum and each rib was cut individually to expose the heart and thymus, which was retracted to expose the aorta and carotid arteries. A curved 22 gauge needle with 6-0 ligature was passed under the aorta between the carotid arteries, and a 27 gauge (406 μm) "spacer" was placed on the arch prior to securing the ligature. The spacer was removed after securing the ligature. The chest was closed with 3 to 5 simple interrupted sutures (5-0 silk) followed by skin closure (continuous interlock pattern). The vaporizer was turned off and the animal weaned from the ventilator. Buprenorphine (0.03 gm) was given subcutaneously at 8 hour intervals following surgery (minimum of 2 additional doses) as needed depending on indications of pain. Additional information on aortic banding can be found in Rockman *et al.* [56] and Li *et al.* [55].

Non-invasive Hemodynamic Testing. After 5 to 8 weeks of recovery, *in vivo* hemodynamics were measured using a single channel pulsed Doppler mainframe and 20 MHz ultrasound probe (Indus Instruments) with a resolution of 300 μm. This measurement included blood velocities where volumetric flowrates were later calculated using diameters corresponding to *in vitro* testing and synchronized to velocity/diameter tracings by Hartley et. al [57] to give a reasonable estimate of volumetric blood flow. Blood pressure measurements were also taken at the tail and estimated locally at the carotid arteries. A subsample of hemodynamic data was

recorded one day after surgery to verify the banding procedure. This procedure was performed under 1.5 to 2% isoflurane at 1.5 LPM, which minimizes the effects of anesthesia on hemodynamics [58]. Hypoallergenic, water soluble ultrasound transmission gel (Parker Laboratories) was spread on a small location at the base of the mouse's tail, neck, and chest. Average blood velocity was measured at (ID_{sten} =406 μ m) or near the aortic band (ID_{aorta} =875 μ m) and within the left and right carotid arteries. An inflation bulb pressurized the tail cuff to systolic pressure P_{sys}, which temporarily blocked blood flow through the caudal artery. Slowly releasing the cuff pressure restored normal blood flow patterns and thus identified diastole P_{dias} [59,60].

A simple Poiseuille relation was used to estimate the pressure drop along the length of the aorta, and thus estimate arterial blood pressure at the left carotid (LCCA-B) relative to that at the tail cuff. This pressure drop is small compared to other arterial measurements of importance, however, particularly the pressure drop across the band-induced stenosis. Li *et al.* [55] experimentally verified the "simplified Bernoulli equation" (actually a control volume energy balance) for a pressure drop across a banded arch using catheters in the left and right carotid arteries. Assuming the steady, inviscid flow, this pressure drop at peak flow is

$$\Delta P = 4v_{jet}^2 \qquad (2.1)$$

where v_{jet} is the peak stenotic jet velocity at the centerline. The regression equation found by Li *et al.* [55] using the above equation at peak pressure drop is $\Delta P = \left(4v_{jet}^2 + 4.03\right)\Big/1.02$ compared to the catheter measurements.

The mean arterial pressure (MAP) in either carotid is approximated from the empiracal formula [2]

$$MAP = P_{dias} + P_{pulse}/3 \tag{2.2}$$

with P_{pulse} the local carotid pulse pressure. Calculation of the true mean pressure from the results of Li *et al.* [55] (i.e., average of the pressure waveforms for each vessel across the cardiac cycle) and comparing it to those values of mean pressure found from equation 2.2 yield errors of roughly 4.9 and 8.9% for the right and left vessels respectively, thus indicating the utility of this formula in our observations.

Mechanical Testing. Methods for harvesting, mounting, and biaxially testing isolated mouse carotid arteries are in Eberth *et al.* [30] (cf. Chapter V) and further details on the testing device are in Gleason *et al.* [61]. Unloaded dimensions were measured interactively by identifying the length at which the vessel began to bend at zero pressure; circumferential and axial stretches were calculated based on these dimensions. Preconditioning was employed to minimize hysteresis, to identify the *in vivo* axial stretch λ_z^{iv}, and to measure static inner diameters. Wall volume, estimated via 12 to 15 measurements of inner and outer radius at multiple static pressures and lengths, remained nearly constant over short periods (i.e., without growth and remodeling), thus inner radius r_i and wall thickness h were calculated assuming incompressibility. Mechanical testing consisted of cycling pressure twice from 0 to 140 mmHg at each of three fixed axial stretches $\lambda_z \approx \lambda_z^{iv}, \lambda_z^{iv+}, \lambda_z^{iv-}$ (i.e., at and ±5% of the *in vivo* value) and cycling axial extension at each of three fixed pressures (P =60, 100, 140 mmHg) while varying the axial load from 0 to 8.8 mN (0.9 g). The mechanical pressure-diameter results were interpolated for exact values of λ_z^{iv} found post experimentally.

Following mechanical testing, we evaluated both endothelial and smooth muscle functionality using methods in Eberth *et al.* [30] (cf. Chapter V). Briefly, phenylephrine (10^{-5} M) was added to the adventitial bath to determine smooth muscle contractility, then

carbamycholine chloride (10^{-5} M) was added to test for endothelial-dependent smooth muscle relaxation. Only those vessels responding to both vasoreactants with at least a 10% change in diameter were considered functional and used for basal data. The media was then replaced with Hank's Balanced Salt Solution (HBSS) without calcium and magnesium, but containing sodium nitroprusside (10^{-5} M) and EGTA ($2x10^{-3}$ M), to ensure full smooth muscle relaxation. Mechanical testing described above was repeated for the passive state.

Mean circumferential and axial wall stresses from *in vitro* experimental testing were estimated by [62,63]

$$\sigma_\theta = \frac{P\, r_i}{h},\ \sigma_z = \frac{f_T + P\pi r_i^2}{\pi\left(r_o^2 - r_i^2\right)} \qquad (2.3\text{-}2.4)$$

where P is the transmural pressure, f_T the axial force measured by the transducer, and r_o the outer radius. Stretch ratios were calculated at the mid-wall where $r_{mid} = \left(r_o + r_i\right)/2$. Basal or passive circumferential, axial, and radial stretches were calculated via

$$\lambda_\theta = \frac{r_{mid}}{R_{mid}},\ \lambda_z = \frac{\ell}{L},\ \lambda_r = \frac{1}{\lambda_\theta \lambda_z} \qquad (2.5\text{-}2.7)$$

where R and L are radii and axial length, respectively, in the unloaded basal configuration.

Histology. Specimens were removed from the testing device under passive smooth muscle conditions, fixed in 4% paraformaldehyde for 1 hour, and placed in 30% sucrose overnight. They were then put in blocks with OCT and frozen in a beaker of 2-methylbutane placed within liquid nitrogen. The frozen blocks were sectioned at 5 μm, from varying locations along the length of the vessel, and mounted on slides. The slides were stained using standard hematoxylin and eosin stain (H&E), Verhoeff-Van Gieson (VVG), and picrosirius red (PSR). The H&E, VVG, and PSR brightfield slides were imaged on an Olympus BX/51 microscope under normal polarized light, with a 20x objective, and recorded using an Olympus DP70 digital

camera. Hue, saturation, luminescence (HSL) thresholding was used to separate pixels representing constituents of interest [64]. On the H&E stained slides, connective tissue was pink/red (H=205-50^o, S=0.05-1, L=0-1) and nuclei were black/blue (H=160-290^o, S=0.1-1, L=0-0.5). Blob analysis was used on the pixels meeting the nuclei thresholding criteria to include adjacent pixels as one blob; the number of blobs was counted as nuclei number. VVG stained sections revealed collagen and smooth muscle as pink/red (H=300-17^o, S=0.04-1, L=0.1-0.9) and elastin as black (H=0-360^o, S=0-1, L=0-0.22). Nuclei also showed up blue/black in VVG stained slides and were removed from the total pixel count of elastin by blob analysis. Pixels of elastin were counted and compared to total pixels of tissue to compute mass fractions of elastin (ϕ^e). Under normal polarized light, PSR stained tissue shows collagen as pink/red (H=300-0^o, S=0.06-1, L=0.01-99) and smooth muscle a dull yellow. PSR sections were also imaged under cross-polarized light (darkfield) to observe collagen birefringence [64,65]. The collagen within the brightfield image was used as a mask for the darkfield image, and collagen fibers under cross-polarized light were quantified and separated into red (H=324-2^o), orange (H=13-53^o), yellow (H=54-72^o), or green (H=73-80^o) bins [65]. The mass fraction of collagen (ϕ^c) was based on total fibrillar collagen.

Statistical Analysis. Outliers were removed from hemodynamic and vessel wall measurements using the quartile method. Hemodynamic and morphological vessel wall measurements were compared among the baseline (CCA), banded right (RCCA-B), and banded left (LCCA-B) vessels. A Pearson correlation coefficient (r*) identified relationships between hemodynamic measurements and wall properties. Then, the critical value (t) was found for each hemodynamic-mechanical-histological relationship and the probability (p) was calculated based on the Student-t distribution using n-2 degrees of freedom and 2 tails. Comparisons were considered to significantly affect the wall when $p<0.05$.

Results

Immediately after banding, the RCCA-B became engorged while the LCCA-B appeared slightly smaller. Based on all banded animals (n = 4 one day after banding, n=7 five to eight weeks after banding), the pulse pressure ($P_{max} - P_{min}$) was statistically higher in the RCCA-B (CCA=43.0±4.08, RCCA-B=61.6±7.14, LCCA-B=31.1±2.81 mmHg) while differences in mean arterial pressure were minor (CCA=98.1±3.93, RCCA-B=90.5±4.84, LCCA-B=85.8±2.21 mmHg) as seen in Figure 2.1a. The pulse flow ($Q_{max} - Q_{min}$) was also significantly higher in the right carotid (CCA=0.042±0.005, RCCA-B=0.066±0.0023, LCCA-B=0.017±0.001 ml/s) while mean flow had some minor difference between baseline and the right carotid (CCA=0.016±0.003, RCCA-B=0.022±0.003 ml/s) as seen in Figure 2.1b. The left carotid experienced a slight, but statistically significant reduction, in mean flow (LCCA-B=0.012±0.001 ml/s) relative to R.

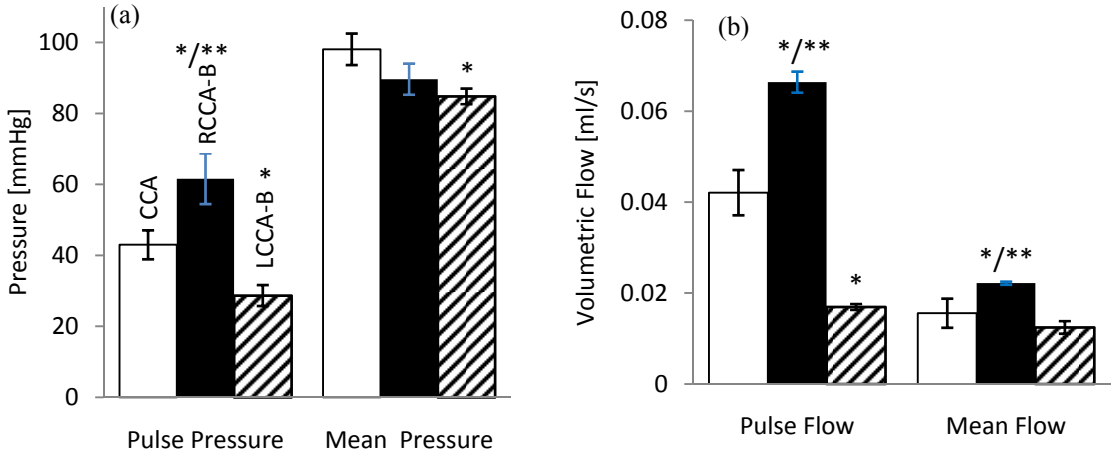

Figure 2.1. Chronic hemodynamic measurements for the baseline common carotid artery (☐ CCA), right carotid after banding (■ RCCA-B), and left carotid artery after banding (▨ LCCA-B) for (a) pulse and mean pressure and (b) pulse (max-min) and mean volumetric blood flow. Statistical significance at $p<0.05$ is indicated by (*) for RCCA-B and LCCA-B vessels compared to CCA and by (**) for comparison between RCCA-B and LCCA-B. Bars are standard error of the mean.

Upon excision, the right carotids appeared grossly larger with an apparently disorganized adventitia (Figure 2.2b) compared to baseline (Figure 2.2a) or left carotids (Figure 2.2c). Gentle, yet consistent, tugging with forceps did not remove this outer tissue. Furthermore, the RCCA-B was able to withstand significant bending moments to the degree that the vessel did not bend when held horizontally. Wall thickness was significantly greater in right carotids compared to baseline while a small increase occurred in the left carotids (CCA=24.8±0.878, RCCA-B=88.1±3.86, LCCA-B=41.6±0.815 μm).

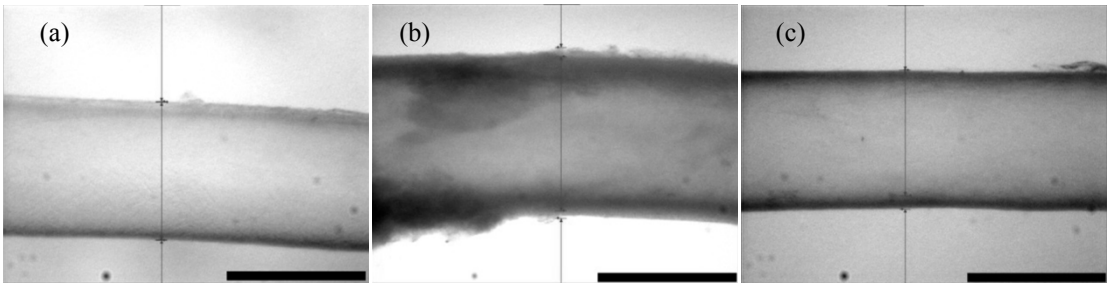

Figure 2.2. Video images of carotid arteries within the mechanical testing device: (a) baseline (CCA), (b) right vessel subjected to high pulsatile conditions after banding (RCCA-B), and (c) left vessel subjected to low pulsatile conditions after banding (LCCA-B). Figures are to scale and the black bar represents 660 μm. Vertical lines show video calipers used to measure outer diameters on-line.

Inner diameters were consistently larger in right carotids compared to left or baseline carotids at all pressures. Compare, for example, the basal inner diameter at the individual mouse's mean arterial pressure (CCA=484±8.51, RCCA-B=591±13.5, LCCA-B=410±2.77 μm), at individual vessel systolic pressures (CCA=507±10.7, RCCA-B=675±12.1, LCCA-B=467±20.2 μm), and at a common pressure of 100 mmHg (CCA=496±8.92, RCCA-B=633±1.23, LCCA-B=482±3.39 μm). Diameters were 9% and 16% larger for CCA and LCCA-B, respectively, in the passive state compared to basal smooth muscle tone while there was little difference in the passive diameter of the RCCA-B compared to its basal state.

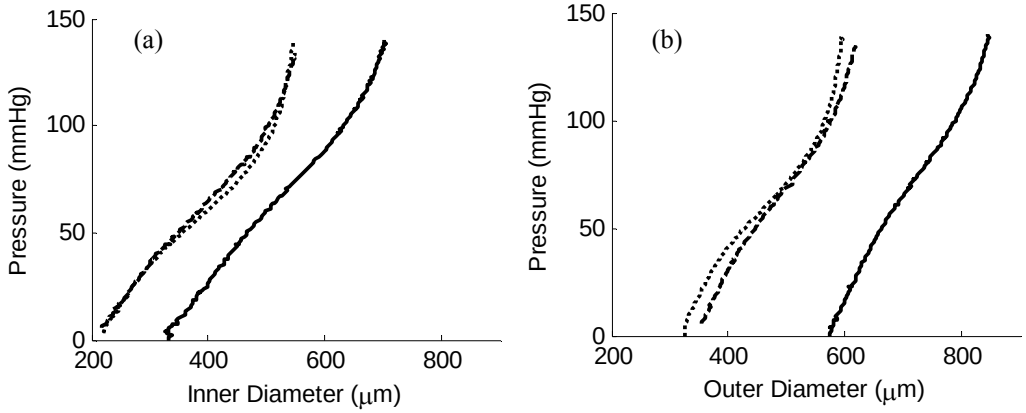

Figure 2.3. Excised vessels pressure-diameter behaviors for RCCA-B (—) and LCCA-B (- - -) after banding and baseline CCA (----) for: (a) outer diameter with basal smooth muscle tone and (b) inner diameter with basal smooth muscle tone. Inner and outer diameters of CCA and LCCA-B were nearly the same while RCCA-B was statistically greater at all pressures.

Although both RCCA-B and LCCA-B reached an apparent steady state outer diameter remodeling after about 2 weeks (data not shown), circumferential stresses did not appear to return to equilibrium values by 5 to 8 weeks. At the individual vessels mean transmural pressures, circumferential stresses in RCCA-B and LCCA-B were lower than the control (CCA=124±4.03, RCCA-B=44.8±5.76, LCCA-B=53.1±1.26 kPa). Similarly, at a common pressure of 100 mmHg, circumferential stresses were lower in RCCA-B compared to LCCA-B or CCA (CCA=137±1.69, RCCA-B=56.9±0.720, LCCA-B=90.6±2.39 kPa). At systole there was no significant difference between left and right banded vessels (CCA=173±4.62, RCCA-B=80.4±10.1, LCCA-B=90.0±6.82 kPa). Stress-stretch plots of averaged data at λ_z^{iv} in the basal state (Figure 2.4) revealed that RCCA-B had a lower circumferential stress for a given circumferential stretch than baseline while LCCA-B had a higher stress compared to baseline. Once smooth muscle cells were relaxed (data not shown), LCCA-B stress-stretch plots continued to be higher than CCA while RCCA-B were nearly identical to CCA, thus reinforcing the importance of smooth muscle tone in the balance of stress in the circumferential direction.

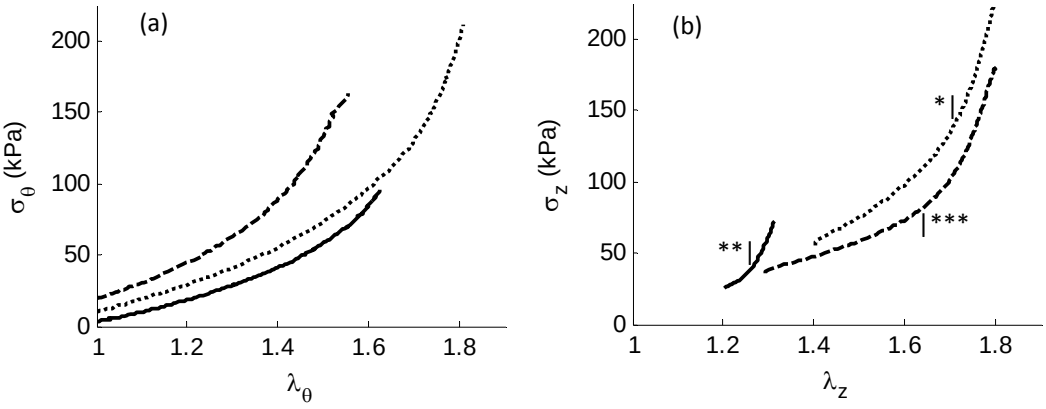

Figure 2.4. Cauchy (true) stress vs. stretch for right RCCA-B (—) and left LCCA-B (- - -) carotid arteries after banding and baseline carotid arteries CCA (----), each at basal tone: (a) circumferential and (b) axial directions with the location of the *in vivo* axial stretch indicated by |*,|**,|*** for CCA, RCCA-B, and LCCA-B respectively.

In contrast, the axial direction experienced significant changes in mechanical characteristics due to altered pulsatility. The *in vivo* axial stretch (λ_z^{iv}), defined as the ratio of the in-situ length divided by the unloaded length, decreased significantly in the right compared to the left or control carotids (CCA=1.72±0.029, RCCA-B=1.27±0.004, LCCA-B=1.67±0.029). The basal *in vivo* force (F_z^{iv}) needed to maintain the vessel at this extension similarly differed between groups (CCA=3.47±0.137, RCCA-B=2.16±0.042, LCCA-B=2.68±0.035 mN). The LCCA-B and CCA had nearly the same force response during cyclic axial stretching while the RCCA-B had a much greater force at all stretches (Figure 2.5). Both *in vivo* axial stretch and *in vivo* force were statistically similar between basal and passive states (not shown). Axial stresses were higher in RCCA-B than LCCA-B or CCA for a given stretch, but quckly reached a limit imposed on the force transducer to prevent over extending the vessels (Figure 2.4b).

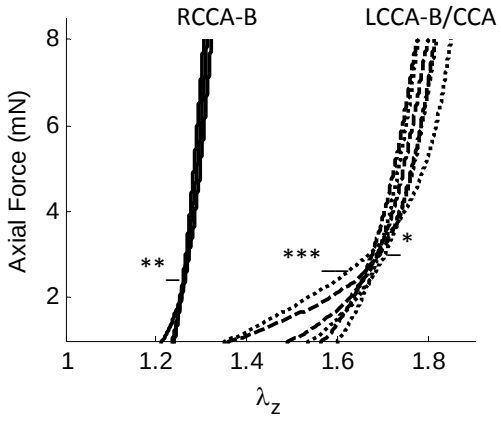

Figure 2.5. Axial force-stretch responses for CCA (----), RCCA-B (—) and LCCA-B (- - -) at fixed transmural pressures of 60, 100, or 140 mmHg with the location of the *in vivo* axial stretch (crossover point) indicated by |*,|**,|*** for the CCA, RCCA-B, and LCCA-B respectively.

Changes in pulse pressure ($r^*=0.632$, $p=0.006$) and systolic pressure ($r^*=0.466$, $p=0.040$) correlated with altered wall thickness whereas changes in mean pressure ($r^*=0.020$, $p=0.473$) did not (cf. Figure 2.6a). Inner diameter, measured at mean pressure (Figure 2.6c), changed throughout remodeling time with all flow parameters (Q_{max}, Q_{min}, Q_{max}-Q_{min} and Q_{mean}), with a slightly stronger correlation between Q_{max}-Q_{min} ($r^*=0.915$, $p<<0.001$) than Q_{mean} ($r^*=0.834$, $p<0.001$). Correlation patterns between flow variables and inner diameter were similar at all pressures tested (i.e., 100 mmHg, systolic, diastolic, and mean pressures). Changes in pulse ($r^*=-0.680$, $p=0.005$) and systolic ($r^*=-0.544$, $p=0.027$) pressure each correlated inversely with *in vivo* axial stretch (Figure 2.6b). Likewise, all flow parameters (not shown) correlated inversely with *in vivo* axial stretch at $p<0.001$. The *in vivo* axial force had the strongest negative correlation with pulse pressure ($r^*=-0.582$, $p=0.017$) and all flow parameters: Q_{max} ($r^*=-0.933$, $p<0.001$), Q_{max}-Q_{min} ($r^*=-0.961$, $p<0.001$), and Q_{mean} ($r^*=-0.884$, $p<0.001$).

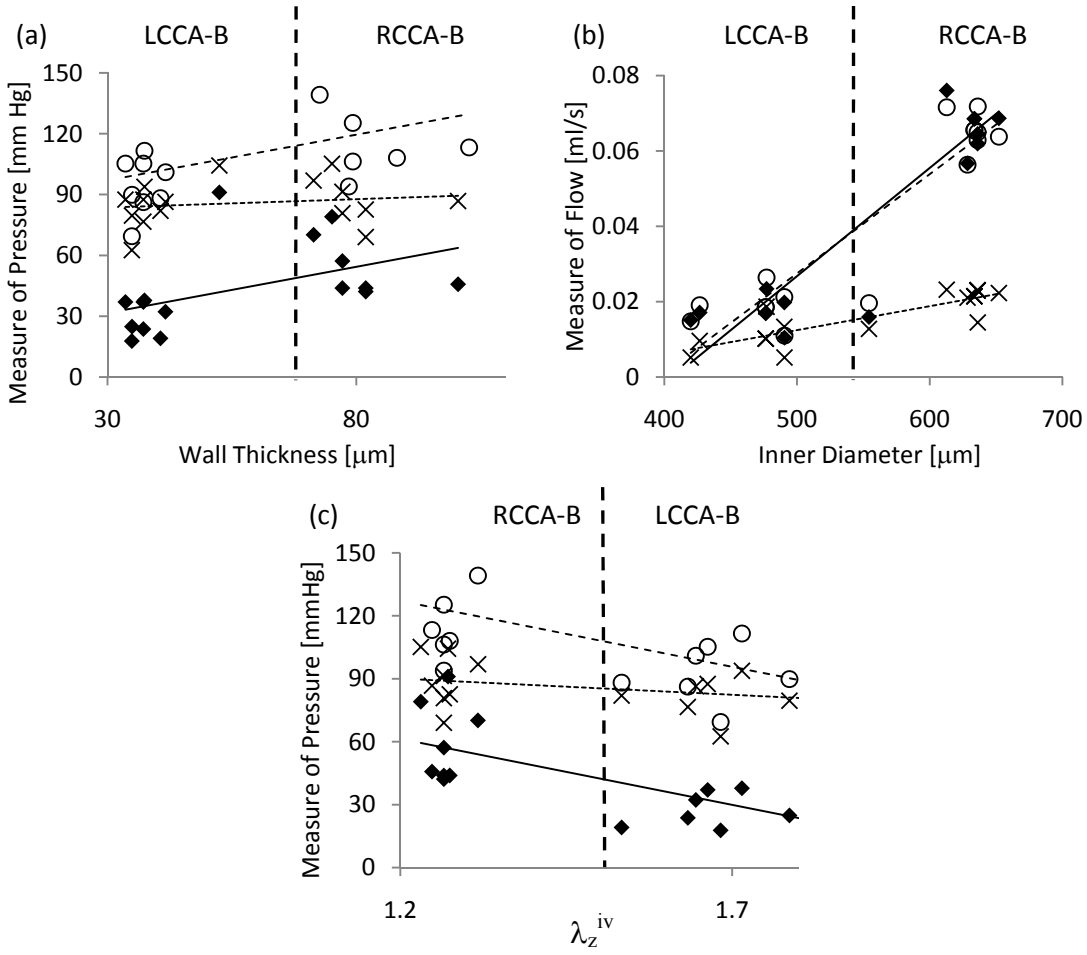

Figure 2.6. Relationships between pulsatile (—◆—), mean (----×----), or maximum (- - -○- - -) pressure/flow: (a) wall thickness, (b) inner diameter, and (c) *in vivo* axial stretch (λ_z^{iv}). Linear relationship chosen for consistency with existing literature [22-24].

Histological sectioning revealed that increased wall thickness in the RCCA-B was due to the accumulation of collagen and proliferation of cells. Sections of RCCA-B and LCCA-B stained with H&E revealed cell nuclei (Figure 2.7 a&e), while VVG revealed elastin (Figure 2.7 b&f), and brightfield (Figure 2.7 c&g) and darkfield (Figure 2.7 d&h) PSR revealed fibrillar collagen. RCCA-B sections showed a marked increase in disorganized adventitial tissue with a distinct seperation of layers that may have occurred during sectioning, which also distorted the

sections from circular. This separation suggests that much of the newly accumulated collagen was only loosely connected to the rest of the tissue after highly pulsatile remodeling.

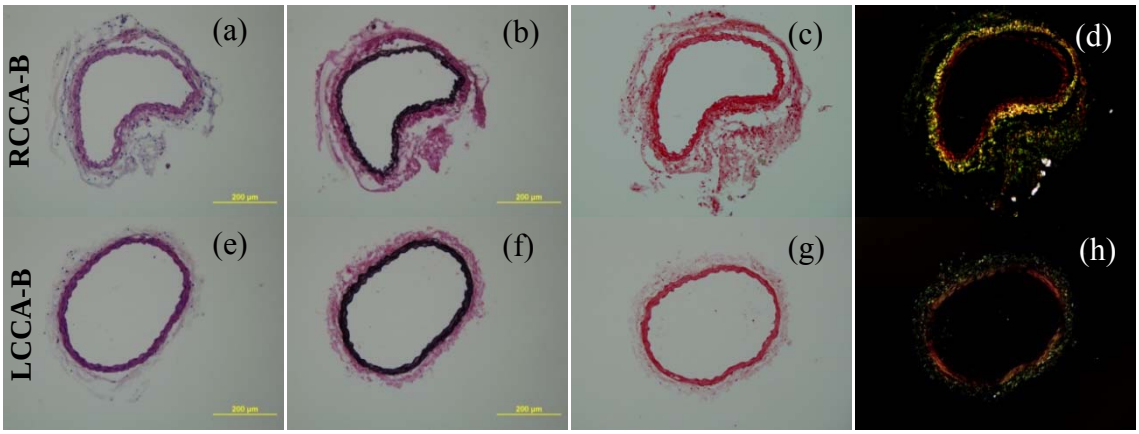

Figure 2.7. Histological staining for the RCCA-B and LCCA-B using (a&e) H&E to visualize cell nuclei, (b&f) VVG to visualize elastin, (c&g) PSR brightfield and (d&h) darkfields to visualize fibrillar collagen.

The increase in wall constituents in high pulsatility (RCCA-B) resulted, in part, from increased cell number and collagen mass fraction. After thresholding and blob analysis, H&E stained slides revealed a two-fold greater number of cell nuclei for RCCA-B compared to LCCA-B (RCCA-B=578±28, LCCA-B=264±40). Furthermore, right carotids increased in collagen mass fraction (ϕ^c) compared to left carotids (RCCA-B=0.314±0.010, LCCA-B=0.257±0.024), with corresponding increases in the collagen to elastin ratio (RCCA-B=1.49±0.261, LCCA-B=0.570±0.059) (Figure 2.8a). Of the collagen found in the vascular wall, the RCCA-B had a higher percentage of fibers with green birefreingence (20%), indicating a greater proportion of thinner fibers (Figure 2.8b) [65], while less than 10% of the LCCA-B fibers were green. The LCCA-B contained a greater proportion of thicker, centrally located, orange fibers (34%) compared to that of the RCCA-B (25%).

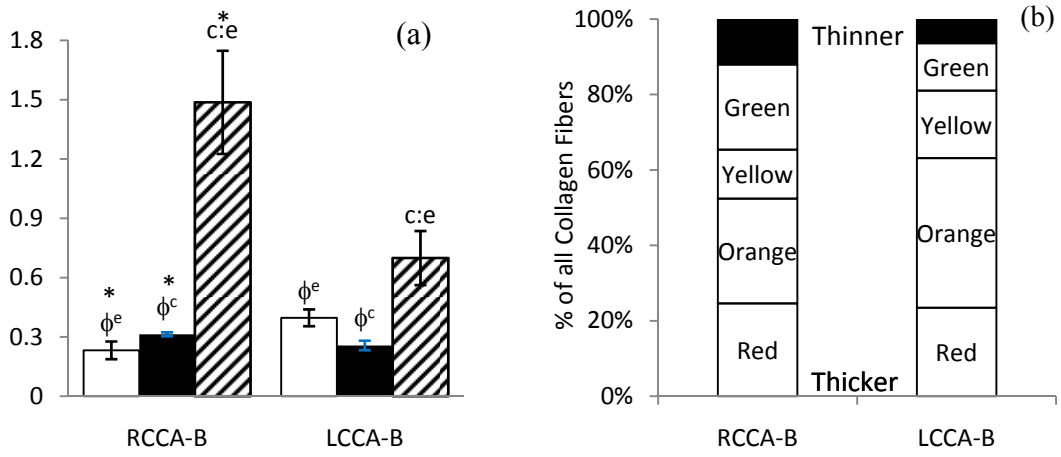

Figure 2.8. Histological quantification of (a) elastin mass fraction (□ ϕ^e), collagen mass fraction (■ ϕ^c), and collagen to elastin ratio (▨ c:e), as well as (b) color of collagen birefringence [65] in the RCCA-B and LCCA-B. Statistical significance between RCCA-B and LCCA-B at $p<0.05$ is indicated by (*) for Figure 2.8a. Bars represent standard error of the mean.

Changes in the number of cell nuclei (Figure 2.9 a-c) correlated well with inner diameter ($r^*=0.877$, $p=0.008$), the decrease in the *in vivo* axial stretch ($r^*=-0.818$, $p<0.001$), and wall thickness ($r^*=0.826$, $p<0.001$). As the wall thickened, in response to increased pulsatility (cf. Figure 2.6a), the mass fraction of collagen (ϕ^c) increased ($r^*=0.5963$, $p=0.045$) as seen in Figures 2.8a and 2.9a. Of note, the inner diameter ($r^*=-0.665$, $p=0.018$) correlated inversely with the mass fraction of elastin (ϕ^e). The collagen to elastin ratio also correlated inversely with *in vivo* axial stretch ($r^*=-0.709$, $p=0.01$) (Figure 2.9c).

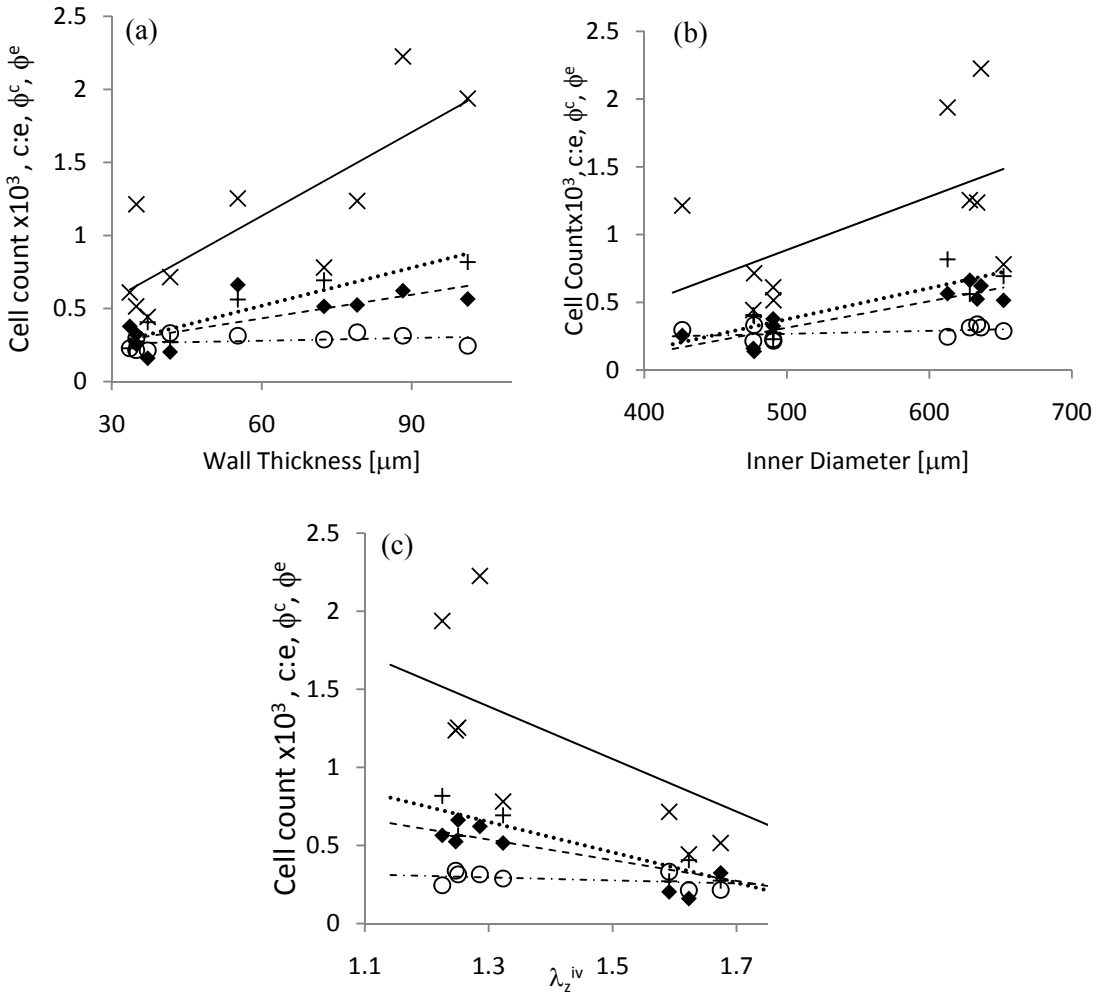

Figure 2.9. Relationships amongst wall constituents, including cell count x1000 (- - ◆ - -), collagen to elastin ratio (—×—), collagen mass fraction (ϕ^c) (- - ○ - -), and adventitial/total cell count (···+···) and macroscopic arterial wall properties: (a) wall thickness, (b) inner diameter, and (c) *in vivo* axial stretch.

Discussion

Consequences of arterial growth and remodeling in response to dynamic mechanical stimuli may be more important than previously thought. To elucidate this relationship, we placed a non-compliant band around the aortic arch in mice to cause the paired carotid arteries to have similar mean pressure and flow, but different pulsatility. After the bulk of arterial remodeling

had occurred, we correlated changes in hemodynamics with changes in vessel wall morphology, histology, and mechanical responses. Our findings suggest that increasing the magnitude of pulsatile mechanical stimuli in the right carotid artery increased the wall thickness compared to both baseline and the left carotid arteries and this change correlated better with pulse pressure than mean or systolic pressure. Increased wall thickness and luminal diameter appeared to result from both amplified cell proliferation (smooth muscle but mainly fibroblasts) and collagen synthesis. Similarly, inner diameter (measured *in vitro* at mean pressure) increased in the highly pulsatile vessel and correlated only slightly better with pulse flow than with mean flow.

Pulse pressure has been identified as an independent risk factor in human cardiovascular disease [38]. An increase in systolic pressure promotes cardiac hypertrophy while a decrease in diastolic pressure can decrease coronary perfusion. Nevertheless, few studies of vascular mechanics have attempted to correlate dynamic mechanical stimuli with known predictors of cardiovascular disease *in vivo*. While it has been shown that pulse pressure affects wall thickness in resistance arteries [16-18], few have studied elastic arteries. We found increased wall thickness to correlate strongly with pulse pressure ($r^*=0.632$, $p=0.006$), but not mean pressure ($r^*=0.020$, $p=0.473$). Boutouyrie *et al.* [23], using a different correlation method (Spearman), similarly suggested that pulse pressure had a greater affect than mean pressure on intimal-media thickening in human carotids. Koffi *et al.* [22] also found a positive correlation between pulse pressure and thickness of thoracic aorta in rats treated with the calcium blocker veraparil. They suggested that wall structure, including altered collagen to elastin ratios, can change without any change in mean pressure. Based on all data available, therefore, it appears that effects of pulse pressure on arterial structure and function may be important locally and transmitted to distal vessels causing a vicious cycle of vascular stiffening. The remodeling manifests especially in the adventitia where stiff collagen prevents overstretching [13], thus adventitial fibroblasts may be

largely responsible for this control mechanism. The high degree of adventitial remodeling in the RCCA-B was confirmed by histological analysis that showed a higher adventitial cell number (Figures 2.7&2.9) and an increase in the proportion of green (thinner) fibers located there. The smaller, green, fibers may be in some state of assembly but might not be ready to fully bear load. It seems that fibroblasts are sensitive to cyclic loading, yet many cyclic tests on fibroblasts and myofibroblasts use non-stretched static controls rather than statically stretched controls [42]. These incompressible constituents probably contribute to reductions in in-vivo axial stretch by providing a counteracting force to the retracting elastin upon excision.

Blood flow controls arterial caliber, but there has been little attention to pulsatility. Guyton and Hartley [24] found, however, that luminal circumference ratios correlated better with peak velocity and an index of pulsatility than with mean blood flow in restricted carotid arteries of juvenile rats. Our data partially supports this observation; carotid caliber in the banded right carotids (cf. Figure 2.3a) correlated slightly better with pulse ($r^*=0.915$, $p<<0.001$) than mean ($r^*=0.834$, $p<0.001$) flow. Responses to pulsatile blood flow likely occur via mechanotransduction mechanisms resulting in endothelial cell alignment [46,47] and release of vasoactive and remodeling molecules [46,48,49] that affect arterial diameter throughout remodeling time.

Blood flow may include steady and oscillatory components depending on location along the vascular tree, including reversed flows near valves or stenotic regions. Indeed, sites of atherosclerosis tend to correlate with oscillatory shear stress [49]. Prostacyclin, an inhibitor of platelet aggregation and a mild vasodilator, increases in cultured endothelial cells subjected to pulsatile flow compared to steady flow [48]. Our findings revealed little difference between RCAA-B tested at basal or passive smooth muscle tone, suggesting that either the vessels were already mostly passive or they were so stiff that smooth muscle relaxation had little effect.

Paradoxically, Ziegler *et al.* [49] found that cells exposed to waveforms of shear stress with flow reversal released more endothelin-1 (a vasoconstrictor) with reduced eNOS compared to unidirectional shear stress. This confirms that mechanosensors in endothelial cells can sense and react differently to different dynamic stresses. Himburg *et al.* [46] showed that modulating frequency affected a variety of independent anti-inflammatory and atheroprotective gene transcription factors, albeit far less than alterations in mean shear. They also noted that frequencies exceeding normal heart rate and shear reversal both promote atherogenesis.

With advanced capability for non-invasive hemodynamic measurement, there is an opportunity to understand better the consequences of the full spectrum of alterations in pulsatile blood pressure and flow on the arterial wall. Morphological wall variables, are shown here to correlate well with pulsatile stimuli. The three layers of the arterial wall appear to respond differently to altered states of stress and different components of pulsatility may drive remodeling. Hence, the complex biomechanics and mechanobiological processes demand continued investigation, which will be facilitated by combining mathematical modeling with experimentation.

CHAPTER III

TIME COURSE OF CAROTID ARTERY GROWTH AND REMODELING IN RESPONSE TO ALTERED PULSATILITY

Overview

Arteries adapt to mechanical perturbations that may involve alterations in maximum, mean, or pulsatile pressure and flow via short-term (vasomotor) and long-term (remodeling) responses. We used an aortic arch banding mouse model that alters pulsatile pressure and flow between paired carotid arteries, and quantified *in vivo* hemodynamics using non-invasive ultrasound and *in vitro* wall properties via biaxal testing at 0, 7, 10, 14, or 42 days post-surgery. Compared to the baseline carotid artery (CCA) or the left carotid after banding (LCCA-B), the right carotid after banding (RCCA-B) showed a large increase in pulsatile pressure (CCA=43.0±4.08, RCCA-B=79.7±4.01, LCCA-B=42.6±2.44 mmHg) and pulsatile flow (CCA=0.042±0.005, RCCA-B=0.085±0.002, LCCA-B=0.029±0.001 ml/s) at 7 days that reduced to moderate, yet elevated pulsatile values after 42 days. Wall thickness (CCA=24.8±0.878, RCCA-B=99.0±8.43, LCCA-B=40.5±2.24 μm) and inner diameter (CCA=530±7.36, RCCA-B=680±32.0, LCCA-B=591±23.6 μm) both peaked in the right carotid at 14 days post-surgery. The ratio of fully passive to active outer diameter was 7 times greater in the LCCA-B than in the RCCA-B implying reduced contractility in the right. Interestingly, circumferential stress decreased in both banded vessels throughout the first 10 days after surgery (CCA=125±4.03, RCCA-B=75.0±8.68, LCCA-B=61.1±4.38 kPa) but were not considered statistically significant from each other until 14 days. The change in stress across the cardiac cycle, however, was higher in the RCCA-B than LCCA-B until 14 days, at which time the changes in stress across the cardiac cycle normalized between left and right (RCCA-B=62.3±16.0, LCCA-B=65.2±5.26

kPa). These findings suggest that: (1) pulsatile stimuli are important, (2) hemodynamic and wall morphological response experiences may initially overcompensate, and (3) mean stress and the change in stress across the cardiac cycle may be controlled.

Introduction

Hypertension, and the associated cardiovascular risks, occurs when blood pressure (optimally 115/75 mmHg) exceeds a systolic pressure of 140 mmHg, a diastolic pressure 90 mmHg, or both [1]. Systolic pressure normally increases more than diastolic pressure, thus an increase in pulse pressure accompanies hypertension, especially in aging [1]. Indeed, increasing evidence suggests that pulse pressure should be looked at as an independent predictor of cardiovascular disease [38]. All higher level vertebrates have some level of pulsatility [5] and the large elastic arteries (i.e., aorta and carotids) normally dampen this pulse wave to deliver a continuous blood flow to distal tissue that facilitates mass transfer [16,23]. In particular, elastin endows the arterial wall with significant passive elastic recoil such that blood flows even during diastole; collagen, in turn, provides stiffness that protects smooth muscle cells from overextension during pressurization [5,21]. The magnitude of arterial pulsations thus results from a complex interplay of arterial compliance, downstream resistance, and reflected waves, which is to say location along the vascular tree [21,66]. For example, in diseases of elastin [30,33,35,56] (cf. Chapter VI) and general aging [5,54,56], arterial stiffening can further the transmission of pulse waves that are then reflected at distal locations creating an even greater work load on the heart. This augmented pulse wave leads to a vicious cycle of altered mechanical stimulus and response in both distal and proximal vessels [17,67]. During development, the arterial system can easily adapt to alterations in stimulus by regulating genes responsible for the production of most proteins, but this response may not be completely available later in life when hypertension often initiates via an augmented pulsatile pressure [1] .

The time-dependent response of the arterial system to localized mechanical perturbations represents a complex interplay between effectors (pressure, flow) and sensors (biologically active cells). The intricacy of this relationship is compounded by the dynamic, cyclic nature of the mechanical perturbations experienced *in vivo* as the stimulus can have both steady and unsteady components with varying frequencies [3,21], and in the case of flow, a potential for reversal [49] . Endothelial cells, smooth muscle cells, and fibroblasts are responsible for sensing consequences of altered pressure and flow and to modify the synthesis, distribution, or organization of structurally significant extracellular matrix proteins in an attempt to restore, to within a tolerance, the intramural and wall shear stresses toward normal. Newly synthesized cells and matrix proteins may be distributed within the wall in a manner that efficiently controls stress, but true optimization may need to involve the stress at diastole, systole, and mean arterial pressure (MAP). Throughout the cardiac cycle, hence the absorbed energy, changes in the arterial wall. Our previous work showed that mouse carotids achieved the bulk of their remodeling after 5 to 8 weeks of hypertension, evidenced grossly by increased wall thickness and caliber, which correlated, at least slightly, stronger with pulsatile than mean stimuli [26] (cf. Chapter II). There is a need, however, to consider the time-course of changes during the development of the hypertension to ultimately improve predictive capabilities of mathematical models. That is, to identify how properties change in the long-term (growth and remodeling - days to weeks) to control how wall structure and function might change in the short term (across the cardiac cycle - seconds).

In this chapter, we exploit a transverse aortic arch banding mouse model that creates different pulsatile blood pressure and flow in pairs of carotid arteries. This model has been used previously to study cardiac hypertrophy [52,53] and peripheral adaptation [55] in normal and aged mice [54]. Aortas were banded for 0, 7, 10, 14, or 42 days. Measurements of *in vivo*

hemodynamics were taken under mild anesthesia at each time point, then vessels were excised and tested biaxially. Experiments were performed using a custom designed mechanical testing device and specimens were stained for histological examination. This process allowed us to explore changes in altered pulsatility on carotid artery remodeling in terms of the time course of changes in microscopic and macroscopic metrics of wall structure and smooth muscle contractility.

Materials and Methods

The Texas A&M Institutional Animal Care and Use Committee (IACUC) approved all surgical, housing, and experimental protocols, details on which are in Eberth *et al.* [26] (cf. Chapter II). Briefly, aortic arch banding surgery was performed on wild-type male mice, with a hybrid C57BL/6J and 129Sv background, at 9 to 10 weeks of age. The total number of vessels in this study was 42 (roughly 21 mice). Mice were allowed to recover for 7, 10, 14, or 42 days after banding surgery, at which time noninvasive hemodynamic measurements were taken from both the left (LCCA-B) and right (RCCA-B) common carotid arteries as well as within the aortic stenosis. Blood pressures were measured at the tail and interpreted via Poiseuille's relation to estimate local blood pressures in the left carotid artery; equations for a pressure drop across a stenosis estimated local pressures in the right carotid [55]. Then *in vitro* mechanical testing was performed on pairs of carotid arteries on a custom designed mechanical test system under both passive and basal smooth muscle tone. Smooth muscle and endothelial cell functionality was tested using the method outlined in Eberth *et al.* [26] (cf. Chapter II) and only those vessels that proved to be functional were used in the analysis. Histological investigation was performed on cross sections of arteries using standard hematoxylin and eosin (H&E), Verhoeff-Van Gieson (VVG), and picrosirius red (PSR) stains with HSL thresholding used to observe characteristics of

interest. The right (RCCA-B) and left (LCCA-B) carotids at 7, 10, 14, or 42 days after banding were compared to baseline common carotid arteries (CCA) considered as day 0 throughout.

Outliers were removed from hemodynamic and vessel wall measurements using the quartile method. Measurements were compared among the baseline (CCA), right (RCCA-B), and left (LCCA-B) vessels as well as between consecutive time points in the banded vessels. The probability (p) was calculated based on the Student-t distribution using n-2 degrees of freedom and 2 tails. Hemodynamic, mechanical, and histological comparisons amongst vessels were considered statistically significant when $p<0.05$.

Results

The hemodynamics changed dramatically post-surgery as the arterial system adapted to distal demands by altering local arterial makeup and modifying downstream resistances. The mean arterial pressure (MAP) was virtually identical (98.1±4.44 mmHg) between the two common arteries (CCA) at day 0 (Figure 3.1a). Following banding surgery, mean blood pressure was at a level of statistical insignificance amongst consecutive time points and between RCCA-B and LCCA-B (dotted line on Figure 3.1a). The diastolic pressure remained similar over time (not shown) and between RCCA-B and LCCA-B while systolic pressure increased immediately after surgery in the RCCA-B (147±0.616 mmHg) compared to CCA (120±1.91 mmHg), reaching a peak at 14 days (154±8.42 mmHg) followed by a return towards baseline after 42 days (125±8.42 mmHg). Meanwhile, the LCCA-B did not experience significant changes in systolic pressure except for a slight decrease after banding (110±1.02 mmHg). Accordingly, the pulse pressure in the right carotid jumped after banding (CCA=43.0±4.08, RCCA-B=79.7±4.01, LCCA-B=42.6±2.44 mmHg) and remained higher than baseline throughout the study (Figure 3.1b). The left carotid experienced a slight decrease in pulsatile pressure, reaching statistical significance at 42 days post surgery.

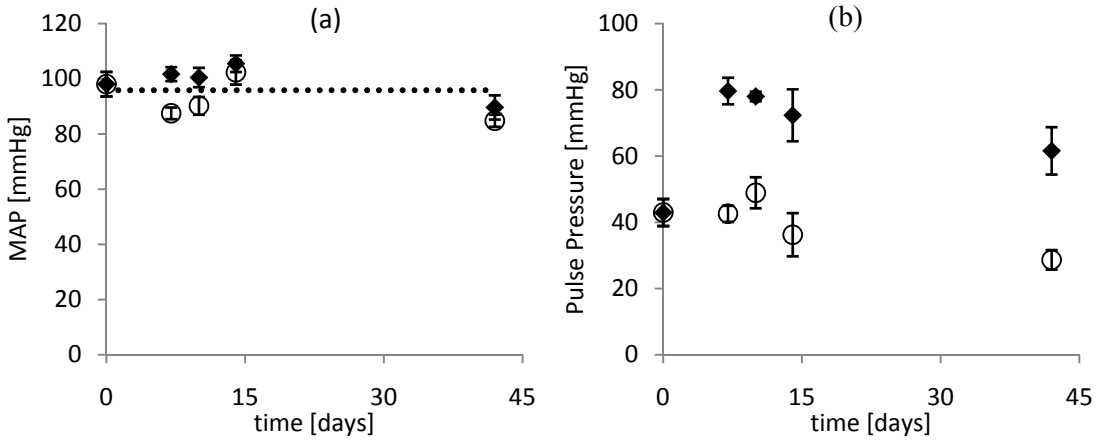

Figure 3.1. Non-invasive measurements of a) mean pressure with (- - -) representing the average of both vessels at all time points, b) pulse pressure for the RCCA-B (◆) and LCCA-B (○) at each time point: 0, 7, 10, 14, or 42 days post-banding surgery. Note, time=0 is before surgery and is considered the baseline test (CCA). Error bars represent standard error of the mean (n=4:7).

The mean volumetric flowrate (Q_{mean}) changed little in the right carotid only at the first time point after banding (CCA=0.016±0.003, RCCA-B=0.032±0.001 ml/s) and then returned towards baseline with little change in the LCCA-B (0.021±0.005 ml/s) (Figure 3.2a). Pulse flow ($Q_{max} - Q_{min}$; Figure 3.2b) changed throughout the post-surgery time for both vessels and was always higher in the right than left carotid. The right carotid experienced a large increase in pulse flow in the first 7 days after banding (CCA=0.042±0.005, RCCA-B=0.085±0.002 ml/s); the left carotid had a pulse flow similar to the baseline until 10 days (LCCA-B=0.019±0.002 ml/s) when it dropped and remained low.

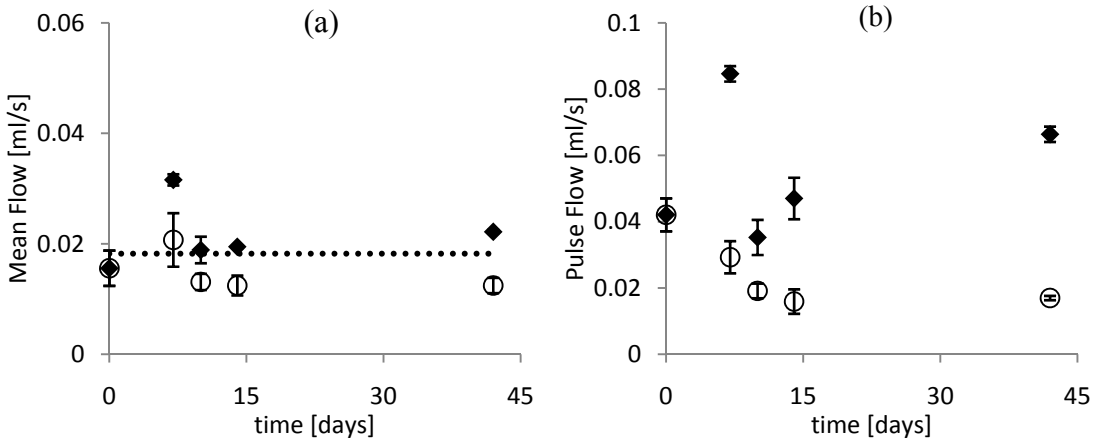

Figure 3.2. Hemodynamic measurements of a) mean flow with (- - -) representing the average of both vessels at all time points, b) pulse flow ($Q_{max} - Q_{min}$) for the RCCA-B (◆) and LCCA-B (○) at each time point: 0, 7, 10, 14, or 42 days post-banding surgery. Note, time=0 is before surgery and is considered the baseline test (CCA). Error bars represent standard error of the mean (n=4:7).

Biaxial mechanical testing was performed *in vitro* using both cyclic pressurization at a series of fixed stretches and cyclic axial extensions at a series at fixed pressures. Pressure-diameter testing revealed a large increase in outer diameter for RCCA-B vessels compared to CCA until 14 days and then a slight return toward baseline at 42 days (Figure 3.3a). A similar trend was experienced by LCCA-B vessels, but with a slight increase in diameter compared with CCA. The difference between 7 and 10 days were not significant for either vessel in the pressure-outer diameter or axial force-stretch plots. The force-stretch tests revealed increases in force for a given axial stretch as time went from 0 to 42 days in the RCCA-B, but little to no change in LCCA-B (Figure 3.3b). The RCCA-B force-stretch plots for 14-42 days were statistically similar and the LCCA-B force-stretch did not reach statistical significance for any time point compared to the CCA.

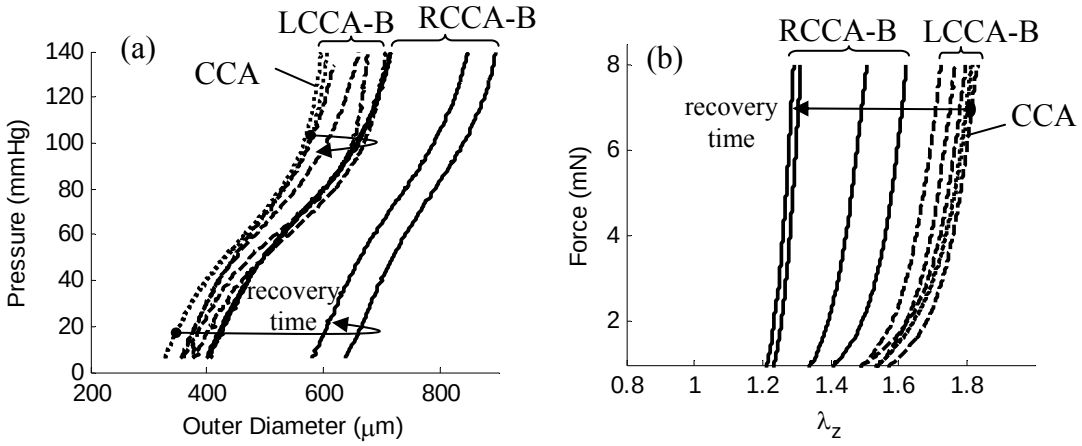

Figure 3.3. Cyclic biaxial mechanical test results for a) pressure-outer diameter at λ_z^{iv} and b) axial force-stretch at 100 mmHg for at each time point: 0 (CCA ----), 7, 10, 14, and 42 days post-banding surgery for both RCCA-B (—) and LCCA-B (- - -). Note that differences between 7 and 10 days were not significant ($p>0.05$) for either vessel in the outer pressure-diameter or force-stretch data. RCCA-B force-stretch plots at 14-42 days were statistically similar and the LCCA-B force-stretch did not reach statistical significance for any time point compared to the CCA ($p>0.05$). Arrows show the shift in diameter or force as time increases indicating a maximal outer diameter for both vessels at 14 days and force at 42 days.

Wall thickness at MAP changed in the RCCA-B vessels in the first 10 days (CCA=24.8±0.878, RCCA-B=46.1±0.531 μm) and then jumped dramatically (RCCA-B=99.0±8.43 μm) at day 14 (Figure 3.4a) and remained high through 42 days post-surgery. A less drastic change in thickness happened in the LCCA-B in the first 10 days (LCCA-B=42.0±1.52 μm). Differences in wall thickness occurred between the RCCA-B to LCCA-B at all time points after banding. At MAP (Figure 3.4b), the inner diameter increased (CCA=484±8.51 μm, RCCA-B at 14 days=680±32.0 μm) for the RCCA-B at each time point (excluding 7-10 days) until 42 days post-surgery where the vessel's diameter decreased from the previous time point (RCCA-B at 42 days=592±13.5 μm). Alternately, the LCCA-B increased and decreased throughout this time with an apparent mean inner diameter of approximately 507 μm and amplitude of 72.3 μm. When measured at a constant pressure of 100 mmHg (not

shown), the RCCA-B reached a peak at 14 days (CCA=496±8.92, RCCA-B=692±19.0) and again experienced a slight decrease in diameter at 42 days (RCCA-B=634±1.23 μm). At 100 mmHg, the LCCA-B oscillated around an equilibrium of approximately 544 μm with an amplitude of 61.1 μm.

A passive to active diameter ratio (Figure 3.4c), a measure of the ability of a blood vessel to contract, was determined by adding a vasoconstrictor (phenylephrine 10-5 M) and then a vasodilator (sodium nitroprusside 10-5 M) at 80 mmHg. The results suggested that the RCCA-B has less available smooth muscle contractility as post-surgical time went to 14 days and beyond as indicated by passive to active diameter ratio (CCA=1.62, RCCA-B=1.11, LCCA-1.71). An initial reduction in smooth muscle control happened in the first 10 days for both vessels while the LCCA-B returned to baseline (CCA) values.

The *in vivo* stretch (λ_z^{iv}) is the ratio of the in situ axial length to the unloaded length with the corresponding force required to hold the vessel in place, F^{iv}. There was a significant decrease in the *in vivo* axial stretch as post-surgery time proceeded to 14 days (Figure 3.5a). The RCCA-B *in vivo* stretch reached a minimum at 14 days (1.19 ± 0.067) and remained similar at 42 days while the LCCA-B changed little (1.67 ± 0.040) over time. The *in vivo* axial force (Figure 3.6b) changed for both vessels in the first 7 days after banding, but remained statistically insignificant to each other until 42 days where the RCCA-B decreased. The LCCA-B quickly located an equilibrium value of force (2.66 ±0.104 mN) after the first 7 days while the RCCA-B oscillated over the first 0-14 days; it located an equilibrium value (2.3±0.320 mN) at day 14.

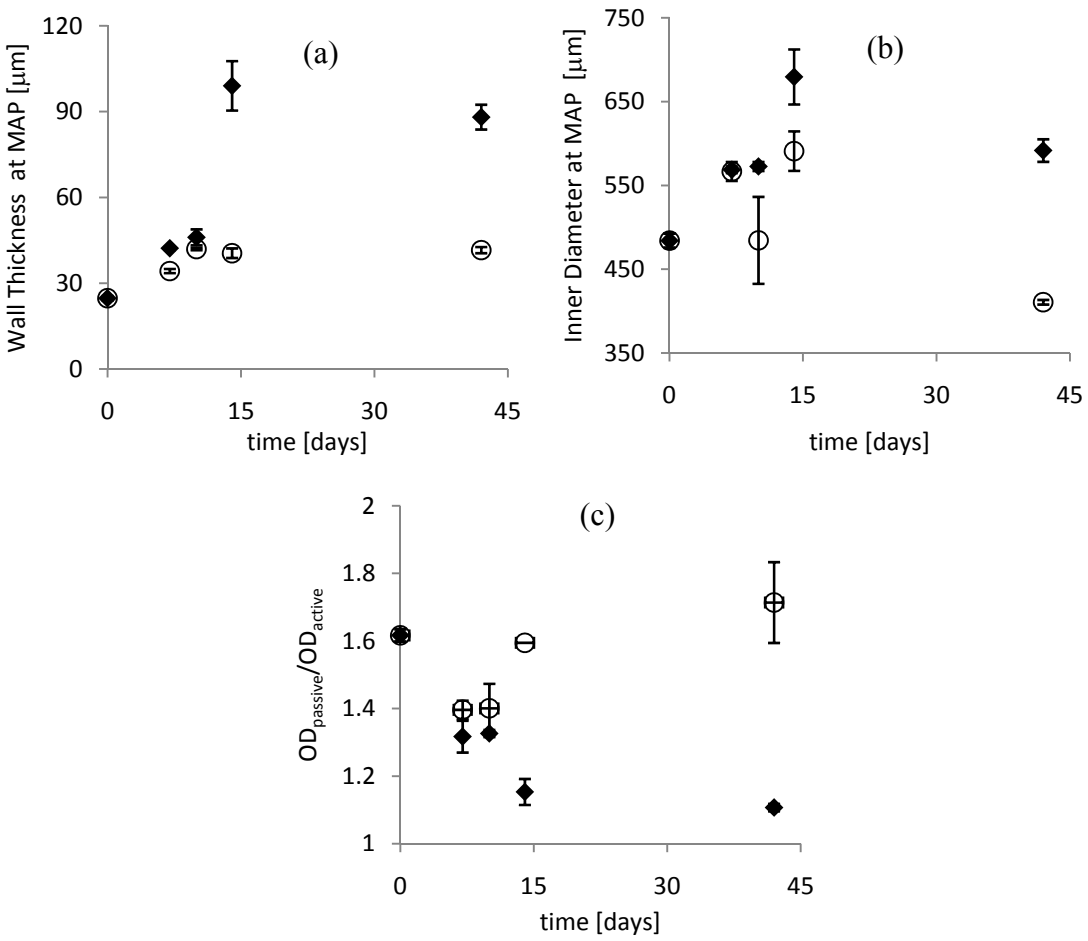

Figure 3.4. Carotid artery circumferential morphological variables at MAP: a) wall thickness, b) inner diameter, and c) smooth muscle dependent outer passive to active diameter ratio at 100 mmHg for the RCCA-B (◆) and LCCA-B (○) at each time point: 0, 7, 10, 14, and 42 days post-banding surgery. Note, time=0 is before surgery and is considered the baseline (CCA) test. Error bars represent standard error of the mean.

The circumferential stretch, calculated at the mid-wall, was virtually identical at all time points (see Figure 3.6a) for the RCCA-B when measured at pressures in the physiologic range (i.e., 70 to 140 mmHg). The LCCA-B experienced an oscillating change in circumferential stretch, similar to the diameter response, for a given pressure starting with a decrease in stretch vs. pressure from 0 to 7 days, then an increase from 7 to 14 days, then a decrease at 42 days.

Similarly, in Figure 3.6b, circumferential stress vs. stretch did not follow a distinct pattern, but oscillated around the baseline carotid artery (CCA) for both RCCA-B and LCCA-B.

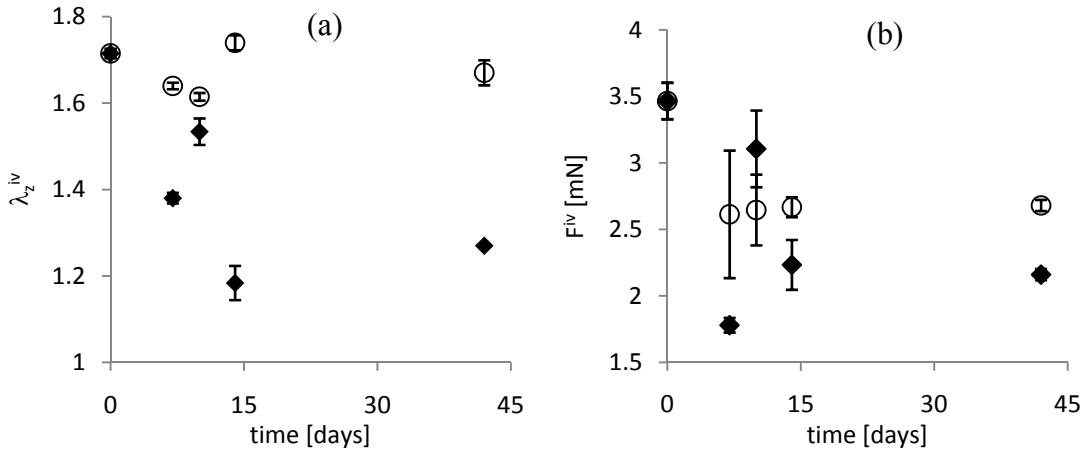

Figure 3.5. Carotid artery axial morphological variables: a) *in vivo* axial stretch, and b) *in vivo* axial force for the RCCA-B (◆), and LCCA-B (○) at each time point: 0, 7, 10, 14, and 42 days post-banding surgery. Note, time=0 is before surgery and is considered the baseline (CCA) test. Error bars represent standard error of the mean.

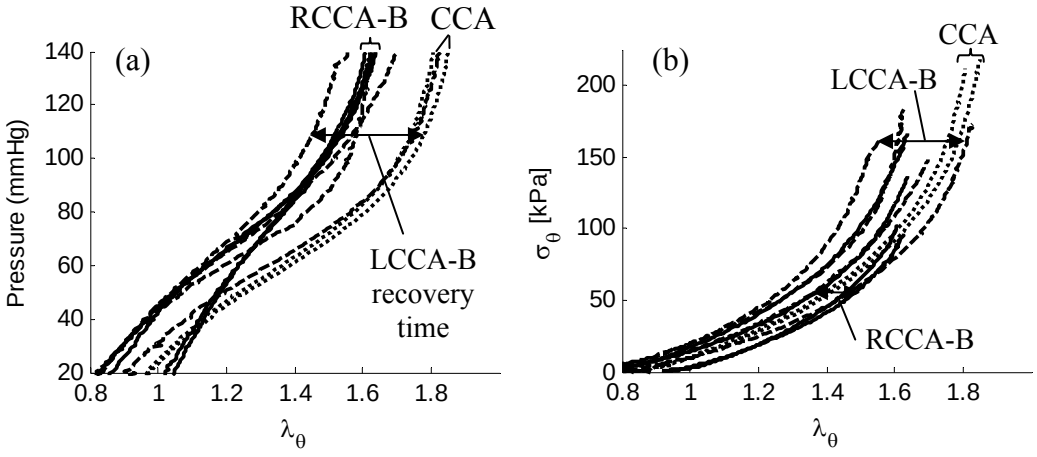

Figure 3.6. Mechanical test results for a) pressure vs. circumferential stretch and b) circumferential stress vs. stretch at each time point: 0 (CCA ----), 7, 10, 14, and 42 days post-banding surgery for both RCCA-B (——) and LCCA-B (- - -). Arrows indicate changes corresponding with post-surgical time.

Circumferential stress at systole (Figure 3.7a) in the RCCA-B reduced continuously after banding until 14 days (CCA=173±4.62, RCCA-B=81.0±10.5 kPa), then remained similar through 42 days, while LCCA-B circumferential stress at systole reduced after banding (LCCA-B =143±3.46 kPa) and reached a minimum of 89.9±6.82 [kPa] at 42 days. Likewise, the circumferential stress measured at MAP reduced continuously after banding surgery to 42 days (CCA=124±4.03, RCCA-B= 44.8±5.76 kPa) and was statistically insignificant from the LCCA-B until 14 days, and again converged at 42 days. The LCCA-B oscillated with a peak at 14 days (LCCA-B=111±8.19 kPa) and a minimum circumferential stress at 42 days (LCCA-B=53.1±7.63 kPa). This pattern is consistent with circumferential stress measured at diastole or 100 mmHg (data not shown). The change in the circumferential stress across the cardiac cycle (Figure 3.7c) were significantly reduced in the first 14 days after banding surgery for both RCCA-B and LCCA-B (CCA=91.9±8.75, RCCA-B=61.3±16.0, LCCA-B=65.2±5.26 kPa). The RCCA-B and LCCA-B had different changes in stress across the cardiac cycle during the first 0 days after banding (RCCA-B= 91.2±6.57, LCCA-B=74.8±10.0 kPa) but from 14 to 42 days such that they were statistically similar. This result suggests interplay between the balance of stress and the change in stress across the cardiac cycle with some tradeoff to achieve both goals. The axial stress and change in axial stress across the cardiac cycle (not shown) had similar trends to that found in the circumferential direction.

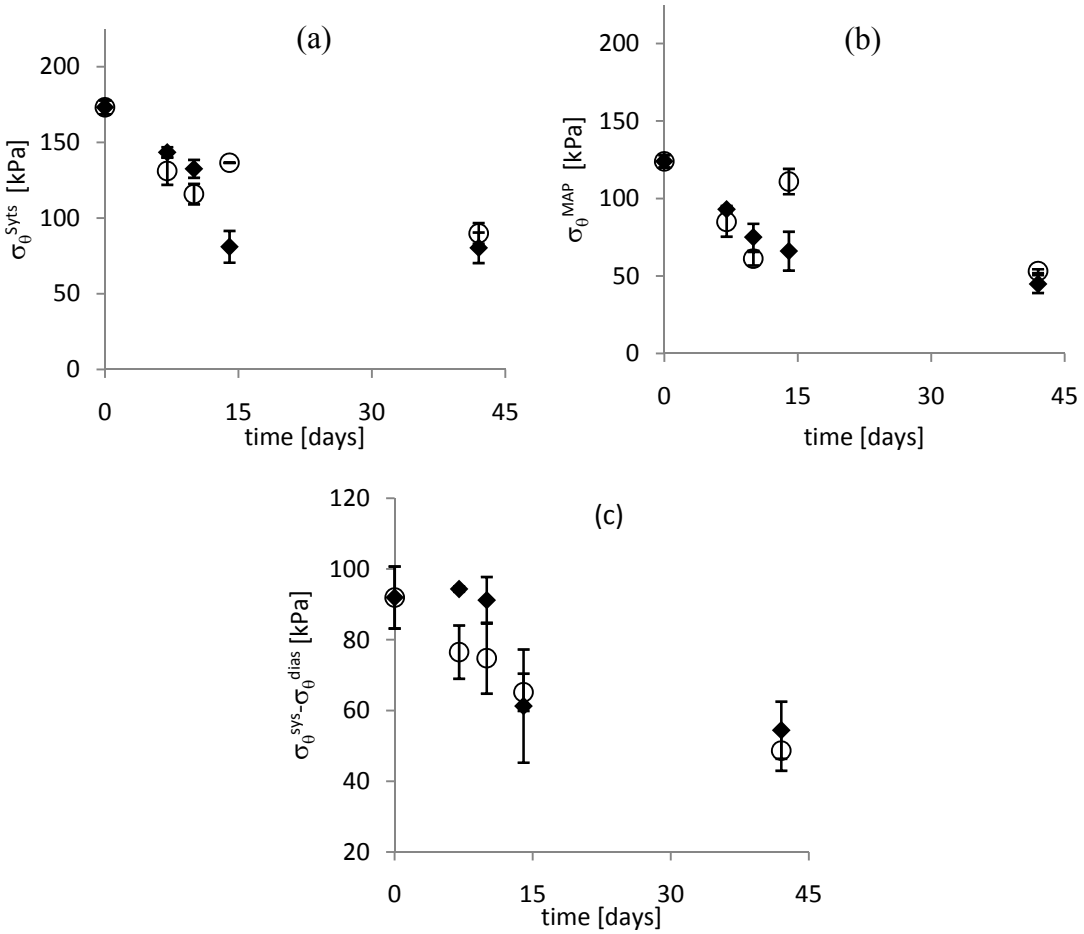

Figure 3.7. Time course of stress in the circumferential direction for a) systole, b) mean pressure, and c) the change in stress across the cardiac cycle for RCCA-B (◆) and LCCA-B (○) at each time point: 0, 7, 10, 14, or 42 days post-banding surgery. Note, time=0 is before surgery and is considered the baseline (CCA) test. Error bars represent ±SEM.

Representative results from histology using VVG and PSR-collagen darkfield can be viewed in Figure 3.8. VVG stained tissue (left) shows elastin as black and collagen/smooth muscle as pink, which can be compared to the birefringent collagen of PSR (right), with columns showing LCCA-B (left) and RCCA-B (right) at each time point after banding. It should be noted that there were wide variations at 14 days post-surgery in the RCCA-B, with some vessels appearing to take on characteristics of 10 day banded right vessels (Figure 3.8 g&p) and others

the 42 day banded right vessels (Figure 3.8 i&r). This response suggests a critical temporal transition toward the steady state remodeled tissue.

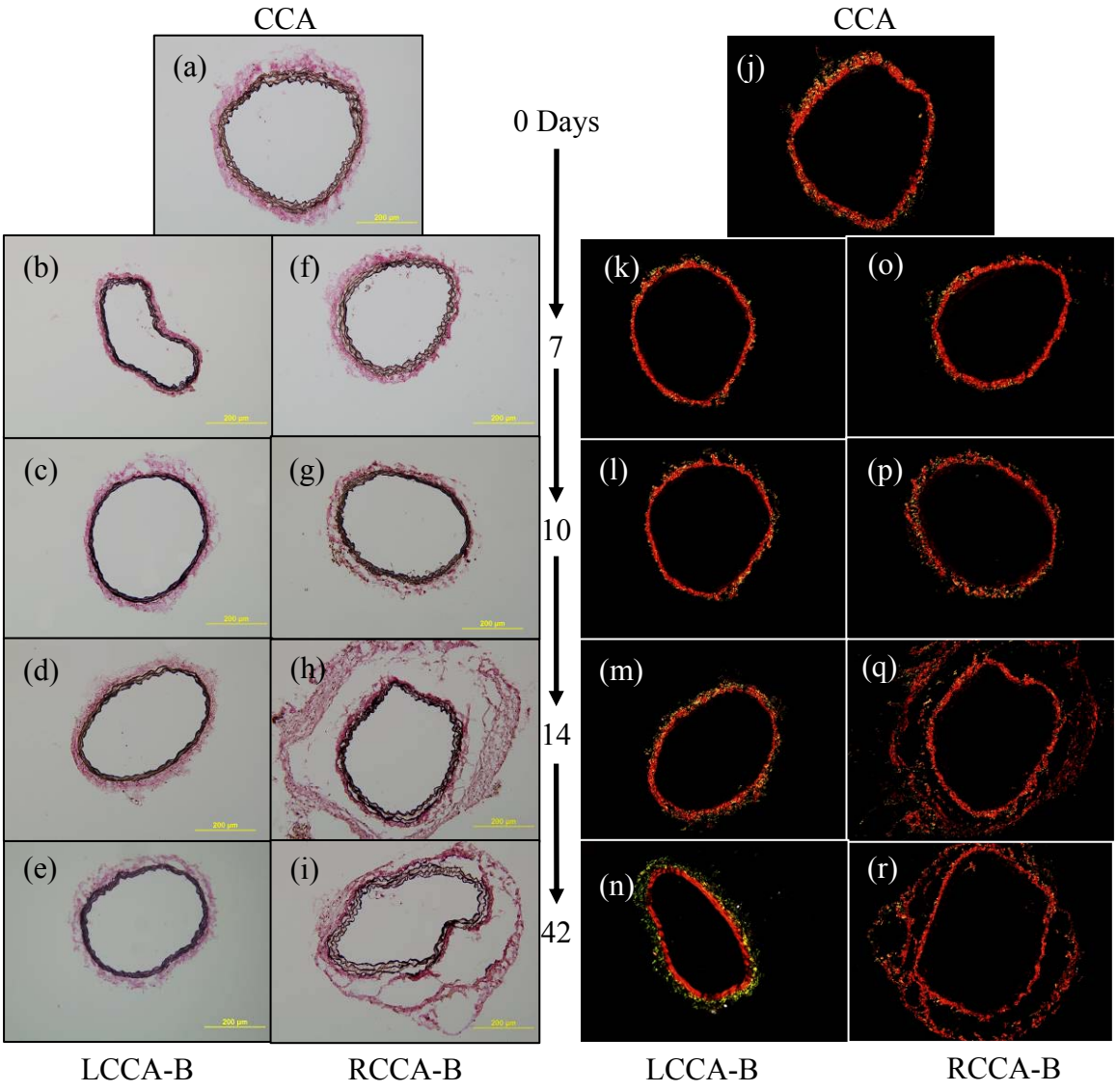

Figure 3.8. Representative histological staining for right (RCCA-B) and left (LCCA-B) carotid arteries at 0, 7, 10, 14, and 42 days after aortic banding surgery using: (a-i) Verhoeff-Van Gieson (VVG) to show elastin in black and (j-r) picrosirius red (PSR) multicolored collagen shown through birefringence. Note, RCCA-B image at time=10 days (Figures 3.8 g&p) only representative of half of the vessel while the others looked similar to those found at 14 days (Figure 3.8 h&q).

Thresholding analysis of VVG stained vessels showed little change in elastin fraction (ϕ^e) in the LCCA-B throughout remodeling while the RCCA-B experienced a reduction (CCA=0.358±0.001, RCCA-B=0.232±0.045, LCCA-B=0.397±0.043) after 42 days. This decrease in elastin mass fraction in the RCCA-B was due in part to a large increase in collagen mass fraction (CCA=0.223±0.056, RCCA-B=0.314±0.011, LCCA-B=0.257±0.002) after 42 days, while no significant change was experienced in the LCCA-B (Figure 3.9a). In fact, the collagen to elastin ratio (Figure 3.9b) yielded a steady increase in the RCCA-B without a significant change in the LCCA-B over 42 days (CCA=0.708±0.152, RCCA-B=1.487±0.26, LCCA-B=0.699±0.137). The number of cell nuclei stained using H&E (Figure 3.9c) revealed a gradual increase in nuclei number for the RCCA-B while changes in the LCCA-B remained insignificant over the 42 days (CCA=298±58.9, RCCA-B=578±28.3, LCCA-B=264±39.5 nuclei).

Discussion

Understanding better the time-dependent response of arteries to alterations in dynamic mechanical stimulation could be fundamental to the treatment of cardiovascular disease. In this work, we surgically altered the pulsatile mechanical characteristics of pressure and flow in mouse carotid arteries while changing their mean values very little. Previously we found that wall thickness and inner diameter correlated better with pulse pressure and pulse flow, respectively, than with mean values, well after banding surgery (42 days) and this relationship depended strongly on the role of the adventitia [26] (cf. Chapter II). Here we have identified the time course of remodeling as vessels seek to restore equilibrium values of stress and the change in stress across the cardiac cycle.

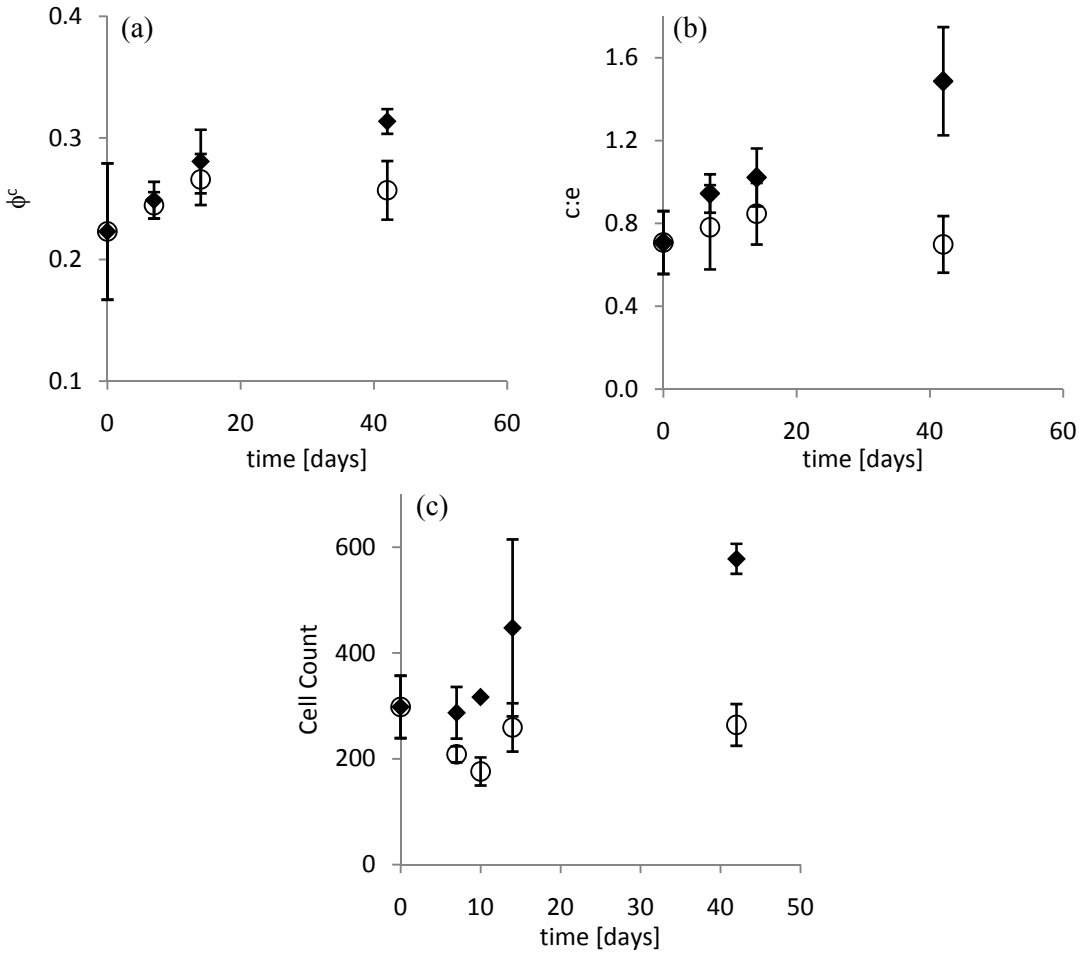

Figure 3.9. Time course results of histological analysis for a) collagen mass fraction, b) collagen to elastin ratio, and c) cell count for the RCCA-B (◆) and LCCA-B (○) at each time point: 0, 7, 10, 14, and 42 days post-banding surgery. Note, time=0 is before surgery and is considered the baseline test (CCA). Error bars represent standard error of the mean.

The surgical procedure called transverse aortic arch banding creates significant differences in pulsatile mechanical stimulation of the two carotids while maintaining mean values near baseline [26,55]. Hemodynamic changes occur rapidly after banding surgery due to the increased aortic resistance and diminished compliance forcing the pressure wave through the right carotid artery. Our results agree that this procedure causes a dramatic change in hemodynamics in the first 7 days, followed by a slight return towards moderate levels as tissue

supply is regulated via downstream resistance and changes in vessel wall microstructure [54,55]. For example, pulse pressure in the RCCA-B increased drastically in the first 7 (79.7±4.02 from 43.0±4.08 mmHg) days and remained higher than baseline throughout the study but decreased to 61.6±7.14 mmHg at 42 days. These findings are similar to those of Rockman *et al.* [52] who showed a general increase in systolic pressure in the RCCA-B or for the duration of their banding test (7 days) and Nakamura *et al.* [53] who showed increases in systolic pressure around 3 days. Likewise, in our experiment, the RCCA-B experienced a large increase in pulse flow in the first 7 days after banding but dropped after 42 days. Li *et al.* [55] also noticed that mean velocities remained similar between right and left carotids after banding surgery. If their carotid artery diameter increased, as it did in ours, mean volumetric flow rate would also have increased at day 7 and would thus be similar to our findings. Still, peripheral adaptation appears to take place to bring blood flowrates closer to baseline after a long-term remodeling period. This adaptation was shown to be delayed in aged subjects [54], however, where pulse transmission is already high [21]. Guyton and Hartley [24] showed that inner diameter correlates strongly with peak flow velocity and pulsatile, not mean, flow on clipped carotid arteries of rats that were allowed to recover for 39 to 82 days. The inner diameter in our case peaked around 14 days with a slight return towards baseline at 42 days [68]. What happens between time points remains unclear, but may involve some oscillation that could be a direct result of hemodynamic overshoot, delayed arterial remodeling, or both.

Our results show that most of the arterial remodeling occurred in the first 14 days (cf., Figures 3.4 a&b), similar to findings of Hu *et al.* [64]. The cascade of arterial responses to altered mechanical stimuli starts with the endothelial and vascular smooth muscle cells. Endothelial response to altered wall shear stress (e.g., altered production of endothelin-1 and nitric oxide) can be very fast [69], which in turn induces rapid changes in smooth muscle

contractility that are followed by an altered production of growth factors and proteases that aid in structural reorganization; this is followed by significant matrix deposition. In our study, wall thickness peaked around 14 days with a slight return towards baseline at 42. The increased thickness was attributed to an increase in both collagen and cell number [26], and correlated better with pulse pressure than mean pressure [22,23,26] (cf. Chapter II). Boutouyrie *et al.* [23] similarly found that pulsatile pressure correlates better with arterial wall intima-medial thickening than mean pressure in human carotids in hypertension.

It is widely held that arteries increase and decrease wall thickness and diameter in an attempt to equilibrate stresses. There is one caveat, however, with regard to our observed increases in wall thickness and associated decreases in calculated wall stresses and change in stress across the cardiac cycle in the RCCA-B carotids. Much of the thickening occurred in the adventitia and some of this material appeared to be looser or less well organized than that in the CCA and LCCA-B carotids. It is possible, therefore, that not all of the tissue included in the measured thickness was fully load bearing, which is to say that the "effective wall thickness" may have been overestimated and the wall stresses underestimated. There is a need to pursue this possibility further. Indeed arterial biomechanics would benefit by better quantification of the load-carrying capability of new cells and matrix during rapid periods of turnover for this is fundamental to understanding the overall growth and remodeling process. There is a desire, for example, to understand better the interactions between newly produced and extant collagen fibers as well as interactions between collagen fibers and other constituents within the matrix, including proteoglycans. Alberding *et al.* [70] showed increased permeability of the wall in carotid arteries subjected to higher pulsatility and that a sudden onset of hypertension could cause interstitial edema. Walker-Caprioglio *et al.* [71] reported that proteoglycan synthesis within arteries was increased significantly in a spontaneously

hypertensive rat model, particularly in carotids, but there has been little attention since on the direct mechanical contributions of changing proteoglycan levels. Revnertson *et al.* [72] reported similar findings in aorta.

There is similarly a need to focus more on the mechanobiological responses of the adventitial fibroblasts. Whereas it has long been thought that hypertension initially increases the stresses in the inner portion of the wall [73], thus leading first to subintimal or medial remodeling, significant early remodeling was observed herein in the adventitia. For example, 69% of the cell nuclei at 42 days were in the adventitia in the hypertensive RCCA-B compared to 26% in the contralateral LCCA-B [26] (cf. Chapter II). These findings are consistent with the increasing evidence that adventitial fibroblasts play a much greater role in diverse cases of arterial remodeling than long thought [74-77]. Fibroblasts may be fundamental to controlling the change in stress across the cardiac cycle and preventing over-distension as evidenced by this aortic banding model of increased pulsatility. For example, comparing the RCCA-B to the LCCA-B, the arteries herein seemed to achieve an altered state of stress equilibrium (Figure 3.7b) until 14 days at which time the right and left carotids diverged in many ways. At this same time, the change in stress across the cardiac cycle (Figure 3.7c) converged between left and right vessels, and by 42 days post-surgery both RCCA-B and LCCA-B had close but not the same values of stress at mean pressure and stress change in stress across the cardiac cycle. This overshoot may be a cause or effect of the hemodynamic overshoot.

Additional research is needed to elucidate this relationship, which may be due in part to altered smooth muscle control. Although this chapter does not identify smooth muscle phenotype, the availability of the smooth muscle to change the wall diameter is 7-times greater in the LCCA-B than the RCCA-B (Figure 3.4c). Hu *et al.* [64] found similar decreased contractility and a shift toward a synthetic phenotype that peaked at 14 days in a pig aortic

coarctation model. The rate of cell proliferation may have been highest at 14 days and leveled off at 42 days in our model. Furthermore, Reccia *et al.* [67] showed that short term vasoactive responses of ex vivo tested porcine carotid arteries maintain an increased diameter, independent of the endothelium, in response to increased pulse pressure. At the extra cellular matrix level, the collagen mass fraction (ϕ^c) was increased greatly at 14 days similar to that found by Hu *et al.* [64]. By comparing circumferential stretches instead of diameters (Figure 3.6a), vessels had no statistical difference in stretch between banding times when operating near physiologic pressures due, in part, to an evolving unloaded configuration. This observation may be illuminated in the axial direction by the increase in force for any given stretch (Figure 3.3) as time progressed in the RCCA-B. Arteries may use the axial direction to compensate for remodeling to achieve balanced wall shear and changes in circumferential stress [78] . After all, the force required to keep the blood vessel at this extension is a function primarily of the extracellular matrix protein elastin, which does not increase in mass fraction as the vessel grows in hypertension (Figure 3.9).

It appears that arteries remodel in a manner such that convergence to an optimal geometry may be an iterative process. One potential hypothesis is that the vessels may undergo an active/passive increase in non load bearing wall constituents, including reticular collagens and proteoglycans, contributing to the overall wall thickness but not function. Alternately, the production and removal rates of wall constituents, or the hemodynamic stimuli, may experience a large "overshoot" and would require growth and remodeling equations to be second order. This control mechanism may be attempting to achieve a balance of both stress and the change in stress across the cardiac cycle. A complete understanding of arterial remodeling in response to alterations in pulsatile pressure and flow is crucial to understanding native arterial tissue and the function of tissue engineered constructs. The information learned herein can be used to improve

time-based constitutive models of arterial reorganization by quantifying mass-production terms as a function of pulsatile stimulus.

CHAPTER IV

ALTERED BIAXIAL MECHANICAL PROPERTIES OF CAROTID ARTERIES IN AN AORTIC ARCH BANDING MOUSE MODEL OF HYPERTENSION

Overview

Quantification of the time course of load-induced changes in wall properties is fundamental to developing models of arterial growth and remodeling, which in turn are essential to predicting disease progression and potential treatment outcomes. Arteries adapt to altered pulsatile pressure and flow by modifying wall thickness, inner diameter, and axial length via marked cell and matrix turnover. To identify biomechanical implications of such adaptations, we used a 4-fiber family constitutive relation to quantify the biaxial mechanical properties of mouse carotid arteries 0 (baseline), 7, 10, 14, or 42 days after an aortic arch banding surgery that augmented pulsatility in the right but not the left carotid. We found dramatic increases over time in strain energy, at any biaxial stretch, in the hypertensive right compared to the nearly normotensive left carotid. This net stiffness increase occurred via an increase in the anisotropic contribution despite a decrease in the isotropic contribution to the strain energy. Yet when comparing vessels near their *in vivo* stretch, the strain energy was lower in the right than in the left carotid indicating that overall stored energy has not increased in pulsatile remodeling. It appeared that the period 7 to 10 days after the onset of increased pulsatile stimuli in the right carotid was a time of transition. Moreover, at its peak (2 wks), wall thickness was approximately 1.8 times greater than needed to restore biaxial stresses to baseline, perhaps indicating an over-abundance of newly synthesized non-tensile bearing constituents, an initial overcompensation, or

an attempt to restore additional homeostatic targets (e.g., changes in stress across the cardiac cycle).

Introduction

Hypertension occurs when resting systolic or diastolic blood pressures rise above 140 or 90 mmHg, respectively [1], with the rise in pulse pressure being particularly important. That is, pulsatile characteristics of blood pressure and flow cause marked changes in arterial wall geometry and composition [16,23,24,26] and should be considered as important stimuli in mathematical models of growth and remodeling. Of particular note, otherwise stable elastin can be fragmented by the heightened cyclic loading of hypertension [37,79,80] and there is a significant cyclic stretch-induced increase in the synthesis of collagen, particularly in the adventitia [74,81,82]. There is a pressing need, however, to model biomechanical consequences of the associated time course of changes in mass fraction, orientation, and turnover of structurally significant constituents within the wall as an artery attempts to recover a homeostatic state [83].

In this chapter, we quantify the time course of altered biaxial mechanical properties of mouse carotid arteries over the first 42 days of hypertension. The associated time course of experimentally measured changes in pressure-diameter and axial force-length responses can be found elsewhere [27] (Chapter III). Briefly, a murine aortic arch banding model [26,27,52,55] (cf. Chapters II, III) was used to differentiate pulsatile pressure and flow in paired common carotid arteries, with the right common carotid artery after banding (RCCA-B) experiencing hypertension and the left carotid after banding (LCCA-B) remaining nearly normotensive. A structurally motivated 4-fiber family constitutive relation [29] was used to quantify the biaxial mechanical properties at 0, 7, 10, 14, or 42 days after banding; best-fit values of the associated material parameters were determined by minimizing an objective function based on differences

in model predicted and experimentally measured stresses. Results are presented primarily in terms of the strain energy stored in the arteries at different states of biaxial stretch, which is a convenient scalar metric of overall stiffness. Motivated by a desire to improve the predictive response of arteries subjected to altered pulsatile stimulation, the results demonstrate marked changes in mechanical properties associated with the previously reported significant changes in wall geometry and composition due to the progression of hypertension.

Materials and Methods

Experimental Data. Common carotid arteries from mature male wild-type C57BL/6J-129Sv mice were studied mechanically at 0 (n=7), 7 (n=5), 10 (n=4), 14 (n=5), or 42 (n=6) days following aortic arch banding [26,27,52,55] (cf. Chapters II, III), which increases pulse pressure in the RCCA-B but leaves the LCCA-B nearly normotensive. Following preconditioning, specimens were held at the experimentally determined in-vivo stretch (λ_z^{iv}) and subjected to slow, cyclic pressurization from 0-140 mmHg. The same protocol was repeated at 5% above and 5% below the in-vivo axial stretch. Although results at basal smooth muscle tone can be found in Eberth *et al.* [27] (cf. Chapter III) all data in this chapter were collected under passive conditions by testing in Hanks Balanced Salt Solution supplemented with sodium nitroprusside (10^{-5} M) and EGTA ($2x10^{-3}$ M).

Mid-wall circumferential (λ_θ), axial (λ_z), and radial (λ_r) stretches were calculated via

$$\lambda_\theta(s) = \frac{r}{R(s)}, \quad \lambda_z(s) = \frac{\ell}{L(s)}, \quad \lambda_r(s) = \frac{1}{\lambda_\theta(s)\lambda_z(s)} \tag{4.1-4.3}$$

where r and R are radii located midway between the intima and the adventitia in current and reference configurations, respectively, and ℓ and L are axial lengths in current and reference configurations. The notation $R(0)$ or $L(0)$ refers to unloaded values before banding whereas

$R(s)$ or $L(s)$ denote any evolving unloaded configuration (i.e., at s =7, 10, 14, or 42 days). Experimentally "measured" mean circumferential and axial Cauchy wall stresses are given by

$$\sigma_\theta^{\exp} = \frac{P\, r_i}{r_a - r_i}, \qquad \sigma_z^{\exp} = \frac{f_T + P\pi r_i^2}{\pi\left(r_a^2 - r_i^2\right)} \tag{4.4-4.5}$$

where P is the transmural pressure, f_T is the axial force measured by the in-line transducer, and subscripts i and a denote intimal and adventitial, respectively.

Constitutive Model and Parameter Estimation. The mechanical properties were quantified using a 4-fiber family constitutive relation that describes biaxial data well for both cerebral (rabbit basilar) and carotid (mouse) arteries [29,30,84,85]. Briefly, this relation is based on the assumption that the dominant contributors to load bearing are an isotropic, elastin-dominated amorphous matrix, multiple families of oriented collagen fibers (axial, circumferential, and diagonal), and passive smooth muscle (circumferential). The associated strain energy function takes the form

$$W = \frac{c}{2}\left(\lambda_\theta^2 + \lambda_z^2 + \lambda_r^2 - 3\right) + \sum_{k=1-4} \frac{c_1^k}{4c_2^k}\left\{\exp\left[c_2^k\left(\left(\lambda^k\right)^2 - 1\right)^2\right] - 1\right\}, \tag{4.6}$$

$$\lambda^k = \sqrt{\lambda_\theta^2 \sin^2\alpha_o^k + \lambda_z^2 \cos^2\alpha_o^k} \tag{4.7}$$

where c, c_i^k are material parameters and α_o^k is the angle between diagonally oriented collagen fibers and the axial direction in the reference configuration; the superscript k denotes each of the four fiber families (1 = axial, 2 = circumferential, and 3,4 = symmetrically oriented diagonal fibers). Consistent with prior findings (e.g., [29,30,84,85]), we assumed the diagonal fibers possessed the same properties, hence $c_1^3 = c_1^4$, $c_2^3 = c_2^4$. Assuming plane stress (i.e., $\sigma_r << \sigma_\theta$ and $\sigma_r << \sigma_\theta$), the non-zero components of the Cauchy stress can be computed in circumferential and axial directions as

$$\sigma_\theta^{\text{mod}} = \lambda_\theta \frac{\partial W}{\partial \lambda_\theta} - \lambda_r \frac{\partial W}{\partial \lambda_r},\ \sigma_z^{\text{mod}} = \lambda_z \frac{\partial W}{\partial \lambda_z} - \lambda_r \frac{\partial W}{\partial \lambda_r} \tag{4.8-4.9}$$

where all stretch ratios (λ) were computed at the current growth and remodeling time (s). The 8 unknown material parameters within equations 4.6-4.7 were found by minimizing the sum of the squares of the differences between experimentally measured (exp) and theoretically modeled (mod) biaxial stresses, namely by minimizing

$$e = \sqrt{\frac{\sum_{i=1}^{N}\left(\sigma_\theta^{\text{exp}} - \sigma_\theta^{\text{mod}}\right)^2}{\sum_{i=1}^{N}\left(\sigma_\theta^{\text{exp}}\right)^2}} + \sqrt{\frac{\sum_{i=1}^{N}\left(\sigma_z^{\text{exp}} - \sigma_z^{\text{mod}}\right)^2}{\sum_{i=1}^{N}\left(\sigma_z^{\text{exp}}\right)^2}} \tag{4.10}$$

where N is the number of data points [30], with data from the multiple biaxial protocols combined for each specimen separately. This minimization was accomplished using a simplex method [30]. Because of the difficulty of assessing specimen-to-specimen differences based on 8 best-fit material parameters in a highly nonlinear model [86] , assessments were based primarily on the total strain energy stored in each artery in response to comparable deformations.

Results

The 4-fiber family model was fit to the biaxial data (comparable to that shown in Chapter III but in the passive state), similar to prior findings for carotid arteries from other mouse genotypes [29,30,85] (cf. Chapter V), with best-fit values of the material parameters changing due to hypertension and its time course. Values of the strain energy W averaged separately for RCCA-B and LCCA-B at the different end-points revealed an increasingly stiffer behavior in hypertension at high stretches (Figure 4.1). Note that W is plotted versus the biaxial state of stretch ($\lambda_\theta, \lambda_z$), with λ_θ and λ_z ranging from those stretches tested experimentally. Further, the W measured at each time point from stretches corresponding to those found in the

baseline carotid artery at $t = 0$, ($\lambda_\theta = \lambda_z = 1-1.75$) are superimposed on the figures as a white grid for comparison purposes.

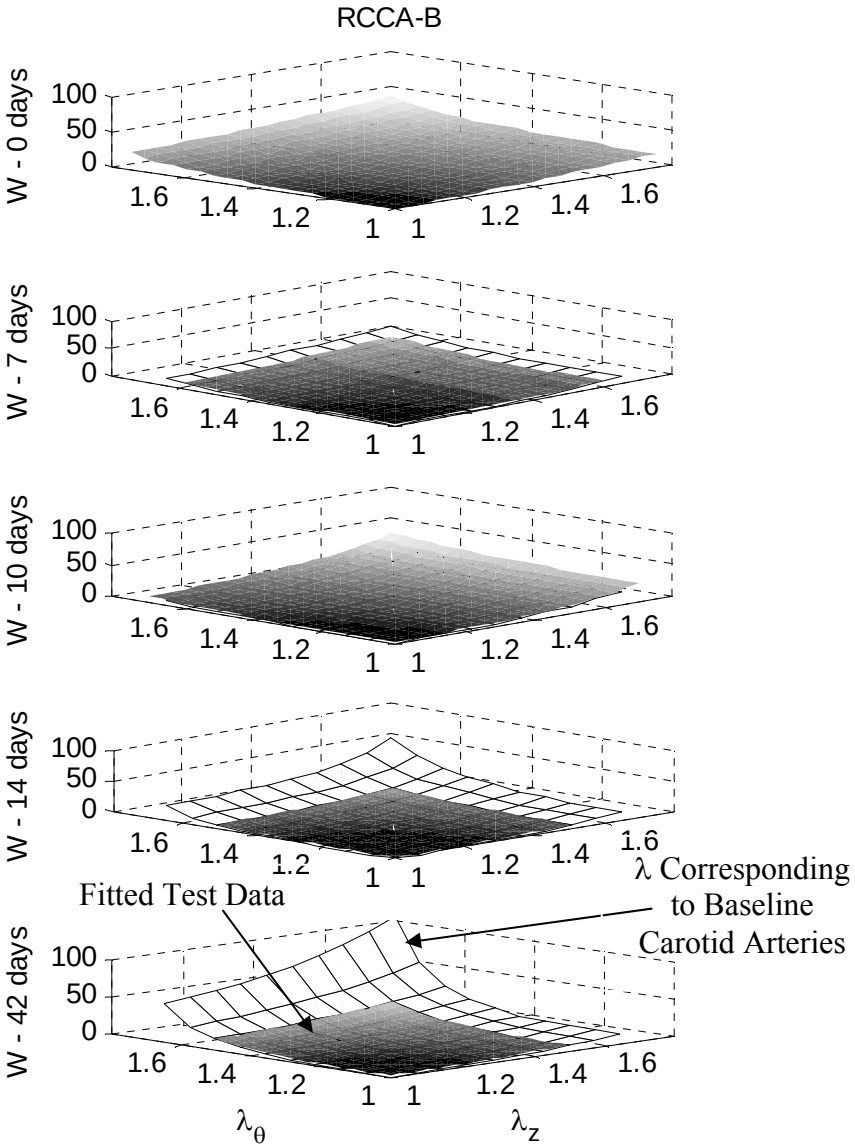

Figure 4.1. Averaged values of total strain energy (W) per unit area (kPa) vs. stretch in the circumferential (λ_θ) and (λ_z) axial direction for the right carotid artery before banding (0 days) and after banding (RCCA-B) at 7, 10, 14, or 42 days post-surgery. Low values of W under actual test conditions (λ_θ and λ_z measured) are shown as solid grayscale colors with increasing values getting lighter. Strain energy extrapolated at stretches similar to those found at baseline ($\lambda_\theta = 1-1.75$ and $\lambda_z = 1-1.75$) are displayed as a white grid.

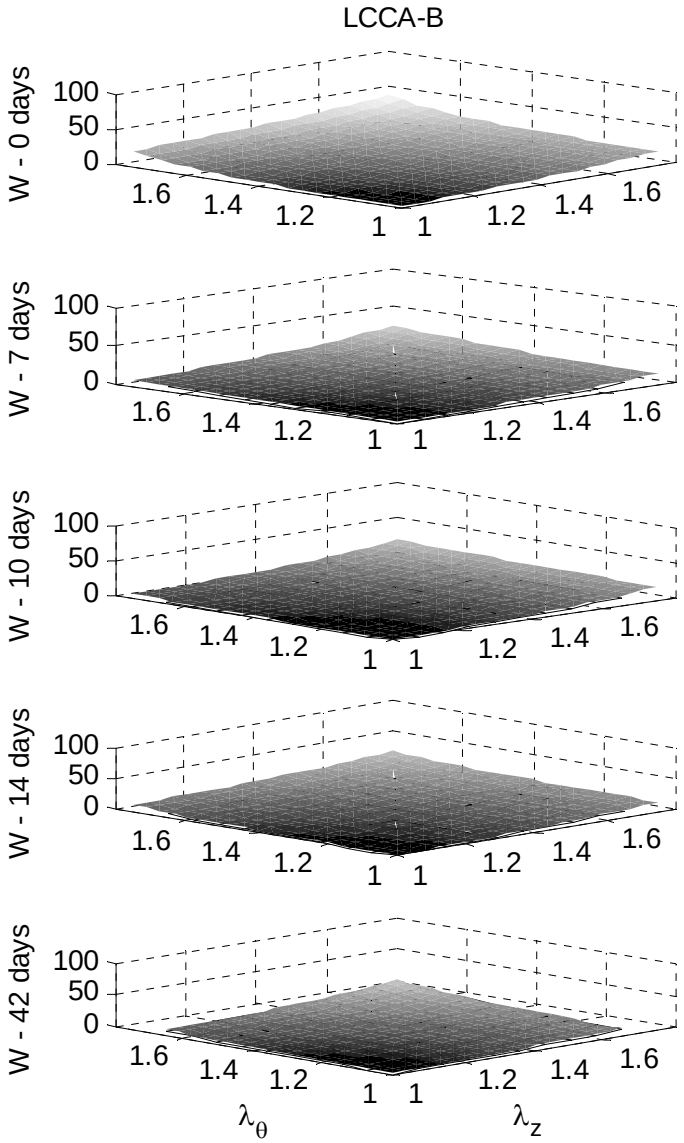

Figure 4.2. Averaged values of total strain energy (W) per unit area (kPa) vs. stretch in the circumferential (λ_θ) and (λ_z) axial direction for the left carotid artery before banding (0 days) and after banding (LCCA-B) at 7, 10, 14, or 42 days post-surgery. Higher values of strain energy are displayed in white.

Although moderate changes were revealed by the averaged data for the RCCA-B over the first 10 days, specimen-to-specimen variation was high at 7 and 10 days – some vessels had a strain energy similar to the average found at 14 days while others were closer to native tissue (0

days). Averaged values of strain energy for the LCCA-B revealed little change over time as expected (Figure 4.2), albeit a slight increase at 42 days.

The mean fiber angle $\alpha_o^{3,4}$ calculated by parameter estimation for the diagonal collagen fibers (k = 3,4) initially increased for both the RCCA-B and the LCCA-B (i.e., became more circumferential), but eventually decreased for the RCCA-B (i.e., became more axial). Angular approximations may not reflect the true condition of the tissue (i.e., collagen may be in a state of assembly/disassembly or undulation) but when combined with the magnitude of the unknown parameter (c_1^3, c_2^3) provide a realistic approximation of the overall diagonal representation of the collagen fibers. Again, there was some indication of an early, marked remodeling in hypertension around 7 to 10 days, followed by long-term response that corresponded to a stiffer axial force-length response (cf. [26,27], Chapter II,III). A sample of representative fiber angles from experimentally fitted results can be seen in Table 4.1. The variation of unknown material parameters in the RCCA-B at 7, 10, and to a lesser degree 14 days was large with results lying at either side of the spectrum (i.e., similar to 0 or 42 days) and rarely near the mean except for the fiber angle. This variation indicates that there is some differences in the recovery of individual mice subjected to hypertension and highlights some of the variability in the banding procedure described previously.

Table 4.1. Sample of best-fit parameters for a 4-fiber family model determined using the simplex method for each time point in the RCCA-B and LCCA-B at 0 (CCA), 7, 10, 14, and 42 days post-banding surgery. (*). Note, values used in Figures 4.1, 4.2 and 4.4 are from averages at each time point rather than the individual samples shown in this table.

	fiber family:	k	1	1	2	2	3	3		
	Post-Surgery Time [days]	c [kPa]	c_1 [kPa]	c_2	c_1 [kPa]	c_2	c_1 [kPa]	c_2	$\alpha_0^{3,4}$ [Deg]	Error
RCCA-B	42	2.375	4.032	1.000	11.05	5.6E-17	16.52	1.000	23.1	0.285
	14*	5.904	1.869	1.000	5.408	1.5E-15	4.075	0.666	33.9	0.130
	10*	6.340	0.001	0.032	12.45	1.0E-11	7.003	0.507	41.2	0.123
	7*	8.535	0.001	1.8E-12	13.12	3.3E-16	6.816	0.872	34.3	0.152
CCA	0	12.79	9.44	0.10	10.72	0.05	0.51	0.87	33.5	0.08
LCCA-B	7	11.30	0.001	4.1E-13	0.001	6.5E-13	4.361	0.501	52.5	0.154
	10	6.254	1.121	0.201	0.001	0.453	3.709	0.245	41.5	0.122
	14	7.345	0.001	0.647	0.001	0.442	2.421	0.199	45.3	0.110
	42	9.677	0.008	0.965	1.737	0.002	19.37	0.344	57.3	0.146

The isotropic part of the strain energy W_{iso} is shown in Figure 4.3 for the RCCA-B, with λ_θ and λ_z again ranging from stretches tested experimentally and superimposed with those found in the baseline carotid artery at $t = 0$, ($\lambda_\theta = \lambda_z = 1 - 1.75$) for comparison purposes. Note the continued decrease in W_{iso} over time despite the aforementioned overall increase in strain energy over time (cf. Figure 4.1). Although changes began within the first 7 to 10 days, they were amplified greatly at 14 to 42 days. Note that W_{iso} formed a symmetric plane as it should, by definition, due to equal contributions to the total energy at equibiaxial stretches. Plots for LCCA-B over time appeared very similar to W_{iso} at 0 days (baseline) despite a slight decrease over the remodeling time course (not shown). Anisotropic contributions to the strain energy are not shown simply because they can be inferred via the subtraction $W - W_{iso}$. Consistent with Figures 4.1 and 4.2, the anisotropic contribution to the strain energy increased markedly for RCCA-B, but not LCCA-B. This is consistent with an increased deposition of collagen during hypertension

[26,27] (cf. Chapter III), much of which was adventitial and contributed to the change in $\alpha_o^{3,4}$ shown in Table 4.1.

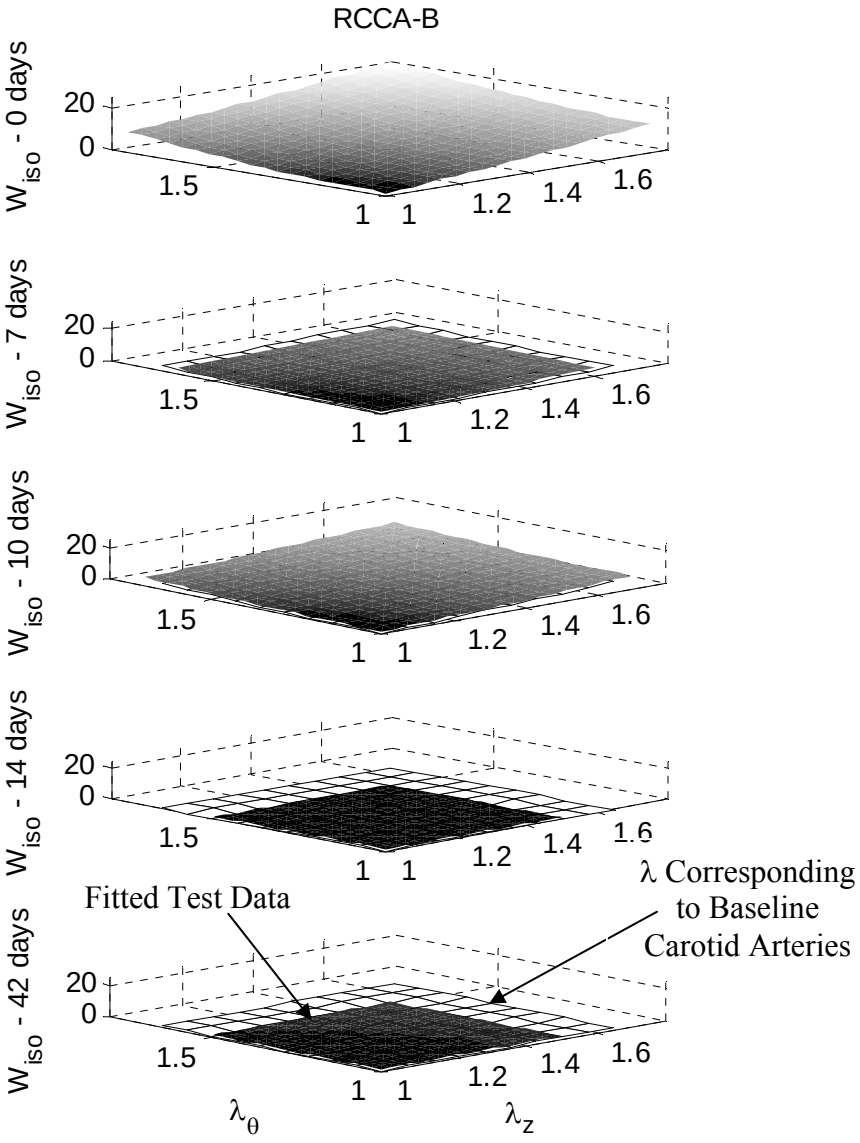

Figure 4.3. Averaged values of the isotropic part of the strain energy W_{iso} (kPa) versus stretch in the circumferential (λ_θ) and axial (λ_z) directions for the hypertensive right carotid artery (RCCA-B) before (0 days) and after (at 7, 10, 14, or 42 days post-surgery) banding. Low values of W under actual test conditions (λ_θ and λ_z measured) are shown as solid grayscale colors with increasing values getting lighter. Strain energy extrapolated at stretches similar to those found at baseline (CCA: $\lambda_\theta = 1-1.75$ and $\lambda_z = 1-1.75$) are displayed as a grid.

It is important to consider the range of stretches that an artery might experience *in vivo* when interpreting three-dimensional plots of strain energy. The isotropic (W_{iso} - Figure 4.4a) and anisotropic (W_{anis} - Figure 4.4b) contributions to the strain energy (W - Figure 4.4c) were calculated for the RCCA-B and LCCA-B at stretches corresponding to individual vessel's mean arterial pressures (MAP) and *in vivo* axial extensions λ_z^{iv} (which were significantly less in the RCCA-B after 42 days of hypertension; [26] Chapter II). The RCCA-B experienced a marked decrease in W ($p<0.001$) at this condition over the 42 days of remodeling, with considerable variability at 7-14 days. Interestingly, the anisotropic contributions (Figure 4.4b) at stretches corresponding to MAP were similar in the RCCA-B and LCCA-B. The strain energy corresponding to the individual vessel's systolic pressure and λ_z^{iv} are plotted for strain energy (W_{iso}, W_{anis}, and W) in Figure 4.4. The strain energy corresponding to stretches found at systole were only slightly greater than those found at MAP for either vessel.

The circumferential stretches λ_θ^{MAP} used to calculate strain energy at physiologic conditions (Figure 4.4c) can be seen in Figure 4.5a. Values for the RCCA-B were similar to those for the LCCA-B at all times. If the composition of elastin changed little throughout remodeling, it would be appropriate to compute stretches with respect to the unloaded configuration of the baseline vessels. Using baseline conditions as a reference, the RCCA-B had a greater stretch at MAP (Figure 4.5b); the evolution of the unloaded configuration reinforces this finding (Figure 4.5c).

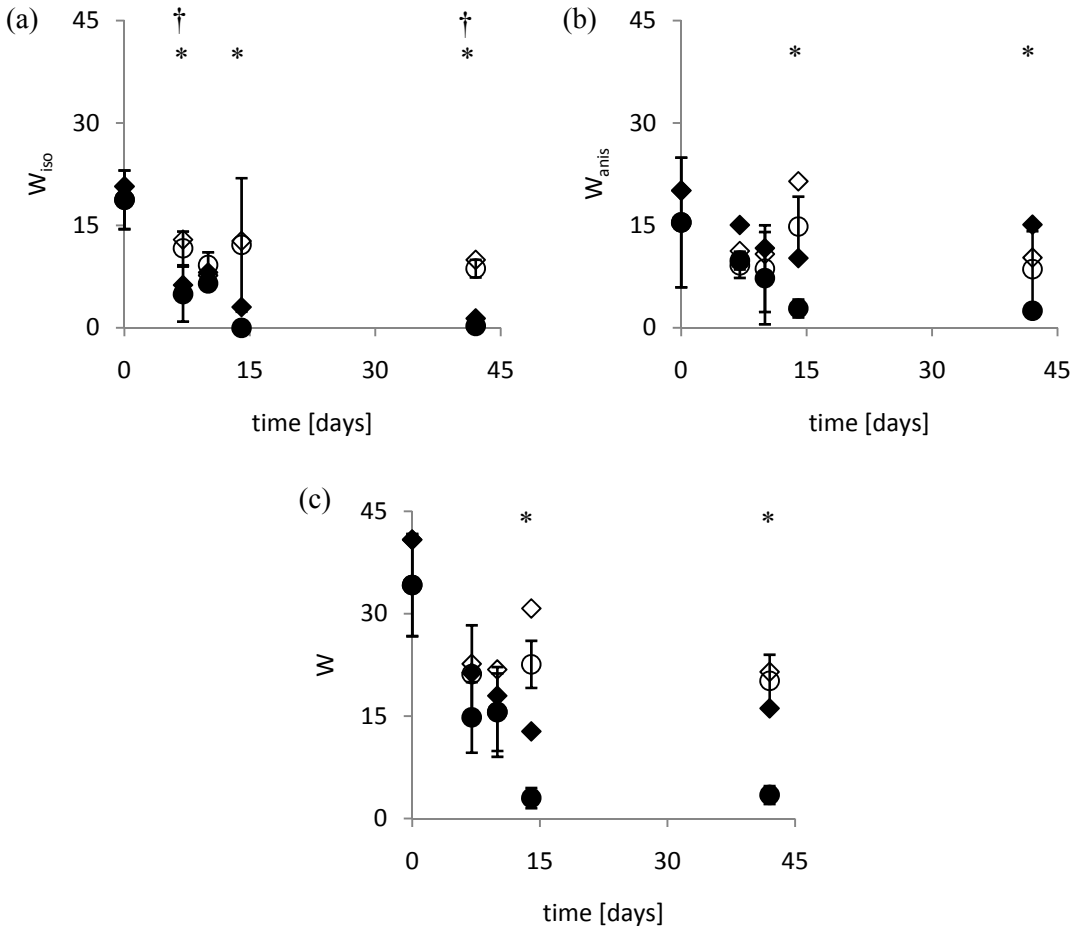

Figure 4.4. Strain energy (W) at physiologic operating points corresponding to mean arterial pressure and systole (λ_θ^{MAP}: λ_θ^{SYS}, λ_z^{iv}) for each time point considering a) the isotropic contribution W_{iso}, b) the anisotropic contribution W_{anis}, and c) the total energy W for the RCCA-B (◆) and LCCA-B (○) at MAP and the RCCA-B (◇) and LCCA-B (◆) at systole as time progresses after aortic banding surgery. Bars represent ± standard deviations for λ_θ^{MAP} only to simplify the graph. (∗) indicates values of statistical significance at λ_θ^{MAP} and (†) shows statistical significance at λ_θ^{SYS} between RCCA-B and LCCA-B.

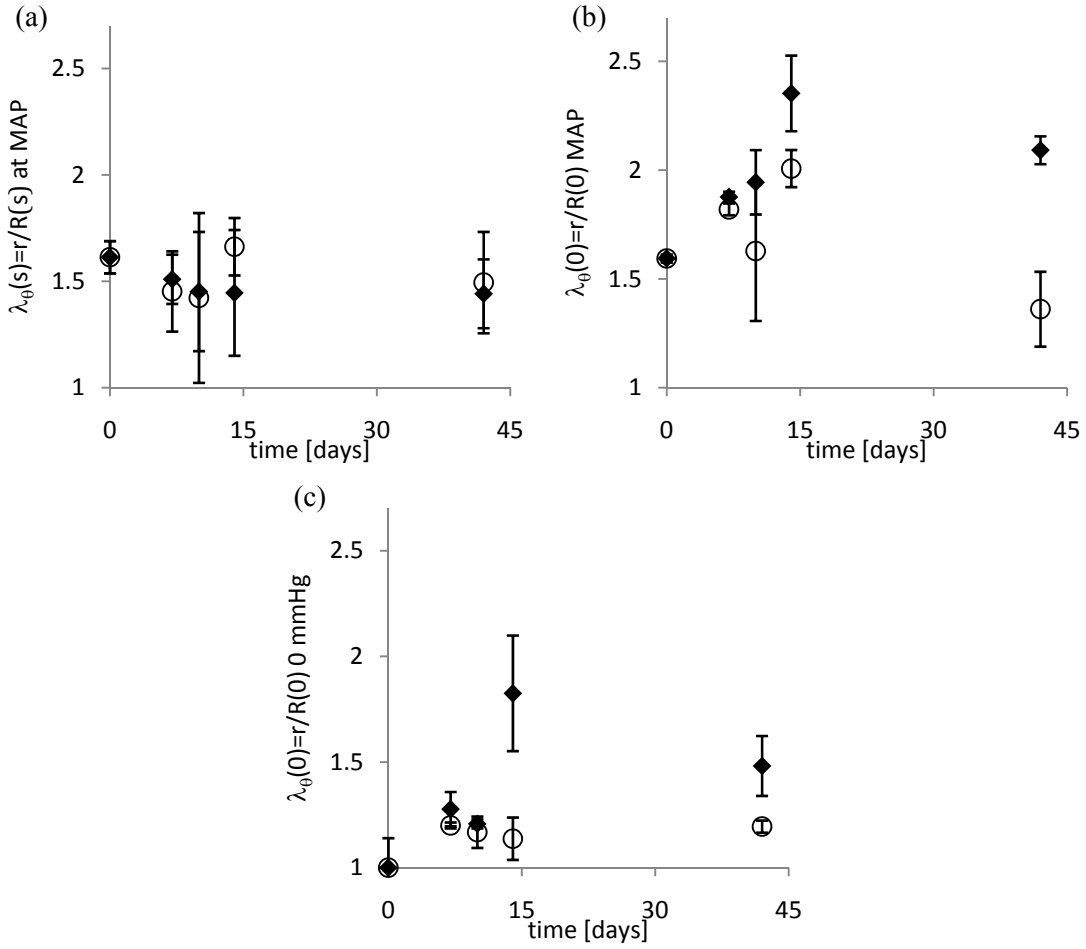

Figure 4.5. Circumferential stretch $\lambda_\theta(s)$ with different reference configurations for the RCCA-B (◆) and LCCA-B (○) as time (s) progresses after aortic banding surgery. Figure 4.5a) shows circumferential stretch $\lambda_\theta^{MAP}(s)$ at MAP with the unloaded current configuration as a reference. Figure 4.5b) shows circumferential stretch at MAP with the original $\lambda_\theta^{MAP}(s=0)$ unloaded state as the reference. Figure 4.5c) shows the unloaded current configuration referred to the original $\lambda_{\theta,u}(s=0)$ unloaded state. Bars represent ± standard deviation.

Wall stress was shown to be much lower in the RCCA-B and LCCA-B than the baseline carotid artery at all times [27] (cf. Chapter III). We hypothesized that potentially, non-tensile bearing constituents could have contributed to the substantial increase in wall thickness (Figure 4.6b) in the RCCA-B, which by equations 4.4-4.5 would result in lower than expected wall stress

(Figure 4.6c). The factor by which measured wall thickness was greater than values that would restore homeostatic values can be seen in Figure 4.6a. This excessive wall thickness peaked at 14 days to 1.8x the wall thickness needed to restore equilibrium at MAP.

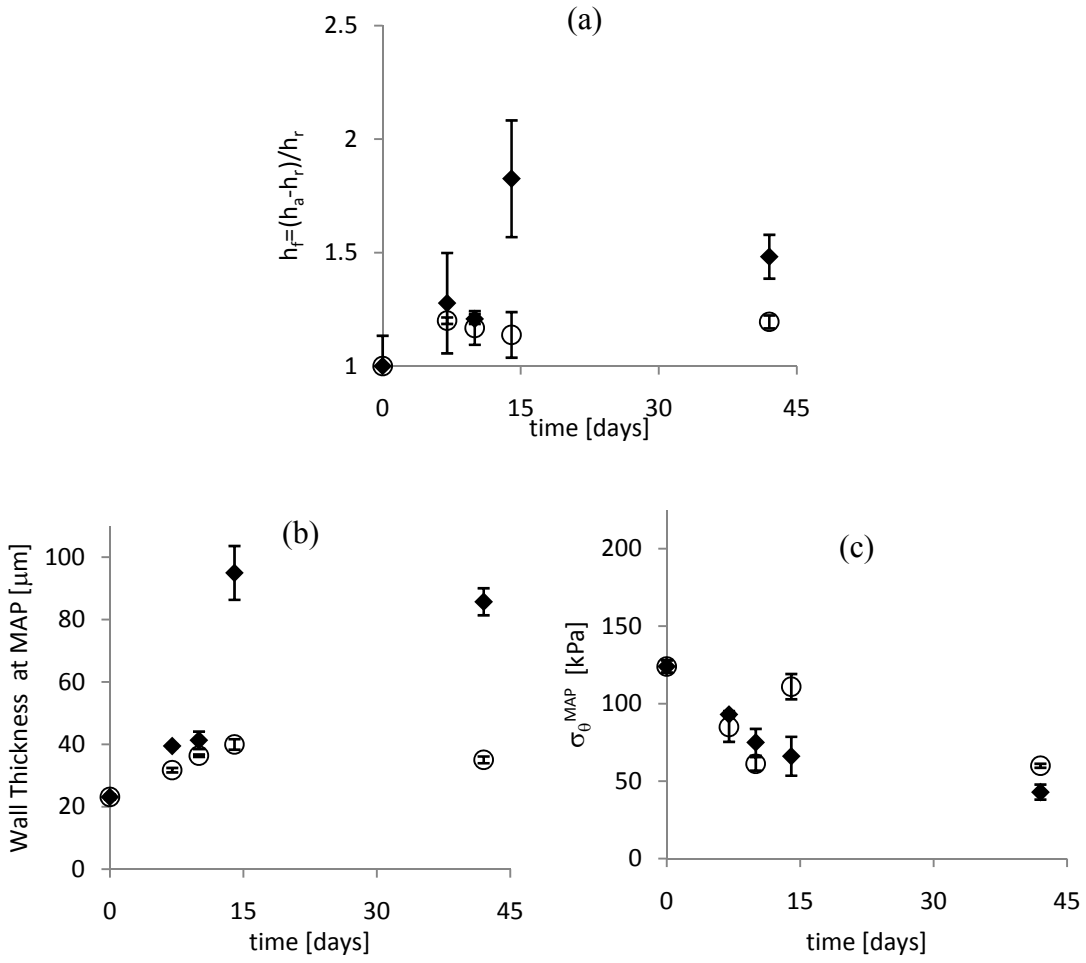

Figure 4.6. a) The factor by which the arterial wall thickness (h_f) of both RCCA-B (◆) and LCCA-B (○) is greater than values that would restore it to circumferential stresses found at the baseline carotid artery. b) Wall thickness and c) circumferential stress from Chapter III are repeated here for reference purposes. Bars represent ± standard deviation of the mean.

Discussion

The structurally motivated 4-fiber family constitutive relation employed herein has been shown previously to capture salient features of the mechanical behavior of arteries. Eberth *et al.*

[30] (cf. Chapter V) showed that the parameter *c*, associated with the elastin-dominated matrix, was less for fibrillin-1 deficient mice than for wild-type controls as expected. Furthermore, the parameters associated with axially oriented collagen were also higher for the fibrillin-1 arteries, consistent with the observed marked increase in their overall axial stiffness. Comparing results from Eberth *et al.* [30] (cf. Chapter V) for mouse carotid arteries (extracranial) with those from Wicker *et al.* [84] for rabbit basilar arteries (intracranial) reveals a markedly lower value for the latter, consistent with the much lower percentage of elastin in intracranial arteries. Results herein, based on the fit of the same 4-fiber family relation to data from hypertensive (RCCA-B) and nearly normotensive (LCCA-B) carotid arteries, revealed that hypertension caused a progressive stiffening of the RCCA-B arteries (Figure 4.1) despite a gradual loss in the isotropic contribution (Figure 4.3). That there was much more variation in strain energy, at a given state of biaxial stretch, at 7 to 10 days post-banding suggested that the significant growth and remodeling occurred at slightly different rates in the different animals. This important observation emphasizes the existence of specimen-to-specimen variability even within a genetically similar breeding colony, which also highlights the utility of studying paired arteries that are subjected to different hemodynamics within the same animal. When assessed near individual *in vivo* conditions, that is, mean arterial pressures and the *in vivo* axial stretch (λ_θ^{MAP} , λ_z^{iv}), the strain energy *W* was slightly higher in the normotensive (LCCA-B) than the hypertensive (RCCA-B) arteries at all time points due, in part, to the higher level of operating stretches. The overcompensation may be due to an attempt to try to normalize strain energy at systole in the RCCA-B.

The eventual decrease in the angle $\alpha_o^{3,4}$ in the RCCA-B arteries at 42 days (Table 4.1), that is, an increase in axially oriented collagen fibers, agreed well with both the increased anisotropy (cf. Figures 4.1 and 4.2), the empirical observation of increased axial stiffness, and

that much of the remodeling due to increased pulse pressure was adventitial [26] (cf. Chapter II). Adventitial collagen tends to have an axial orientation [84] and yet is thought to prevent over-extension of the media [3]. The changes in $\alpha_o^{3,4}$ during the first 14 days in the RCCA-B arteries were unexpected, however. The initial increase, then fall, in circumferential collagen may have reflected an early increase in medial (circumferential) collagen that gave way to an increase of adventitial collagen. Indeed, the period 7 to 10 days appeared to reflect a "transition phase" including more rapid turnover and thus changes in the amount of collagen and its orientation or undulation [87]. Finally, the decrease in the isotropic contribution to overall strain energy could reflect a strain-induced fragmentation of elastin due to increased pulse pressures in the RCCA-B arteries [37,79,80] and increase in collagen mass fraction [27].

Observation of the three-dimensional strain energy plots around their operating points suggested that the apparent increases in strain energy were not experienced in-vivo (Figure 4.4) and that the true consequence may be in further perturbations from equilibrium. In fact, the LCCA-B had higher strain energy than the RCCA-B, perhaps due to the slightly higher circumferential stretches at MAP and significantly higher in-vivo stretches. Eberth *et al.* [27] (cf. Chapter III) showed that the in-vivo axial stretches reduced from 1.72 to 1.27 in 42 days post-banding, reaching a minimum of 1.18 at 14 days, in the RCCA-B in hypertension. There is clearly a need for more attention to be paid to the microstructural basis for changes in the axial stretch, and likewise a need to quantify better whether all constituents that contribute to wall thickness are truly load bearing. We suggested, for example, that the extreme thickening of the wall may be a result of increased proteoglycan content or non-load bearing collagen. If correct, this would result in a consistent underestimation of wall stress (equations 4.4&4.5) and necessarily lead to lower stresses predicted by the model (equation 4.10). Amongst other factors,

there is a need to determine if cross-link density evolves during early stages of arterial remodeling in hypertension.

CHAPTER V

MECHANICS OF CAROTID ARTERIES IN A MOUSE MODEL OF MARFAN SYNDROME

Overview

Transgenic mouse models of Marfan Syndrome (MFS) provide insight into the type and extent of vascular abnormalities manifested in this disease. Inclusion of the mgR mutation causes the otherwise normal extracellular matrix protein fibrillin-1 to be under-expressed at ~25% of its normal value, a condition seen in MFS. Aortas in patients with MFS are generally less distensible and may experience dissecting aneurysms that lead to premature death. In this study, mouse carotid arteries heterozygous (mgR HET) and homozygous (mgR KO) for the mgR mutation were studied under biaxial loading and compared to wild-type controls (mgR WT). Carotids from WT and HET mice exhibited similar mechanical characteristics whereas those from KO mice were only slightly stiffer in the circumferential direction. The most significant difference in the KO arteries was primarily in the axial direction where axial stiffness was greater and the *in vivo* axial prestretch was less than in WT and HET counterparts. Stress-stretch data were fit by a four-fiber family constitutive model for each mouse genotype using the simplex method of parameter estimation where a lower value of a parameter typically ascribed to the elastin-dominated amorphous matrix. In conclusion, it appears that changes in axial mechanical properties may afford vessels a means to compensate, in part, for the loss of important structural constituents as they attempt to maintain mechanical homeostasis.

Introduction

Marfan syndrome (MFS), affecting approximately one out of every 5,000 people [88], is characterized by abnormal bone growth, lens dislocation, and aortic dilation and dissection. This

disease results from a variety of mutations in the gene coding for the elastin-associated extracellular matrix protein fibrillin-1 (Fbn-1) and spans a wide range of phenotypes [89]. Sherratt *et al.* [90] suggest that fibrillin microfibrils act as stiff reinforcing filaments in elastic tissues, possibly limiting extension of elastin, [91] that protect elastic fibers from a fatigue-like damage; Fbn-1 is thus important to tissue homeostasis [32,33]. In addition, recent studies [92,93] show that these microfibrils are biologically active and play a role in regulating transforming growth factor – β (TGF-β), a key modulator of extracellular matrix integrity.

Mice homozygous for the mgR mutation produce normal Fbn-1 at levels one-fourth of normal [94] and develop Marfan-like vascular abnormalities. These mice are born with apparently normal vascular elastic lamina, but develop obvious focal calcifications as early as 6 weeks [94]. Further study showed breakdown of elastic lamina within the media as well as an increased synthetic phenotype among the smooth muscle cells (SMCs), infiltration of inflammatory cells, and increased matrix metalloproteinase (MMP) levels [95,96].

Due to the devastating effects of aortic dilation and dissection, the aorta has been studied extensively in MFS. Ultrasound measurements by Jeremy *et al.* [32] suggest that ascending aortas in MFS are substantially stiffer than those of age-matched controls. Similar results were found by Marque *et al.* [97] in homozygous mgR mice. Using magnetic resonance imaging, Groenink *et al.* [98] measured decreased distensibility both in the aortic arch and near the aortic bifurcation, as well as increased pulse wave velocities along the aorta, indicating that the entire vessel stiffens in MFS.

As Marfan patients live longer due to improved treatment, they will likely face many other vascular complications that affect the normal population, such as hypertension and atherosclerosis. It is imperative, therefore, to gather biomechanical data from the entire Marfan vasculature so that clinicians can predict the effects of vascular complications in Marfan patients

and develop appropriate methods of treatment. Although the aortas in both human patients and animal models of MFS are stiffer than controls [32,97,99], there has been little research on other arteries. This chapter compares the mechanical response of common carotid arteries from wild-type animals and mice heterozygous or homozygous for the mgR mutation, a commonly used mouse model of MFS.

Materials and Methods

Animals and Surgery. A breeding pair of mice heterozygous for mgR, obtained from Dr. Francesco Ramirez, were used to produce mgR wild-type +/+ (WT), mgR heterozygous +/- (HET), and mgR homozygous -/- (KO) mice for study. Animals were cared for by the Texas A&M University Laboratory Animals Resources and Research (LARR) program. Common carotid arteries were harvested from male mice between the ages of 8 and 14 weeks. Surgical procedures, housing, and experimental protocols were approved by the University Laboratory Animal Care Committee (ULACC).

Mice were restrained by holding the tail with one hand and firmly grabbing the skin behind the neck (scruffing) with the index finger and thumb of the other hand. An intraperitoneal injection of sodium pentobarbital (125 mg/kg) was used as anesthesia and when the mouse was deeply under, an incision was made from the chest to the neck to expose the thoracic cavity and neck around the esophagus. Both carotid arteries were excised via incisions at the aortic arch and carotid bifurcation. Vessels were separated and cleaned of excess perivascular tissue. Carotids were placed in warm media, cannulated on 300 μm diameter custom-pulled glass pipettes, and secured using braided 6-0 silk suture.

Mechanical Testing. Cannulated vessels were mounted in a circulating adventitial bath contained within an isolated, temperature controlled chamber. The bath consisted of Dulbecco's Modified Eagle's Media, containing 2% heat inactivated fetal bovine serum, 2% L-glutamine,

1000 units/L penicillin, and 1000 g/L streptomycin. A steady flow of 95% air – 5% CO_2 controlled media pH. A peristaltic pump separately provided adventitial and luminal flow of media, with lumen pressure controlled independently by regulating the air-CO_2 pressure on the surface of a media reservoir. A side-mounted, calibrated CCD camera measured vessel diameter D, while precision stepper motors controlled the vessel's length. A force transducer was connected to the distal cannula and measured the applied axial force, f_T. Further detail on the biaxial testing device can be found in Gleason *et al.* [61].

Unloaded dimensions were measured interactively by identifying the length at which the vessel began to bend at zero pressure. Circumferential and axial stretches were calculated based on these dimensions. The vessel was stretched to its predetermined *in vivo* value λ_z^{iv} (see below) and preconditioned through three cycles of pressurization from 0 to 140 mmHg to minimize hysteresis. The computer then performed a pre-programmed routine to achieve various axial stretch and pressure set-points. Wall volume remains nearly constant over short periods (i.e., without growth and remodeling), thus inner radius r_i and wall thickness h were calculated from incompressibility via [3,61,100]

$$r_i = \sqrt{r_a^2 - \overline{V}/(\pi \ell)}\,, \qquad h = r_a - r_i \tag{5.1, 5.2}$$

where $\overline{V}$ is the mean wall volume, ℓ the current length, and r_a the outer radius. Wall volume was estimated based on 12-15 measurements of inner and outer radius at multiple static pressures and lengths. Equation 5.1 thus allowed inner radius to be determined at any pressure and stretch based on known $\overline{V}$ and ℓ and on-line measurements of outer radius via an edge detection algorithm in LabView.

Mechanical testing consisted of cycling pressures from 0 to 140 mmHg (KO) or 160 mmHg (WT and HET) twice at each of three fixed axial stretches $\lambda_z^{WT/HT}$ =1.65, 1.75, 1.85 and

λ_z^{KO} =1.55, 1.65, 1.70. Next, the program tested the load-length response at each of three fixed pressures (P =60, 100, 140 or 160 mmHg) while the axial load was varied twice from 0 to 8.8 mN (0.9 g). The mechanical results at a fixed pressure of 140 mmHg were interpolated for WT and HET using a three-point interpolation from the 60, 100 and 160 mmHg tests. Based on pilot results, the KO set-points for stretch and peak pressures were set lower than the WT and HET to protect cells from possible damage due to overstretching. As a result, group-to-group comparisons were based on interpolations across a range of axial stretches with the only common stretch set-point at λ_z =1.65. The summary of mechanical testing performed on the different mouse types and their age/weight are reported in Table 5.1.

Following mechanical testing, we evaluated both endothelial and smooth muscle functionality. Phenylephrine (10^{-5} M) was added to the adventitial bath and the diameter was allowed to equilibrate for 15 (WT and HET) or 30 (KO) minutes to determine smooth muscle contractility. The knockout vessels were generally less responsive to phenylephrine, possibly due to alterations in cell phenotype as described in Bunton *et al.* [95]. For WT and HET groups, 30 percent contraction was considered functional. Next carbamycholine chloride (10^{-5} M) was added to test for endothelial-dependent smooth muscle relaxation and the vessel was allowed to equilibrate for 15 minutes. A 10% relaxation was considered functional for all groups. Sodium nitroprusside (10^{-4} M), which tests endothelial-independent relaxation, was then added to the bath and the vessel allowed to equilibrate for 15 minutes. Finally, the media was replaced with Hank's Balanced Salt Solution (HBSS) without calcium and magnesium but containing sodium nitroprusside (10^{-5} M) and EGTA ($2x10^{-3}$ M) to ensure full smooth muscle relaxation. Mechanical testing described above was repeated for the passive state.

Table 5.1. Summary of tests on mgR WT, HET, and KO mice with (*n*) given separately for basal, passive data.

		Genotype (mgR)	Group Size (n)	Avg. Weight (g)	Mean Age (wks)
Fixed	Press.	WT (+/+)	8, 7	23.83	11.5
		HET (+/-)	8, 6	23.57	11.1
		KO (-/-)	7, 9	20.60	9.5
Fixed	Stretch	WT (+/+)	7, 7	23.25	12.1
		HET (+/-)	6, 6	24.24	12.0
		KO (-/-)	7, 9	20.59	9.7

Formula for stress calculations are described in Chapter V. The basal or passive (b, p) (circumferential $\lambda_\theta^{b|p}$, axial $\lambda_z^{b|p}$, and radial $\lambda_r^{b|p}$ stretches were calculated from unloaded basal and loaded basal and passive states via

$$\lambda_\theta = \frac{r_{mid}^{b|p}}{\rho_{mid}},\ \lambda_z = \frac{\ell^{b|p}}{L},\qquad \lambda_r = \frac{1}{\lambda_\theta \lambda_z} \tag{5.3-5.5}$$

where ρ and L are radii and axial length in the unloaded basal configuration, respectively.

Note that the unloaded basal configuration can be mapped mathematically into either a loaded basal or a loaded passive configuration through the deformation gradients $\mathbf{F}^b$ and $\mathbf{F}^p$ (Figure 5.1). We referred the passive loaded configuration to the basal unloaded configuration instead of the passive unloaded configuration simply to facilitate comparisons of data. Of course, a stress free configuration (R, Θ, Z) could also be used as a reference, but this is only needed for 3-D stress analyses and would require a stress relieving radial cut that causes the vessel to spring open [101]. Such a "stress-free" state still has residual stresses, due to elastin in tension [4,10] and collagen in compression, which could in turn be reduced using elastase or collagenase.

Because residual stresses tend to yield homogeneous transmural distributions of stress, which thus render mean values (equations 5.4, 5.54) as good estimates of wall stress, and because we did not attempt to quantify smooth muscle phenotype as a function of radius across the wall, the unloaded basal state was used as a reference herein.

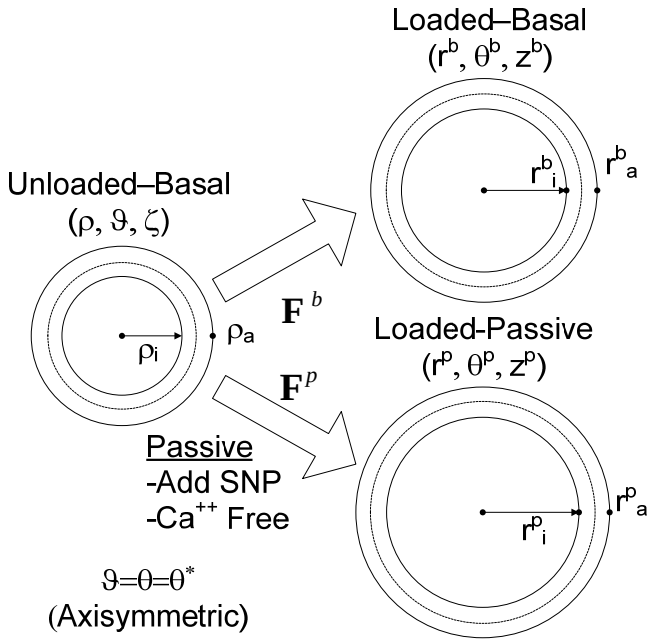

Figure 5.1. Unloaded and loaded basal configurations and loaded passive configurations. For convenience, all loaded configurations were referred back to the unloaded basal configuration to quantify deformations during biaxial testing.

The four-fiber family constitutive relation is described in Chapter IV by equations 4.9-4.12. Unknown material parameters were fit using the simplex method (equation 5.13). One difference between the modeling method used for Chapter IV and Chapter V is that in some cases contained in this chapter (only where noted) we used nonlinear optical microscopy to estimate fiber angle.

Results

Pressure and Force. Intersections of axial force-stretch curves at different fixed pressures estimate the *in vivo* axial stretch [3,102-106] . This stretch may help to optimize the vessel against buckling during normal movement and is a crucial measure used to compare vessels *in vitro* [105]. Averaged, basal, *in vivo* axial stretches for WT, HET, and KO mice were λ_z^{iv}=1.71, 1.72 and 1.63, respectively (Figure. 5.2, a-c, a), and passive axial stretches were similarly $\lambda_z^{p,iv}$=1.72, 1.73 and 1.64 (i.e., there was no statistical difference between basal and passive values). Note, however, that the *in vivo* axial stretch for KO was significantly less than that for both WT and HET. Basal values of the associated *in vivo* force for WT, HET, and KO mice were f_T=3.63, 3.34 and 2.85 (mN), respectively (Figure 5.2, a-c and, and mean, passive axial forces were f_T^p=3.43, 3.67 and 2.40 (mN). Again, the *in vivo* value for the KO was statistically different from WT and HET, which were not statistically different from one another.

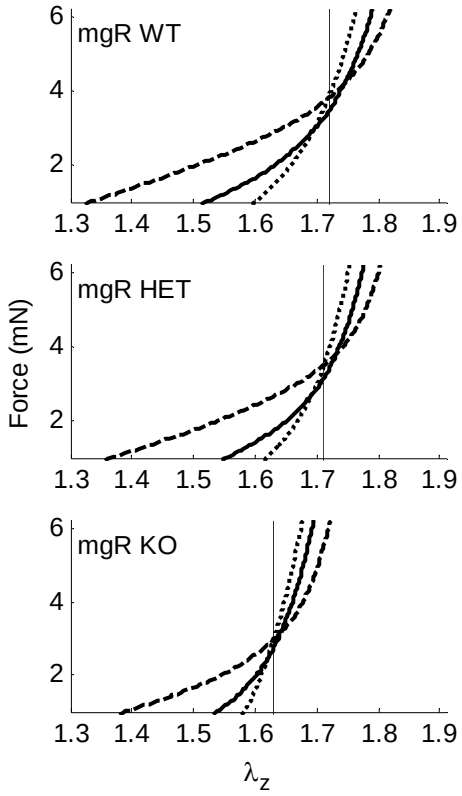

Figure 5.2. Averaged axial force-stretch data with basal smooth muscle tone at fixed pressures of 60, 100, and 140 for carotid arteries of wild-type (WT), heterozygous (HET), and knockout (KO) mice. Note that cross over points/intersections estimate the *in vivo* axial stretch (vertical lines).

Averaged axial force-pressure data (Figure 5.3, a-c) show that the *in vivo* estimation for the WT and HET carotids yielded a relatively flat relation at λ_z^{iv} as expected [104]. These data indicate that WT and HET mice can be considered mechanically similar in the axial direction (Figure 5.3 a,b). That the magnitude of the *in vivo* axial force was lower for the KO (2.4 mN) compared to both WT and HET vessels (~3.5 mN) is also seen easily in Figure 5.3. Axial force, however, was not significantly influenced by smooth muscle contractility because the cells are oriented primarily in the circumferential direction.

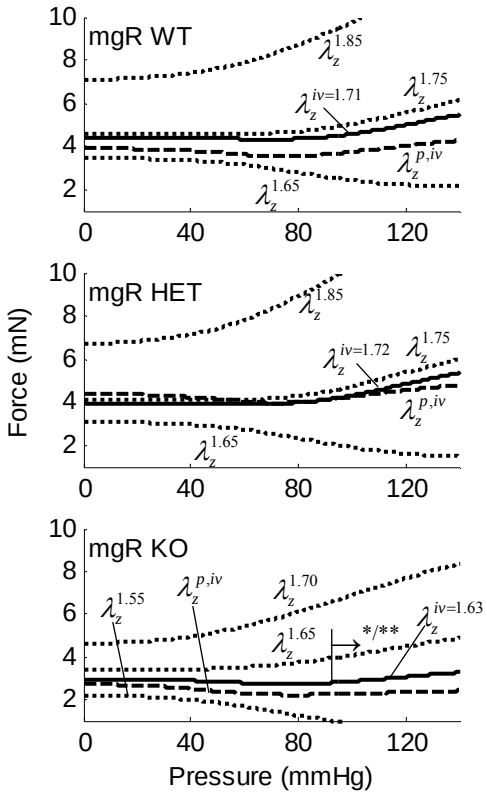

Figure 5.3. Averaged axial force-pressure experimental data at fixed axial stretches including basal and passive conditions. Also shown are interpolated data at the *in vivo* axial stretch for the carotid arteries of wild-type (WT), heterozygous (HET), and knockout (KO) mice. The → indicates the direction of statistical difference for the KO relative to WT at (*) $\lambda_z^{1.65}$ and (**) λ_z^{iv}.

Pressure and Diameter. Cyclic testing at a common axial stretch of 1.65 allowed direct numerical comparison amongst all three genotypes. Further testing was performed at stretches above and below the *in vivo* (λ_z^{iv}) stretch, with the experimental behavior interpolated at λ_z^{iv} (not known a priori). All fixed pressure and axial stretch testing was performed with basal and then passive smooth muscle tone. Figure 5.4 shows characteristic changes in diameter as the pressure increased. The KO vessel appeared to be slightly dilated; statistical analysis only revealed differences, however, between the WT/HET and KO groups for pressures over 40 mmHg in the passive state. For example, the slope of the pressure-diameter data for the passive KO vessel in

this pressure range was steeper than that for the passive WT and HET groups, thus indicating a circumferentially stiffer structure.

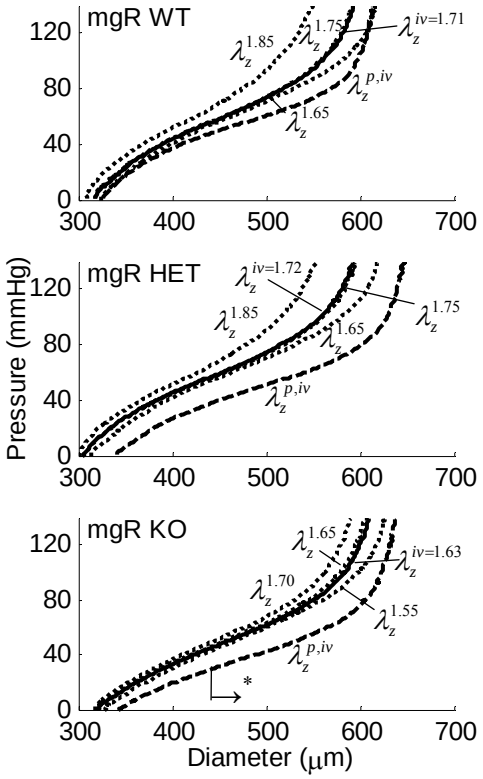

Figure 5.4. Averaged pressure-diameter experimental results at fixed axial stretches including basal and passive conditions, with those at the *in vivo* axial stretch interpolated from the other stretch-data for the carotid arteries of wild-type (WT), heterozygous (HET), and knockout (KO) mice. The → indicates the direction of statistical significance for the KO from the WT mouse at (*) λ_z^{iv} in the passive state.

Stress. Altered states of stress may be initiators or indicators of disease. Although differences between groups did not reach statistical significance for the circumferential direction, the stress-stretch curves for the HET carotids were shifted slightly to the right (less stiff) compared to those for the WT. This may have been due to an altered compensatory mechanism not available in the KO carotids. As expected, smooth muscle relaxation resulted in vessel

dilatation at any given pressure causing distinct shifts in pressure - diameter (Figure 5.4, a-c) and σ_θ - λ_θ plots (Figure 5.5, a-c) relative to basal responses.

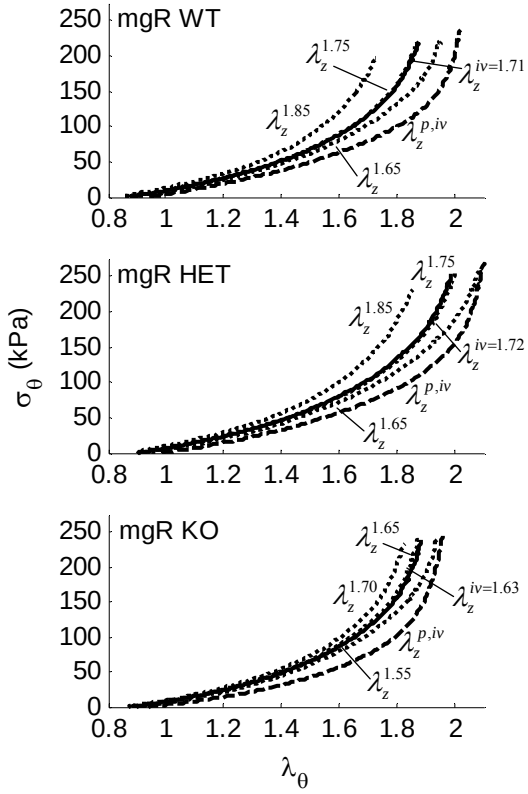

Figure 5.5. Averaged circumferential stress-stretch experimental results at fixed axial stretches including basal and passive conditions, plus interpolated results for the *in vivo* axial stretch for the carotid arteries of wild-type (WT), heterozygous (HET), and knockout (KO) mice. Data interpolated at the *in vivo* axial stretch is indicated by λ_z^{iv} with the value of *in vivo* axial stretch superscripted.

Carotids from WT and HET mice exhibited similar axial stress responses (Figure 5.6, a-c). Figure 5.6, a,b shows the axial stress as a WT and HET were stretched axially at fixed pressures of 60, 100, and 140 mmHg. Figure 5.6c shows the axial stress for KO vessels at 60 and 100, and 140 mmHg indicating that the KO vessel experienced greater values of axial stress for similar axial stretches.

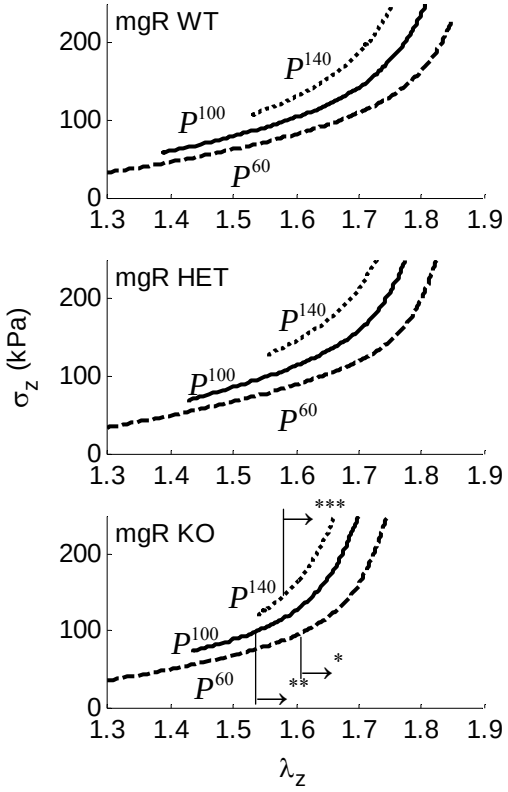

Figure 5.6. Averaged axial stress-stretch results for basal smooth muscle tone at fixed pressures of 60, 100 and 140 mmHg for the carotid arteries of wild-type (WT), heterozygous (HET), and knockout (KO) mice. The → indicates the direction of statistical difference for the KO from the WT mouse at (*) P=60, (**) P=100, or (***) P=140 mmHg. The value of fixed pressure is shown in the superscript.

A representative dose response curve for one vessel with all of the vasoreactants is shown in Figure 5.7. Phenylephrine (10^{-5} M) was added to the adventitial bath at point (a) to test for smooth muscle contractility and point (b) represents the vessel in its "maximum" contractile state. Carbamycholine chloride (10^{-5} M) was added at point (b) to test for endothelial-dependent smooth muscle relaxation. As nitric oxide (NO) was depleted, the diameter returned to its contractile status: points (c)-(d). Sodium nitroprusside (10^{-4} M) was then added to the bath to

elicit endothelial-independent smooth muscle relaxation at point (d). The media was replaced with Hank's Balanced Salt Solution (HBSS) without calcium or magnesium but containing sodium nitroprusside (10^{-5} M) and EGTA ($2x10^{-3}$ M) to ensure full smooth muscle relaxation by depleting intracellular and extracellular stores of calcium at point (e). The gap in diameter data between points (e) and (f) occurred during the exchanging of media for HBSS.

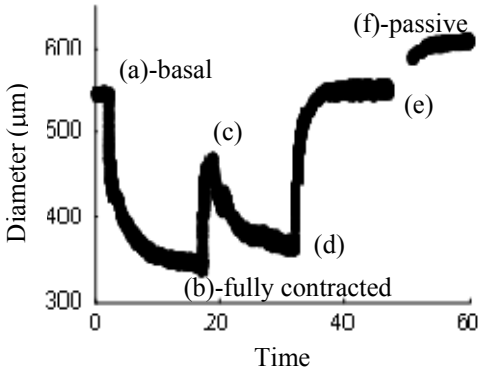

Figure 5.7. Representative diameter dose-response for the addition of (a) phenylephrine at 10^{-5} M, (b) carbamycholine chloride at 10^{-5} M, (d) sodium nitroprusside at 10^{-4} M, and (e) Hank's Balanced Salt Solution (HBSS) containing sodium nitroprusside (10^{-5} M) and EGTA ($2x10^{-3}$ M), with maximally contracted and fully passive states at (b) and (f).

Mean values of distension for each mouse type (WT, HET and KO) at each smooth muscle cell function reference point (a)-(f) can been seen in Figure 5.8. By comparing the fully passive state (f) to the basal one (a), one observes that the "basal" state of all vessels had very little smooth muscle tone. KO vessel circumferential stretch changed less than WT and HET for all levels of smooth muscle activation.

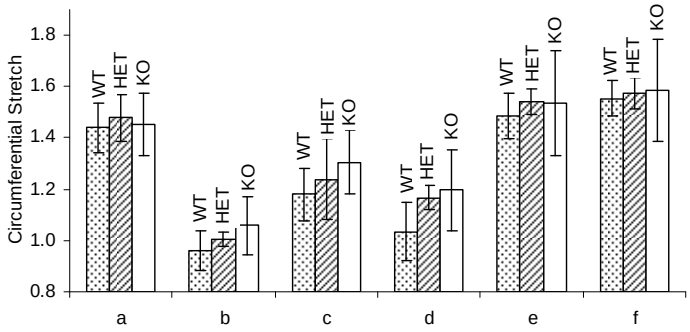

Figure 5.8. Average circumferential stretch values for the addition of (a) phenylephrine at 10^{-5} M, (b) carbamycholine chloride at 10^{-5} M, (d) sodium nitroprusside at 10^{-4} M, and (e) Hank's Balanced Salt Solution (HBSS) containing sodium nitroprusside (10^{-5} M) and EGTA ($2x10^{-3}$ M), with maximally contracted and fully passive states at (b) and (f) for wild-type (WT), heterozygous (HET) and knockout (KO) vessels

Four-Fiber Family Model. The unknown parameters in the four-fiber family strain energy function (Equations 5.9-5.12) were determined via minimization of the objective (error) function described by equation (5.13) for each vessel in the passive state. Fiber families 1 and 2 are considered to be primarily axial with $\alpha_o^1 = 0$ deg and circumferential with $\alpha_o^2 = 90$ deg. Furthermore, for the diagonal families $\alpha_o^4 = -\alpha_o^3$ was represented by one angle α_o. Results of the parameter estimation for the WT, HET and KO can be seen in the table at the end of the chapter. Illustrative fitted results with experimental data for one mouse in each data set are shown in Figure 5.9. Of particular note is the reduction of the isotropic Fung parameter "c" in the KO mice and the similar values of coefficients in the WT and HET mice. One noticeable difference between the WT and HET is the reduction in fiber angle for the HET.

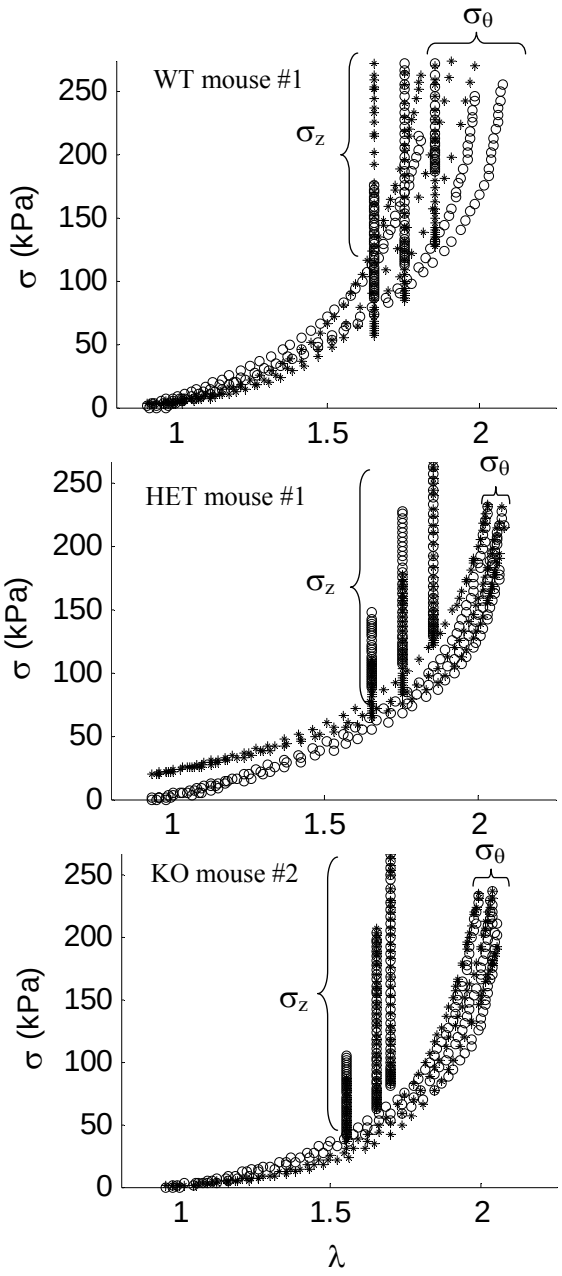

Figure 5.9. Constitutive fits (∗) for experimental data (∘) at three axial stretches for a) wild-type (WT) mouse #1 in with $c = 2.081$ kPa, $c_1^1 = 7.558$ kPa, $c_2^1 = 0.091$, $c_1^2 = 10.846$ kPa, $c_2^2 = 0.012$ $c_1^3 = 0.662$ kPa, $c_2^3 = 0.909$, $\alpha_o = 27.58$ deg., b) heterozygous (HET) mouse #1 with $c = 20.656$ kPa, $c_1^1 = 0.185$ kPa, $c_1^2 = 0.532$, $c_1^2 = 0.051$ kPa, $c_2^2 = 0.429$, $c_1^3 = 0.576$ kPa, $c_2^3 = 0.477$ and $\alpha_o = 32.00$ deg., and c) knockout (KO) mouse #2 with $c = 0.234$ kPa, $c_1^1 = 7.086$ kPa, $c_2^1 = 0.178$, $c_1^2 = 4.978$ kPa, $c_2^2 = 0.082$, $c_1^3 = 0.265$ kPa, $c_2^3 = 0.937$ and $\alpha_o = 30.86$ deg. Axial stretch remained constant throughout the above fitted testing procedure while axial stress can change due to changes in pressure (cf. equation 4.5) causing the axial stress to be represented by vertical lines.

Discussion

We characterized, for the first time, the biaxial mechanical behaviors of common carotid arteries in homozygous (knockout, KO) and heterozygous (HET) mouse models of reduced, extracellular matrix protein Fibrillin-1 (Fbn-1) and compared the results to otherwise normal wild-type (WT) mice. Our results revealed that carotids from 9.5 week old mice homozygous for the mgR mutation, which reduces fibrillin-1 content ~25%, exhibited altered mechanical properties while those from heterozygous mice were similar to their wild-type controls. Differences were primarily in the axial direction where the *in vivo* axial stretch was lower and axial stresses were higher in KO than HET and WT for a common value of axial stretch. When vessels were normalized to their individual *in vivo* stretches, however, both axial force and axial stress were lower in KO vessels than in HET and WT, perhaps suggesting a slight overcompensation. KO vessels showed only slight increases in circumferential stiffness and diameter in the passive state without the degree of dilation found in studies of the aorta.

The parameter estimation and fitting of data (Figure 5.9) demonstrated the utility of a four-fiber family constitutive model to describe mean stresses at three axial stretches for WT, HET, and KO carotids. Minimal hysteresis was exhibited during loading and unloading cycles at 0.01 Hz (data not shown), further justifying the use of an elastic model. We found, however, that the model had difficulty predicting stress when prescribed axial stretches yielded wide variations in σ_θ - λ_θ. Whereas minimization of the objective function e (equation 5.13) was based directly on stress, other mechanical quantities can be calculated using the constitutive model and best-fit parameters. For example, Figure 5.10 shows predicted versus measured results for pressure-distension for WT mouse #3 and force-pressure for KO mouse #7. Although reasonable, these predictions reflected varying degrees of goodness since they are secondary calculations with additional free variables.

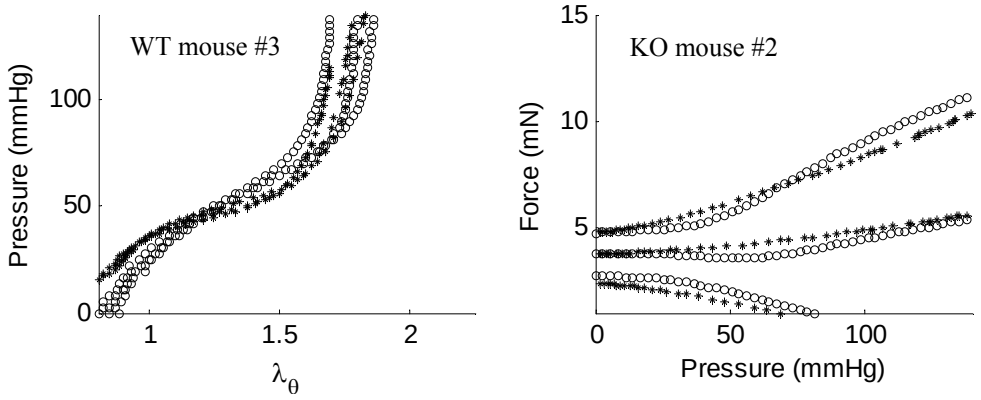

Figure 5.10. Estimated ($*$) and experimental ($\circ$) a) diameter vs. pressure for passive wild-type (WT) mouse #3 with $c = 24.292$ kPa, , $c_1^1 = 0.469$ kPa, $c_2^1 = 0.493$, $c_1^2 = 1.873$ kPa, $c_2^2 = 0.278$ $c_1^3 = 0.021$kPa, $c_2^3 = 1.425$, $\alpha_o = 39.98$ deg., or b) force vs. pressure for passive knockout (KO) mouse #2 with $c = 0.234$ kPa, $c_1^1 = 7.086$ kPa, $c_2^1 = 0.178$, $c_1^2 = 4.978$ kPa, $c_2^2 = 0.082$, $c_1^3 = 0.265$ kPa, $c_2^3 = 0.937$ and $\alpha = 30.86$ deg.

In the parameter estimations, the angle α_o for the families of diagonal fibers was left free to vary within the model to help minimize the objective function. Such fiber angles may change with vessel remodeling and disease and can be measured directly, however. One way to compare such modeling results to actual fiber angles is to use nonlinear optical microscopy (NLOM) [84] to visualize intramural collagen (via 2nd harmonic generation) throughout the wall (Figure 5.11). Fiber direction was quantified using NLOM and a mean fiber angle $\alpha^{\exp}$ (in the current configuration) was determined at each 0.5 μm increment. Taking geometry and deformation into consideration, mean fiber angles in the reference configuration were calculated using

$$\alpha_o^{\exp} = \tan^{-1}\left(\frac{\lambda_z}{\lambda_\theta}\tan\alpha^{\exp}\right), \tag{5.6}$$

where $\alpha_o^{\exp}$ is the fiber angle in the unloaded state similar to estimated values. For one additional specimen for each genotype, mean fiber angles in the unloaded state were found via NLOM to

be $\alpha_{o,WT}^{\exp}$ =43.2 deg, $\alpha_{o,HET}^{\exp}$ =20.2 deg, and $\alpha_{o,KO}^{\exp}$ =51.1 deg for three fixed axial extensions and a pressure of 100 mmHg. These values were prescribed in the 4-fiber family constitutive model for that data set having the closest fiber angle found through parameter estimation, and best-fit parameters were determined again. The resulting error was slightly higher when fiber angle was fixed for WT test #2a, HET test #5a and KO test #6a, but otherwise similar thus suggesting the utility of prescribing the mean angle based directly on data when available.

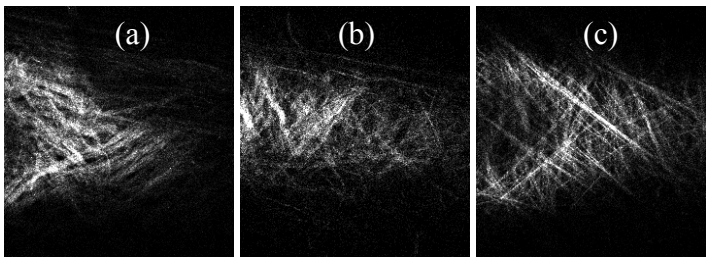

Figure 5.11. Nonlinear optical microscopic image of a representative vessel with fibrillar collagen illuminated using 2nd harmonic generation. a) wild-type, b) heterozygous (HET), and c) knockout (KO) vessels. Due to out-of-plane imaging, the left side of the HET and KO images show part of the lumen.

Fibrillin-1 is one of many micro-fibrils involved in supporting elastin [107-109] , but its precise role in the vasculature remains unknown. These micro-fibrils may help transfer load to and orient the elastic fibers along the direction of stress [110] . Others suggest that Fbn-1 may act as a protective sheath that prevents elastin from over-extending [90,91]. Fbn-1 is also known to down-regulate TGF-β [92,93], a growth factor frequently found with higher expression at sites of aortic aneurysms. Chung *et al.* [111] studied the thoracic aorta in Fbn-1 deficient mice with and without aneurysm and found further that MMP production was upregulated in those with aneurysms. They suggest that Fbn-1 fragments may stimulate MMP production, thus causing a vicious cycle that leads to aneurysm. Smooth muscle cells are both the sensor and effector of

remodeling and are improperly linked to the extracellular matrix in models of MFS [112]. Cellular remodeling of matrix (e.g., via production, removal, and reorientation of collagen) may thus be compromised in MFS. Our data showed that smooth muscle contractility was affected only slightly by partial removal of extracellular matrix protein Fbn-1 (Figure 5.8), possibly due to an increased synthetic phenotype as noted by Bunton [95].

It is possible that changes in the *in vivo* axial stretch implicate a compensatory mechanism available during development (cf. Figure 5.12). Some suggest however, that Fbn-1 has a maintenance role for existing elastic fibers rather than being involved in early assembly [94]. Fbn-1 deficient mice are similar to wild-type mice at birth, but gradually develop defects. Marque *et al.* [97] showed that a reduction in Fbn-1 causes an accelerated, aged-related fragmentation of elastin, rather than affecting elastognesis. If there is an adaptation during development, it may compensate for the reduced Fbn-1 (e.g., by up-regulating other micro-fibrils) rather than for poorly cross-linked elastin. There is clearly a need for further study.

The biomechanical properties of Fbn-1 deficient carotid arteries resembled those of normally aged vessels wherein elastin has a reduced mass fraction [63,113], noting that associated decreases in overall arterial elasticity may render individuals at higher risk for aneurysm [114]. An analogy can thus be made to the findings of Pezet *et al.* [115] who showed that aortas from mice with heterozygous mutations in the elastin gene ELN (6 months) exhibit some characteristics similar to those of aged (24 months) wild-type mice. Specifically, decreased elastin results in reduced elasticity, vessel lengthening, extracellular matrix accumulation, and decreased endothelial derived vasomotor response in addition to systemic hypertension. Elastin is highly stable and deposited primarily during development despite continued demand from perturbations in stress. Aged vessels experience a decreased *in vivo* axial stretch [116] and often become stiffer and tortuous [4,10] resulting from vessel lengthening and extracellular matrix

accumulation. Age did not have consistent correlation with any mechanical parameters but might be significant for the KO mouse (Age SD=0.91) at ages beyond the scope of our test (10 wks for KO) as disease characteristics are known to intensify. Further, weight correlated only with diameter, force and thickness, not stress.

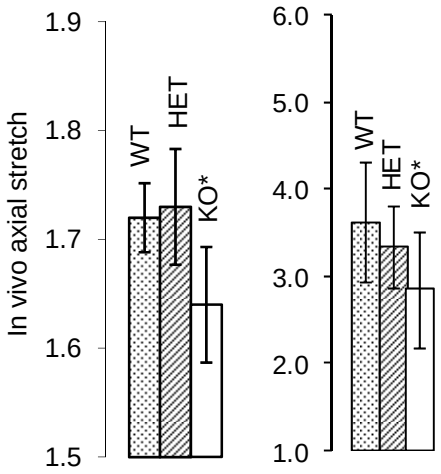

Figure 5.12. Passive *in vivo* axial stretch for carotid arteries of a) for wild-type (WT; 1.72), heterozygous (HET; 1.73), and knockout (KO; 1.64) mice and similarly for force b) wild-type (WT; 3.63 mN), heterozygous (HET; 3.34 mN), and knockout (KO; 2.85 mN) mouse types. (*) indicates that there is statistical significance between the basal and passive condition.

The literature shows that aortas from MFS patients have reduced distensibility [32,33,99] . Although both the carotid artery and the aorta are classified as elastic, Jondeau *et al.* [33] found that carotid artery diameters were not different in human MFS patients compared to normal samples at either diastole or systole. Our results similarly show that changes in basal diameter from diastole to systole in mouse carotids (Table 5.2) held at an *in vivo* axial stretch are comparable to the WT and KO. Some feel that vessel failure in MFS may result from cyclic fatigue [32,33]. Marque *et al.* [97] reported WT and KO blood pressures to be 124/91 and 131/88 respectively, at similar heart rates. Circumferential stresses across these blood pressures

range from 117 to 188 kPa for the WT mouse and 127 to 222 for the KO, demonstrating that KO vessels experience a greater increase in stress throughout the cardiac cycle. Furthermore, the ratio of circumferential stress to axial stress at *in vivo* axial stretch at diastole was greater for the KO than the WT or HET but not at systole (Table 5.2). It is not known how such ratios might play a role although Jackson *et al.* [112] showed that cells can distinguish between loadings in two different directions resulting in independent oriented remodeling.

Table 5.2. Mechanical parameters across the cardiac cycle for carotid arteries of mgR WT, HET and KO mice. †Blood pressures from Marque *et al.* [97].

	WT	KO
Blood Pressure (mmHg)†	124/91	131/88
Mean Wall Thickness (μm)	24.8	23.2
Outer Diameter (μm) Systole/Diastole	584/544	607/567
Circ. Wall Stress (kPa) Systole/Diastole	188/117	222/127
Axial Wall Stress (kPa) Systole/Diastole	220/168	197/137
Mean Circ. To Axial Wall stress Ratio	0.86/0.97	1.13/0.93

Average best-fit values for the isotropic stress parameter (c) were 8 to 9 times greater for the WT and HET mice than the KO (Table 5.3). The elastin-dominated amorphous matrix has a nearly isotropic response, thus the KO vessel probably had decreased elastin effectiveness. Mathematically, however, some of the isotropic response could be accommodated by increasing the value of the parameters of fiber families (1) and (2), which are controlled primarily by collagen accumulating and orientating to optimize stress. The reduction of *in vivo* axial stretch could be the byproduct of a decrease in axially oriented elastin fibers as a result of

fragmentation. The elastic recoil of arteries upon excision indicates an axial tension *in vivo*, but the associated unloaded state has residual stresses. Zeller and Skalak [10], showed by applying elastase and collagenase to otherwise unloaded cross sections of rat saphenous arteries and observing the change in opening angle and circumference, that elastin is in tension in the circumferential direction in unloaded segments. The same is expected for the axial direction where elastin provides a retraction force that is equilibrated by compressing other constituents in the unloaded state [116], primarily GAG-sequestered water and smooth muscle, bound by collagen fibers. If the elastin is fragmented, the retraction force could decrease and the vessel elongate. When the vessel is excised the decreased force would limit the degree of retraction and show a vessel with a decreased axial prestrech compared to healthy vessels as observed herein.

Current treatments of MFS symptoms seek primarily to prevent dilation and dissection [88,93]. Hence, β-blocker therapy and limiting exhaustive exercise are used for their negative chronotropic and inotropic effects. These therapeutic methods reduce the hemodynamic stress on the aortic wall in an attempt to avoid an initial insult that may lead to aneurysm. Most elastic arteries experience only minimal cyclic axial extensions from the rhythmic pulsations of the heart with the exceptions of the pulmonary artery and ascending aorta due to their close proximity to the heart, yet all elastic vessels experience marked cyclic changes in diameter as a result of the variations in blood pressure and flow throughout the cardiac cycle. Aortic dissection occurs frequently in the ascending aorta, which could be due to the unusual cyclic changes in length (axial stress) known to occur here. Hence, cyclic loading may be important to MFS arterial stability. β-blocker therapy and reduced exhaustive exercise may also limit the axial stresses experienced by the ascending aorta. Coincidentally, during early stages of *in vitro* testing we observed dissecting carotid aneurysms following acute overstretching in the axial direction (data not shown). Recently, TGF-β neutralizing antibodies and the angiotension II

receptor antagonist, Losartan, have demonstrated promising results for preventing aneurysms in a different mouse model for Marfan Syndrome [93] ($Fbn1^{C1039FG/+}$) by reducing TGF-β (a growth factor known to be involved in developing aneurysms in MFS). Angiotension II receptor antagonists also reduce hemodynamic stress by decreasing blood pressure, but its action as a vasodilator complicates its utility if used in adulthood.

By examining vessels *in vitro*, our findings illustrate the importance of axial extension in studying effects of MFS on arteries. *In vivo* determination using MRI, ultrasound, or catheter mounted pressure transducers to infer arterial stiffness by pulse wave velocity cannot reveal axial changes in stiffness, and thus only approximates overall macroscopic characteristics. The structural integrity of Fbn-1 deficient arteries is sensitive to perturbations in axial extension and may contribute to the fatal consequence of this disease, dissecting aneurysm. The carotid arteries of KO mice show a greater stress for comparable axial stretches. These findings could be a result of changes in the unloaded configuration, which can evolve in the diseased state. This disease model is further evidence that the mechanisms of growth and remodeling are three-dimensional and precise tracking of axial changes must eventually be identified.

Table 5.3. Best-fit parameters for a 4-fiber family model determined using the simplex method for passive carotid arteries of wild-type (WT), heterozygous (HET), and knockout (KO) mouse types for each mouse tested (n=22). Fiber angle α_o was allowed to be free in all parameter estimations except where noted (2a, 5a, and 6a).

fiber family		k=1	1	k=2	2	k=3	3		
	c [kPa]	c1 [kPa]	c2	c1 [kPa]	c2	c1 [kPa]	c2	α_o [Deg]	Error
WT									
1	2.081	7.558	0.091	10.846	0.012	0.662	0.670	27.58	0.152
2	4.105	5.101	0.159	0.000	1.690	1.322	0.448	44.16	0.262
3	24.292	0.469	0.493	1.873	0.278	0.021	1.425	39.98	0.120
4	1.348	1.792	0.316	3.021	0.001	0.503	0.322	30.20	0.130
5	13.577	0.757	0.519	9.419	0.018	1.394	0.670	34.45	0.148
6	0.034	0.000	2.942	0.014	1.827	0.091	1.838	37.56	0.463
7	12.728	0.055	1.016	3.772	0.001	0.047	0.992	34.12	0.270
avg	**8.309**	**2.248**	**0.791**	**4.135**	**0.547**	**0.577**	**0.909**	**35.44**	**0.221**
std	8.247	2.720	0.922	4.027	0.773	0.543	0.508	5.25	0.114
								α from NLOM	
2a	0.162	1.876	0.344	1.767	0.067	3.667	0.266	**43.23**	0.223
HET									
1	20.656	0.185	0.532	0.051	0.429	0.576	0.477	32.00	0.251
2	10.188	0.954	0.434	2.298	0.115	1.377	0.480	31.22	0.147
3	7.344	0.735	0.380	2.350	0.076	2.057	0.342	30.21	0.181
4	4.280	0.727	0.538	0.112	0.244	6.439	0.226	36.54	0.192
5	4.324	11.267	0.152	4.256	0.082	0.061	1.141	29.30	0.151
6	1.351	4.326	0.113	0.014	0.162	3.065	0.235	36.12	0.180
avg	**9.359**	**2.773**	**0.407**	**1.814**	**0.189**	**2.102**	**0.533**	**31.85**	**0.184**
std	6.305	3.928	0.170	1.595	0.123	2.107	0.311	2.80	0.034
								α from NLOM	
5a	8.066	0.007	0.010	5.242	0.066	1.546	0.576	**20.19**	0.249
KO									
1	0.005	0.142	0.342	1.956	0.087	1.643	0.445	21.03	0.286
2	0.234	7.086	0.178	4.978	0.082	0.265	0.937	30.86	0.157
3	1.612	8.623	0.138	4.387	0.055	0.051	1.036	32.25	0.196
4	4.325	10.812	0.116	7.516	0.298	0.670	1.291	31.96	0.156
5	0.001	2.041	0.488	1.429	0.058	4.207	0.218	34.87	0.203
6	0.002	5.097	0.407	0.001	1.502	3.096	0.657	45.54	0.269
7	2.863	21.401	0.001	8.928	0.496	0.000	4.122	21.89	0.414
8	0.009	0.174	1.030	6.523	0.244	3.645	0.564	36.53	0.189
9	0.114	13.977	0.001	0.902	0.386	0.017	1.393	42.32	0.337
avg	**1.018**	**7.706**	**0.300**	**4.069**	**0.357**	**1.510**	**1.185**	**33.03**	**0.245**
std	1.500	6.588	0.305	2.990	0.432	1.607	1.101	7.70	0.083
								α from NLOM	
6a	0.174	3.407	0.628	3.439	0.001	3.498	0.522	51.10	0.300

CHAPTER VI

SUMMARY AND RECOMMENDATIONS

The consequence of pulsatility on arterial growth and remodeling progression may be more important than previously thought. Pulsatile pressure and flow are coupled to cardiac performance and vascular mechanics through a variety of factors, including but not limited to, cardiac contractility, heart rate, arterial compliance, and distal resistances. This coupling is a complex, dynamic, interplay of stimulus and response with adaptations to both acute (cardiac cycle, exercise) and chronic alterations (essential hypertension, atherosclerosis). Endothelial cells, smooth muscle cells, and fibroblasts are responsible for sensing altered pressure and flow and modifying the synthesis, distribution, and organization of structurally significant extracellular matrix proteins in an attempt to restore the intramural and wall shear stresses toward normal. This reorganization of cells and matrix proteins may be distributed within the wall in a manner that efficiently controls stress, but to achieve true optimization, the resulting wall configuration would need to optimize stress at diastole, systole, and mean arterial pressure (MAP) in a time dependant manner.

In this dissertation, we examined the effects of pulsatility on carotid artery remodeling in the mouse using vessels tested biaxially. Chapters II-IV using a surgical procedure known as transverse aortic banding, which allowed us to study the effects of changes in the magnitude of pulsatile pressure and flow in pairs of mouse carotids. Chapter V uses a genetic model of Marfan Syndrome to study how reductions in the effectiveness of the key protein in pulsatile remodeling (elastin) would modify arterial wall structure.

In Chapter II, we found that wall thickness and blood flow correlated best with pulsatile measures of pressure and flow, and the remodeling was located primarily in the outer

(adventitial) layer. In Chapter III, we found that both hemodynamic and wall morphological response experienced overshoot beyond desired values. The time period of 7-10 days post-surgery indicated a transition period with excessive increases in wall thickness and diameter. In Chapter IV, we modeled the findings of Chapter III using a 4-fiber family constitutive relation that allowed us to infer fiber angles and strain energy for any stretch (greater in the higher pulsatile vessels) and around physiologic operating points (lower in the higher pulsatile vessel). Finally, Chapter V showed that carotid artery circumferential adaptations to elastin with decreased effectiveness (Marfan Syndrome) are made throughout development, perhaps at the expense of the axial direction.

By examining biaxial properties of mouse common carotid arteries resulting from changes in pulsatility this research showed that pulsatility is a key component to arterial remodeling and biaxial wall morphology. We took a unique perspective by measuring both arterial blood flow and pressure to compare various metrics to remodeling throughout recovery. Furthermore, we used a model of hypertension (aortic banding) that changed the mean values of pressure and flow little while augmenting the peak values and thus the pulsatility. Based on existing literature, we chose to explore linear relationships between pulsatile hemodynamic stimulation and wall morphology. For certain relationships, however, nonlinear models may be more appropriate. While we dealt primarily with macroscopic, structural, adaptations to alterations in magnitude, future work could be performed to elucidate the pulsatile relationship further by studying arterial remodeling with altered frequency. Additionally, we did not address or quantify those biomolecules known to be mechano-sensitive and contribute to cellular vasomotor, proliferative, focal adhesion, hyperplasia/hypertrophy or differentiative responses (PGI_2, ET-1, NO, NOS, ANG-II, ACE, paxillin, vinculin). We did not quantify the mechano-transductive, dynamic affect over molecules involved in extra cellular matrix deposition,

removal, or maintenance (various growth factors, MMPs) that are crucial to arterial maintenance. In later work, an important area of biochemical histological analysis would be to quantify proteoglycan content after pulsatile remodeling. Ultimately, this work does demand future consideration of dynamic stimulation in growth and remodeling; a relationship that can be further clarified by time course measurements of biomolecules.

Pulsatility is a consequence of the evolution of the mammalian heart; therefore its influence over arterial mechanics cannot be ignored. Native blood vessels (specifically elastic arteries) will experience pulsatile remodeling in response to arterial disease or during recovery from clinical procedures. Further, with the increasing prevalence of left ventricular assist devices and improvements to tissue engineered constructs that require accurate hemodynamic environments, it is crucial that we develop our understanding of how arteries respond to pulsatile stimulation. Currently, the information in this dissertation is being employed in predictive models of time dependent arterial remodeling that can ultimately be used in the treatment of vascular disease and improve clinical interventions.

REFERENCES

1. Chobanian AV, Bakris GL, Black HR, Cushman WC, Green LA*, et al.* Seventh report of the Joint National Committee on Prevention, Detection, Evaluation, and Treatment of High Blood Pressure. *Hypertension.* 2003;**42**(6):1206-1252.

2. Berne RM, Levy MN. *Cardiovascular Physiology*. 8th ed. St. Louis, Missouri: Mosby, Inc.; 2001.

3. Humphrey JD. *Cardiovascular Solid Mechanics*. New York: Springer-Verlag; 2002.

4. Davis EC. Elastic lamina growth in the developing mouse aorta. *J Histochem Cytochem.* 1995;**43**(11):1115-1123.

5. Faury G. Function-structure relationship of elastic arteries in evolution: from microfibrils to elastin and elastic fibres. *Pathol Biol (Paris).* 2001;**49**(4):310-325.

6. Leung DY, Glagov S, Mathews MB. Elastin and collagen accumulation in rabbit ascending aorta and pulmonary trunk during postnatal growth. Correlation of cellular synthetic response with medial tension. *Circ Res.* 1977;**41**(3):316-323.

7. Bendeck MP, Keeley FW, Langille BL. Perinatal accumulation of arterial wall constituents: relation to hemodynamic changes at birth. *Am J Physiol.* 1994;**267**(6 Pt 2):H2268-2279.

8. Wells SM, Langille BL, Adamson SL. In vivo and in vitro mechanical properties of the sheep thoracic aorta in the perinatal period and adulthood. *Am J Physiol.* 1998;**274**(5 Pt 2):H1749-1760.

9. Langille BL. Remodeling of developing and mature arteries: endothelium, smooth muscle, and matrix. *J Cardiovasc Pharmacol.* 1993;**21**:S11-17.

10. Zeller PJ, Skalak TC. Contribution of individual structural components in determining the zero-stress state in small arteries. *J Vasc Res.* 1998;**35**(1):8-17.

11. Gleason RL, Jr., Humphrey JD. A 2D constrained mixture model for arterial adaptations to large changes in flow, pressure and axial stretch. *Math Med Biol.* 2005;**22**(4):347-369.

12. Gaballa MA, Jacob CT, Raya TE, Liu J, Simon B, Goldman S. Large artery remodeling during aging: biaxial passive and active stiffness. *Hypertension.* 1998;**32**(3):437-443.

13. Humphrey JD, Na S. Elastodynamics and arterial wall stress. *Ann Biomed Eng.* 2002;**30**(4):509-523.

14. Gleason RL, Humphrey JD. A mixture model of arterial growth and remodeling in hypertension: altered muscle tone and tissue turnover. *J Vasc Res.* 2004;**41**(4):352-363.

15. Wei JY. Age and the cardiovascular system. *N Engl J Med.* 1992;**327**(24):1735-1739.

16. Baumbach GL. Effects of increased pulse pressure on cerebral arterioles. *Hypertension.* 1996;**27**(2):159-167.

17. Baumbach GL, Siems JE, Heistad DD. Effects of local reduction in pressure on distensibility and composition of cerebral arterioles. *Circ Res.* 1991;**68**(2):338-351.

18. Christensen KL. Reducing pulse pressure in hypertension may normalize small artery structure. *Hypertension.* 1991;**18**(6):722-727.

19. Bakker EN, Sorop O, Spaan JA, VanBavel E. Remodeling of resistance arteries in organoid culture is modulated by pressure and pressure pulsation and depends on vasomotion. *Am J Physiol Heart Circ Physiol.* 2004;**286**(6):H2052-2056.

20. Fischer GM, Swain ML, Cherian K. Pulsatile distention and vascular collagen synthesis in the rabbit. *Blood Vessels.* 1980;**17**(4):216-220.

21. London GM, Guerin AP. Influence of arterial pulse and reflected waves on blood pressure and cardiac function. *Am Heart J.* 1999;**138**(3 Pt 2):220-224.

22. Koffi I, Safar ME, Labat C, Lacolley P, Benetos A, Mourad JJ. Arterial structural changes with verapamil in spontaneously hypertensive rats. *Am J Hypertens.* 1999;**12**(7):732-738.

23. Boutouyrie P, Bussy C, Lacolley P, Girerd X, Laloux B, Laurent S. Association between local pulse pressure, mean blood pressure, and large-artery remodeling. *Circulation.* 1999;**100**(13):1387-1393.

24. Guyton JR, Hartley CJ. Flow restriction of one carotid artery in juvenile rats inhibits growth of arterial diameter. *Am J Physiol.* 1985;**248**(4 Pt 2):H540-546.

25. Gleason RL, Gray SP, Wilson E, Humphrey JD. A multiaxial computer-controlled organ culture and biomechanical device for mouse carotid arteries. *J Biomech Eng.* 2004;**126**(6):787-795.

26. Eberth JF, Gresham VC, Reddy AK, Wilson E, Humphrey JD. Importance of pulsatility in hypertensive carotid artery growth and remodeling. *J Hypertension.* 2008 in review.

27. Eberth JF, Gresham VC, Wilson E, Humphrey JD. Time course of carotid artery growth and remodeling in response to altered pulsatility *AMJ Physiology: Heart and Circulatory Research.* 2008 in prep.

28. Eberth JF, Humphrey JD. Altered biaxial mechanical properties of carotid arteries in an aortic arch banding mouse model of hypertension. *Journal of Biomechanics.* 2008 in review.

29. Baek S, Gleason R, Rajagopal K, Humphrey J. Theory of small on large in computations of fluid-solid interactions in arteries. *Comput Methods Applied Mech Eng.* 2007;**196**:3070-3078.

30. Eberth JF, Taucer AI, Wilson E, Humphrey JD. Mechanics of carotid arteries in a mouse model of Marfan syndrome. *Annals of Biomedical Engineering.* 2008 in review.

31. Marque V, Kieffer P, Gayraud B, Lartaud-Idjouadiene I, Ramirez F, Atkinson J. Aortic wall mechanics and composition in a transgenic mouse model of Marfan syndrome. *Arterioscler Thromb Vasc Biol.* 2001;**21**(7):1184-1189.

32. Jeremy RW, Huang H, Hwa J, McCarron H, Hughes CF, Richards JG. Relation between age, arterial distensibility, and aortic dilatation in the Marfan syndrome. *Am. J. Cardiol.* 1994;**74**(4):369-373.

33. Jondeau G, Boutouyrie P, Lacolley P, Laloux B, Dubourg O*, et al.* Central pulse pressure is a major determinant of ascending aorta dilation in Marfan syndrome. *Circulation.* 1999;**99**(20):2677-2681.

34. Dajnowiec D, Langille BL. Arterial adaptations to chronic changes in haemodynamic function: coupling vasomotor tone to structural remodelling. *Clin Sci (Lond).* 2007;**113**(1):15-23.

35. Wagenseil JE, Nerurkar NL, Knutsen RH, Okamoto RJ, Li DY, Mecham RP. Effects of elastin haploinsufficiency on the mechanical behavior of mouse arteries. *Am J Physiol Heart Circ Physiol.* 2005;**289**(3):H1209-1217.

36. Jeremy RW, Huang H, Hwa J, McCarron H, Hughes CF, Richards JG. Relation between age, arterial distensibility, and aortic dilatation in the Marfan syndrome. *Am J Cardiol.* 1994;**74**(4):369-373.

37. Avolio A, Jones D, Tafazzoli-Shadpour M. Quantification of alterations in structure and function of elastin in the arterial media. *Hypertension.* 1998;**32**(1):170-175.

38. Safar ME. Pulse pressure, arterial stiffness, and cardiovascular risk. *Curr Opin Cardiol.* 2000;**15**(4):258-263.

39. Sottiurai VS, Kollros P, Glagov S, Zarins CK, Mathews MB. Morphologic alteration of cultured arterial smooth muscle cells by cyclic stretching. *J Surg Res.* 1983;**35**(6):490-497.

40. Hayakawa K, Sato N, Obinata T. Dynamic reorientation of cultured cells and stress fibers under mechanical stress from periodic stretching. *Exp Cell Res.* 2001;**268**(1):104-114.

41. Kim BS, Nikolovski J, Bonadio J, Mooney DJ. Cyclic mechanical strain regulates the development of engineered smooth muscle tissue. *Nat Biotechnol.* 1999;**17**(10):979-983.

42. Cha JM, Park SN, Noh SH, Suh H. Time-dependent modulation of alignment and differentiation of smooth muscle cells seeded on a porous substrate undergoing cyclic mechanical strain. *Artif Organs.* 2006;**30**(4):250-258.

43. Ziegler T, Nerem RM. Tissue engineering a blood vessel: regulation of vascular biology by mechanical stresses. *J Cell Biochem.* 1994;**56**(2):204-209.

44. Peng X, Recchia FA, Byrne BJ, Wittstein IS, Ziegelstein RC, Kass DA. In vitro system to study realistic pulsatile flow and stretch signaling in cultured vascular cells. *Am J Physiol Cell Physiol.* 2000;**279**(3):C797-805.

45. Sipkema P, van der Linden PJ, Westerhof N, Yin FC. Effect of cyclic axial stretch of rat arteries on endothelial cytoskeletal morphology and vascular reactivity. *J Biomech.* 2003;**36**(5):653-659.

46. Himburg HA, Dowd SE, Friedman MH. Frequency-dependent response of the vascular endothelium to pulsatile shear stress. *Am J Physiol Heart Circ Physiol.* 2007;**293**(1):H645-653.

47. Helmlinger G, Berk BC, Nerem RM. Calcium responses of endothelial cell monolayers subjected to pulsatile and steady laminar flow differ. *Am J Physiol.* 1995;**269**(2 Pt 1):C367-375.

48. Frangos JA, Eskin SG, McIntire LV, Ives CL. Flow effects on prostacyclin production by cultured human endothelial cells. *Science.* 1985;**227**(4693):1477-1479.

49. Ziegler T, Bouzourene K, Harrison VJ, Brunner HR, Hayoz D. Influence of oscillatory and unidirectional flow environments on the expression of endothelin and nitric oxide synthase in cultured endothelial cells. *Arterioscler Thromb Vasc Biol.* 1998;**18**(5):686-692.

50. Li YH, Hsieh CY, Wang DL, Chung HC, Liu SL, *et al.* Remodeling of carotid arteries is associated with increased expression of thrombomodulin in a mouse transverse aortic constriction model. *Thromb Haemost.* 2007;**97**(4):658-664.

51. Liao Y, Ishikura F, Beppu S, Asakura M, Takashima S, *et al.* Echocardiographic assessment of LV hypertrophy and function in aortic-banded mice: necropsy validation. *Am J Physiol Heart Circ Physiol.* 2002;**282**(5):H1703-1708.

52. Rockman HA, Knowlton KK, Ross JJ, Chien KR. In vivo murine cardiac hypertrophy: a novel model to identify genetic signaling mechanisms that activate an adaptive physiological response. *Circulation.* 1993;**87**(suppl VII):VII-14-VII-21.

53. Nakamura A, Rokosh DG, Paccanaro M, Yee RR, Simpson PC, *et al.* LV systolic performance improves with development of hypertrophy after transverse aortic constriction in mice. *Am J Physiol Heart Circ Physiol.* 2001;**281**(3):H1104-1112.

54. Li YH, Reddy AK, Ochoa LN, Pham TT, Hartley CJ*, et al.* Effect of age on peripheral vascular response to transverse aortic banding in mice. *J Gerontol A Biol Sci Med Sci.* 2003;**58**(10):B895-899.

55. Li YH, Reddy AK, Taffet GE, Michael LH, Entman ML, Hartley CJ. Doppler evaluation of peripheral vascular adaptations to transverse aortic banding in mice. *Ultrasound Med Biol.* 2003;**29**(9):1281-1289.

56. Pezet M, Jacob MP, Escoubet B, Gheduzzi D, Tillet E*, et al.* Elastin haploinsufficiency induces alternative aging processes in the aorta. *Rejuvenation Res.* 2008;**11**(1):97-112.

57. Hartley CJ, Reddy AK, Madala S, Entman ML, Michael LH, Taffet GE. Noninvasive ultrasonic measurement of arterial wall motion in mice. *Conf Proc IEEE Eng Med Biol Soc.* 2004;**5**:3688-3691.

58. Janssen BJ, De Celle T, Debets JJ, Brouns AE, Callahan MF, Smith TL. Effects of anesthetics on systemic hemodynamics in mice. *Am J Physiol Heart Circ Physiol.* 2004;**287**(4):H1618-1624.

59. Stegall HF, Kardon MB, Kemmerer WT. Indirect measurement of arterial blood pressure by Doppler ultrasonic sphygmomanometry. *J Appl Physiol.* 1968;**25**(6):793-798.

60. Reddy AK, Taffet GE, Madala S, Michael LH, Entman ML, Hartley CJ. Noninvasive blood pressure measurement in mice using pulsed Doppler ultrasound. *Ultrasound Med Biol.* 2003;**29**(3):379-385.

61. Gleason RL, Gray SP, Wilson E, Humphrey JD. A multiaxial computer-controlled organ culture and biomechanical device for mouse carotid arteries. *J. Biomech. Eng.* 2004;**126**(6):787-795.

62. Gleason RL, Wilson E, Humphrey JD. Biaxial biomechanical adaptations of mouse carotid arteries cultured at altered axial extension. *J. Biomech.* 2007;**40**(4):766-776.

63. Gleason RL, Humphrey JD. A 2D constrained mixture model for arterial adaptations to large changes in flow, pressure and axial stretch. *Math. Med. Biol.* 2005;**22**(4):347-369.

64. Hu JJ, Ambrus A, Fossum TW, Miller MW, Humphrey JD, Wilson E. Time courses of growth and remodeling of porcine aortic media during hypertension: a quantitative immunohistochemical examination. *J Histochem Cytochem.* 2008;**56**(4):359-370.

65. Rich L, Whittaker P. Collagen and picrosirius red staining: a polarized light assessment of fibrillar hue and spatial distribution. *Braz. J. Morphol. Sci.* 2005;**22**(2):97-104.

66. Safar ME, Boudier HS. Vascular development, pulse pressure, and the mechanisms of hypertension. *Hypertension.* 2005;**46**(1):205-209.

67. Recchia FA, Byrne BJ, Kass DA. Sustained vessel dilation induced by increased pulsatile perfusion of porcine carotid arteries in vitro. *Acta Physiol Scand.* 1999;**166**(1):15-21.

68. Fung YC, Liu SQ. Change of residual strains in arteries due to hypertrophy caused by aortic constriction. *Circ Res.* 1989;**65**(5):1340-1349.

69. Davies PF. Flow-mediated endothelial mechanotransduction. *Physiol Rev.* 1995;**75**(3):519-560.

70. Alberding JP, Baldwin AL, Barton JK, Wiley E. Onset of pulsatile pressure causes transiently increased filtration through artery wall. *Am J Physiol Heart Circ Physiol.* 2004;**286**(5):H1827-1835.

71. Walker-Caprioglio HM, Koob TJ, McGuffee LJ. Proteoglycan synthesis in normotensive and spontaneously hypertensive rat arteries in vitro. *Matrix.* 1992;**12**(4):308-320.

72. Reynertson RH, Parmley RT, Roden L, Oparil S. Proteoglycans and hypertension. I. A biochemical and ultrastructural study of aorta glycosaminoglycans in spontaneously hypertensive rats. *Coll Relat Res.* 1986;**6**(1):77-101.

73. Matsumoto T, Hayashi K. Mechanical and dimensional adaptation of rat aorta to hypertension. *J Biomech Eng.* 1994;**116**(3):278-283.

74. Strauss BH, Rabinovitch M. Adventitial fibroblasts: defining a role in vessel wall remodeling. *Am J Respir Cell Mol Biol.* 2000;**22**(1):1-3.

75. Sartore S, Chiavegato A, Faggin E, Franch R, Puato M*, et al.* Contribution of adventitial fibroblasts to neointima formation and vascular remodeling: from innocent bystander to active participant. *Circ Res.* 2001;**89**(12):1111-1121.

76. Maiellaro K, Taylor WR. The role of the adventitia in vascular inflammation. *Cardiovasc Res.* 2007;**75**(4):640-648.

77. Pagano PJ, Gutterman DD. The adventitia: the outs and ins of vascular disease. *Cardiovasc Res.* 2007;**75**(4):636-639.

78. Humphrey J, Eberth J, Dye W, Gleason R. Fundamental role of axial stress in compensatory adaptations by arteries. *Journal of Biomechanics.* 2008 in review.

79. Arribas SM, Hinek A, Gonzalez MC. Elastic fibres and vascular structure in hypertension. *Pharmacol Ther.* 2006;**111**(3):771-791.

80. Greenwald SE. Ageing of the conduit arteries. *J Pathol.* 2007;**211**(2):157-172.

81. Li Q, Muragaki Y, Hatamura I, Ueno H, Ooshima A. Stretch-induced collagen synthesis in cultured smooth muscle cells from rabbit aortic media and a possible involvement of angiotensin II and transforming growth factor-beta. *J Vasc Res.* 1998;**35**(2):93-103.

82. Sasamura H, Shimizu-Hirota R, Saruta T. Extracellular matrix remodeling in hypertension. *Curr Hyperten Rev* 2005;**1**:51-60.

83. Humphrey JD. Vascular adaptation and mechanical homeostasis at tissue, cellular, and sub-cellular levels. *Cell Biochem Biophys.* 2008;**50**(2):53-78.

84. Wicker BK, Hutchens HP, Wu Q, Yeh AT, Humphrey JD. Normal basilar artery structure and biaxial mechanical behaviour. *Comput Methods Biomech Biomed Engin.* 2008:1-13.

85. Gleason RL, Dye WW, Wilson E, Humphrey JD. Quantification of the mechanical behavior of carotid arteries from wild-type, dystrophin-deficient, and sarcoglycan-delta knockout mice. *J Biomech.* 2008.

86. Baek S, Gleason RL, Rajagopal KR, Humphrey JD. Theory of small on large: potential utility in computations of fluid–solid interactions in arteries *Computer Methods in Applied Mechanics and Engineering.* 2007;**196**(31-32):3070-3078

87. Tsamis A, Stergiopulos N. Arterial remodeling in response to hypertension using a constituent-based model. *Am J Physiol Heart Circ Physiol.* 2007;**293**(5):H3130-3139.

88. Milewicz DM, Dietz HC, Miller DC. Treatment of aortic disease in patients with Marfan syndrome. *Circulation.* 2005;**111**(11):e150-157.

89. Pyeritz R. The Marfan syndrome. *Annu. Rev. Med.* 2000;**51**:481-510.

90. Sherratt MJ, Baldock C, Haston JL, Holmes DF, Jones CJ*, et al.* Fibrillin microfibrils are stiff reinforcing fibres in compliant tissues. *J. Mol. Biol.* 2003;**332**(1):183-193.

91. Carton RW, Dainauskas J, Clark JW. Elastic properties of single elastic fibers. *J. Appl. Physiol.* 1962;**17**(3):547-551.

92. Neptune ER, Frischmeyer PA, Arking DE, Myers L, Bunton TE*, et al.* Dysregulation of TGF-β activation contributes to pathogenesis in Marfan syndrome. *Nat. Genet.* 2003;**33**(3):407-411.

93. Habashi JP, Judge DP, Holm TM, Cohn RD, Loeys BL*, et al.* Losartan, an AT1 antagonist, prevents aortic aneurysm in a mouse model of Marfan syndrome. *Science.* 2006;**312**(5770):117-121.

94. Pereira L, Lee SY, Gayraud B, Andrikopoulos K, Shapiro SD*, et al.* Pathogenetic sequence for aneurysm revealed in mice underexpressing fibrillin-1. *Proc. Natl. Acad. Sci. U. S. A.* 1999;**96**(7):3819-3823.

95. Bunton TE, Biery NJ, Myers L, Gayraud B, Ramirez F, Dietz HC. Phenotypic alteration of vascular smooth muscle cells precedes elastolysis in a mouse model of Marfan syndrome. *Circ. Res.* 2001;**88**(1):37-43.

96. Chung AW, Au Yeung K, Sandor GG, Judge DP, Dietz HC, van Breemen C. Loss of elastic fiber integrity and reduction of vascular smooth muscle contraction resulting from the upregulated activities of matrix metalloproteinase-2 and -9 in the thoracic aortic aneurysm in Marfan syndrome. *Circ Res.* 2007;**101**:512-522.

97. Marque V, Kieffer P, Gayraud B, Lartaud-Idjouadiene I, Ramirez F, Atkinson J. Aortic wall mechanics and composition in a transgenic mouse model of Marfan syndrome. *Arterioscler. Thromb. Vasc. Biol.* 2001;**21**(7):1184-1189.

98. Groenink M, de Roos A, Mulder BJ, Verbeeten BJ, Timmermans J, *et al.* Biophysical properties of the normal-sized aorta in patients with Marfan syndrome: evaluation with MR flow mapping. *Radiology.* 2001;**219**(2):535-540.

99. Groenink M, de Roos A, Mulder BJ, Spaan JA, van der Wall EE. Changes in aortic distensibility and pulse wave velocity assessed with magnetic resonance imaging following beta-blocker therapy in the Marfan syndrome. *Am. J. Cardiol.* 1998;**82**(2):203-208.

100. Gleason RL, Humphrey JD. Effects of a sustained extension on arterial growth and remodeling: a theoretical study. *J. Biomech.* 2005;**38**(6):1255-1261.

101. Chuong CJ, Fung YC. On residual stresses in arteries. *J Biomech Eng.* 1986;**108**(2):189-192.

102. Han HC, Fung YC. Longitudinal strain of canine and porcine aortas. *J. Biomech.* 1995;**28**(5):637-641.

103. Weizsacker H, Lambert H, Pascale K. Analysis of the passive mechanical properties of rat carotid arteries. *J. Biomech.* 1983;**16**(9):703-715.

104. Van Loon P, Klip W, Bradley EL. Length-force and volume-pressure relationships of arteries. *Biorheology.* 1977;**14**(4):181-201.

105. Brossollet LJ, Vito RP. An alternate formulation of blood vessel mechanics and the meaning of the in vivo property. *J. Biomech.* 1995;**28**(6):679-687.

106. Dye WW, Gleason RL, Wilson E, Humphrey JD. Altered biomechanical properties of carotid arteries in two mouse models of muscular dystrophy. *J. Appl. Physiol.* 2007;**103**(2):664-672.

107. Charbonneau NL, Ono RN, Corson GM, Keene DR, Sakai LY. Fine tuning of growth factor signals depends on fibrillin microfibril networks. *Birth Defects Res.* 2004;**72**(1):37-50.

108. Arteaga-Solis E, Gayraud B, Ramirez F. Elastic and collagenous networks in vascular diseases. *Cell Struct. Funct.* 2000;**25**(2):69-72.

109. Ramirez F, Pereira L. The fibrillins. *Int. J. Biochem. Cell Biol.* 1999;**31**(2):255-259.

110. Lillie MA, David GJ, Gosline JM. Mechanical role of elastin-associated microfibrils in pig aortic elastic tissue. *Connect Tissue Res.* 1998;**37**(1-2):121-141.

111. Chung AW, Au Yeung K, Sandor GG, Judge DP, Dietz HC, van Breemen C. Loss of Elastic Fiber Integrity and Reduction of Vascular Smooth Muscle Contraction Resulting From the Upregulated Activities of Matrix Metalloproteinase-2 and -9 in the Thoracic Aortic Aneurysm in Marfan Syndrome. *Circ. Res.* 2007.

112. Jackson ZS, Gotlieb AI, Langille BL. Wall tissue remodeling regulates longitudinal tension in arteries. *Circ. Res.* 2002;**90**(8):918-925.

113. Langille BL. Remodeling of developing and mature arteries: endothelium, smooth muscle, and matrix. *J. Cardiovasc. Pharmacol.* 1993;**21 Suppl 1**:S11-17.

114. Kouchoukos NT, Dougenis D. Surgery of the thoracic aorta. *N. Engl. J. Med.* 1997;**336**(26):1876-1888.

115. Pezet M, Jacob MP, Escoubet B, Gheduzzi D, Tillet E, *et al.* Elastin Haploinsufficiency Induces Alternative Aging Processes in the Aorta. *Rejuvenation Res.* 2008.

116. Dobrin PB. Mechanical properties of arterises. *Physiol. Rev.* 1978;**58**(2):397-460.

VITA

Name:	John Francis Eberth
Address:	c/o Biomedical Engineering Department, Texas A&M University, College Station, TX, 77843-3120
Email Address:	jeberth@tamu.edu
Education:	B.S., Mechanical Engineering, Clarkson University, May 2001 M.S., Mechanical Engineering, Clemson University, August 2004 Ph.D., Biomedical Engineering, Texas A&M University, December 2008
Post Doctorate:	Rice University, 2008